Search for Θ^+ via $\pi^- p \rightarrow K^- X$ Reaction near Production Threshold

Koji Miwa

A dissertation submitted in partial fulfillment of
the requirements for the degree of

Doctor of Science

Department of Physics
Faculty of Science
Kyoto University

May, 2006

Abstract

We have searched for Θ^+ via $\pi^- p \rightarrow K^- X$ reaction using 1.87 and 1.92 GeV/c π^- beam at the K2 beam line of the KEK 12 GeV Proton Synchrotron. A SCIFI target ($(\mathrm{CH})_n$) was exposed to 2.9×10^9 π^-'s with momentum of 1.87 GeV/c. For the search for the Θ^+, a polyethylene target ($(\mathrm{CH}_2)_n$)was mainly used to enhance the contribution from free protons and was exposed to 3.0×10^9 π^-'s of 1.87 GeV/c and 7.4×10^9 π^-'s of 1.92 GeV/c.

In the missing mass of the $\pi^- p \rightarrow K^- X$ reaction at 1.87 GeV/c, any structure corresponding to the Θ^+ have not been observed. In the missing mass at 1.92 GeV/c, a bump of which width was consistent with the experimental resolution has been found at the mass of $M = 1530.6^{+2.2}_{-1.9}(\mathrm{stat.})^{+1.9}_{-1.3}(\mathrm{syst.})$ MeV/c^2. However the statistical significance of the bump is only 2.5∼2.7σ which is not sufficient to claim the evidence of the Θ^+. Therefore we have derived the upper limit of the production cross section via the $\pi^- p \rightarrow K^- \Theta^+$ reaction. The upper limits of the differential cross sections averaged over 0 deg to 20 deg in the laboratory frame have been obtained to be 1.6 μb/sr and 2.9 μb/sr at the 90 % confidence level at the beam momenta of 1.87 and 1.92 GeV/c, respectively. The upper limits of the total cross sections have been obtained to be 1.8 μb and 3.9 μb at 1.87 and 1.92 GeV/c, respectively, assuming that the Θ^+ is produced isotropically in the center of mass system. The obtained upper limits are quite smaller than the theoretical calculations and give a strong constraint to the unknown parameters such as the coupling constant $g_{K^* N \Theta}$ used in the calculations.

Contents

Chapter 1

Introduction

1.1 The Θ^+ baryon

The color interaction between quarks and gluons is described by Quantum Chromodynamics (QCD), a theory of strong interaction. One of the most remarkable successes can be seen in the good agreement between the experimental results and the calculations by QCD in the high energy region, where QCD can be treated perturbatively. When we take a look at the low energy region, the properties of hadrons such as spin, parity, magnetic moment and mass should be explained by QCD. However the framework of QCD in the low energy region is still in progress due to its non-perturbative nature. Currently most of the hadron properties have been understood by using the effective models based on the principle of QCD; quarks and gluons have quantum number of "color" with the $\mathrm{SU}(3)_{color}$ symmetry and hadrons, compound of the quarks and the gluons, must be the singlet state of the $\mathrm{SU}(3)_{color}$ symmetry. In the constituent quark model, which is one of the most familiar models based on QCD, mesons and baryons are described by quark and anti-quark pair and three quarks respectively. The hadrons known so far are well classified by the quark model taking into account the assignment of flavors and spins of the constituent quarks. The masses of hadrons are also well reproduced by considering the effective color magnetic interaction between quarks. In these frameworks, the existence of exotic hadrons such as "hybrid meson ($q\bar{q}g$)", "baryonium ($qq\bar{q}\bar{q}$)", "pentaquark ($qqqq\bar{q}$)" and "dibaryon ($qqqqqq$)" has also been predicted theoretically, because QCD requires only that hadrons should be color singlet, but does not restrict the number of quarks [1]. Although many experimental efforts to search for these exotics were made, there was no clear evidence of such states.

The pentaquark is the exotic particle which consists of four quarks and one anti-quark. In particular, the pentaquark with a positive strangeness $S = +1$ has been attracting attentions of physicists, because it has a "$\bar{s}$" quark as a constituent quark and cannot be a simple three-quark state. Therefore resonance states of K^+ and nucleon were vigorously searched for using the partial wave analysis of K^+-nucleon scattering from the 1970's. These searches resulted in two possibilities, the isoscalar $Z_0(1780)$ and $Z_0(1865)$ [2, 3]. However the evidence of the existence was denied by PDG group because there was no conclusive confirmation for a long time [4]. The comment of PDG group is following, *"The evidence for strangeness +1 baryon resonances was reviewed in our 1976 edition [5], and more recently by Kelly [6] and by Oades [7]. Two new partial-wave analyses have appeared since our 1984 edition [2, 3]. Both claim that the* P_{13} *and perhaps other waves resonate. However, the results permit no definite conclusion- the same story heard for 15 years. The standards of proof must simply be much more severe here than in a channel in which many resonances are already known to exist. The general prejudice against baryons not made*

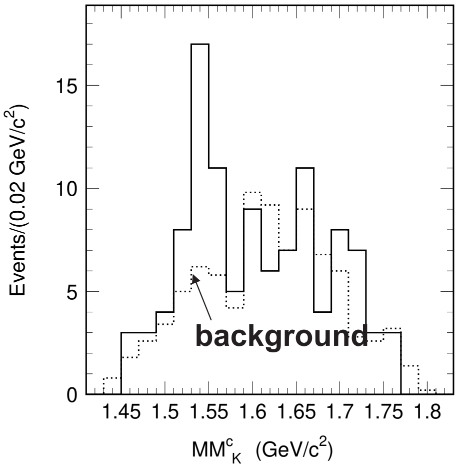

Figure 1.1: The first evidence on the existence of the Θ^+ reported by SPring-8/LEPS collaboration. The solid histogram is a missing mass spectrum of $\gamma n \rightarrow K^-$X reaction where K^+ is also detected. The hatched histogram is the estimated background from $\gamma p \rightarrow K^- K^+$X reaction. The peak with a Gaussian significance of 4.6σ was observed at 1540 ± 10 MeV/c^2. The only upper limit of the width was reported to be less than 25 MeV/c^2 because the observed width was consistent with the experimental resolution.

of three quarks and the lack of any experimental activity in this area make it likely that it will be another 15 years before the issue is decided.”.

It was almost just 15 years after the comment of PDG group that the report on the evidence of the baryon resonance with $S = +1$, which is now called Θ^+, was made by SPring-8/LEPS collaboration [8]. They measured the $\gamma n \rightarrow K^- K^+ n$ exclusive reaction where neutrons in ^{12}C nuclei were used as a target and showed a peak in mass distribution of the missing mass of the $\gamma n \rightarrow K^- X$ reaction as shown in Figure 1.1. They have claimed that the mass of the Θ^+ is 1.54 ± 0.01 GeV/c^2. The observed width is consistent with its experimental resolution and the only upper limit of 25 MeV/c^2 has been reported.

The analysis at SPring-8 was motivated by the theoretical prediction based on the chiral soliton model by Diakonov, Petrov and Polyakov [9]. They predicted the narrow resonance state of width less than 15 MeV/c^2 at 1530 MeV/c^2. The nice agreement between the theoretical prediction and the experimental result at SPring-8 stimulated many physicists. Possible evidences of the narrow baryonic resonance Θ^+ with mass around 1530 MeV/c^2 and strangeness of +1 and width of about $\Gamma < 15$ MeV/c^2 were reported one after another by several collaborations [10] using various reactions such as photo-induced reaction, kaon-nucleon scattering, proton-proton reaction, ν A reaction and deep inelastic electron scattering.

Such a state is extremely exciting because it is unambiguously exotic in the sense that it cannot be a simple three-quark state as mentioned above. Therefore much of the theoretical activity has been aimed at understanding the structure of the exotic state, Θ^+ [11]. Besides using the chiral soliton model, the most common treatment of this problem has been based on variants of the quark model where the new baryon is identified as a pentaquark [12, 13]. Other approaches treat the Θ^+ in terms of meson-baryon binding or as a kaon-pion-nucleon state [14]. Attempts to identify quantum numbers of the Θ^+ and to confirm or deny its existence directly from QCD have been performed within the lattice Monte Carlo simulations [15, 16, 17, 18, 19] and within the QCD sum-rules [20].

One of the most remarkable feature of the Θ^+ is its narrow width. In general, the

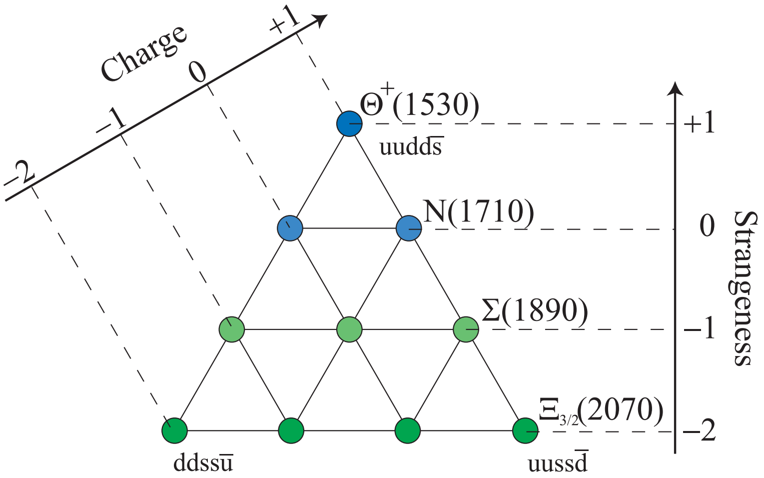

Figure 1.2: The proposed anti-decuplet of baryons with $J^P = 1/2^+$ by chiral soliton model [9]. The anti-decuplet includes the exotic particles, Θ^+, Ξ^+ and Ξ^{--} at the corners of this diagram. The quark content and the predicted masses are shown.

mass and width of a resonance of two particles is related through the depth and range of the potential. For a simple attractive potential of range ∼1 fm, the width of a P-wave resonance 100 MeV/c^2 above threshold is above 175 MeV/c^2. To produce a width of order of 10 MeV/c^2 requires a range of about 0.05 fm [12]. Thus the observed width of the Θ^+ is one of the reasons to consider the Θ^+ as not a loosely bound state of K^+n like a molecule but a pentaquark state. In order to understand the narrow width, many theoretical models are proposed considering the additional correlation between quarks. The difference of the dynamics proposed in several models appears as the difference of the spin and parity of the Θ^+. Therefore experimentally, in addition to confirm the existence, it is quite important to determine the spin and parity to select theoretical models and to understand the quark dynamics in the low energy region.

Recently, however, negative results were reported from high energy experiments where they searched for the Θ^+ with much higher statistics [10]. Consequently the status of the Θ^+ is currently becoming controversial. Therefore the confirmation of the Θ^+ is urgent and crucial.

In this thesis, we present the results of the experimental search for the Θ^+ via $\pi^- p \to K^- X$ reaction. In this introduction chapter, theoretical works are reviewed first. Then we mention about the experimental status with both positive and negative results. Finally, we describe the importance of the search via hadronic reactions we have executed.

1.2 Theoretical works

1.2.1 Structure of Θ^+

The narrow resonance state of width less than 15 MeV/c^2 at 1530 MeV/c^2 was first predicted by D. Diakonov, Petrov and Polyakov using chiral soliton model [9]. The chiral soliton model is a model of baryons based on the large-N_c (number of color) limit. The "soliton" is another word for the self-consistent pion mean-field in the nucleon in which the quarks move. The light baryons are regarded as the rotational state in space and flavor SU(3) space. The ordinary baryon octet and decuplet are assigned to the lowest and first excited states of the rotational states of the soliton and the masses of these states are reproduced within accuracy of 1%. The exotic anti-decuplet state including the Θ^+ is the next excited state and the members are shown in Figure 1.2. The spin of the anti-decuplet is 1/2 and the parity is positive same as the octet and decuplet baryons in the chiral soliton model. Diakonov *et al.* assumed the state $N^*(1710)$ to be a member of the proposed anti-decuplet in order to have a prediction for the absolute mass of the Θ^+. They also calculated the decay width $\Gamma < 15$ MeV, which triggered the experimental searches. In their formalism the narrowness of the Θ^+ occurs due to a cancellation of different contributions in the decay operator.

Jaffe and Wilczek describe the exotic states as pentaquarks composed of two strongly bound scalar diquarks (ud) interacting with a strange anti-quark [12]. They took particular note of the strong attractive force interacting between diquarks in spin-zero, color and flavor $\bar{\mathbf{3}}$ configuration. In order to combine with the anti-quark, the two diquarks must combine into a color $\mathbf{3}$, the antisymmetric part of $\bar{\mathbf{3}} \times \bar{\mathbf{3}}$. Therefore the wave function must be antisymmetric under space exchange, i.e. P-wave, in order to symmetrize all system other than color. Their prediction of the Θ^+ with $J^P = 1/2^+$ is significantly different from the assignment of $1/2^-$ by the naive quark model where all quarks stay in S-state. The model predicts that lowest-lying pentaquark states are a nearly ideally mixed combination of an $\mathrm{SU}(3)_{\mathrm{flavor}}$ octet and an $\mathrm{SU}(3)_{\mathrm{flavor}}$ anti-decuplet. One basic feature of the model is the prediction of two pentaquark states with nucleon quantum numbers: one with a mass of ~1450 MeV/c^2 and the other with a mass of ~ 1700 MeV/c^2. These states have been tentatively identified with the Roper resonance $N^*(1440)$ and the $N^*(1710)$. In this framework, it is needed for the decay to re-assign quarks from the diquark-diquark-antiquark configuration to the KN, quark-antiquark and three quarks, configuration. Due to the re-assignment, the decay of the Θ^+ is considered to be suppressed. They also mention the possibility of charm and bottom analogues of the Θ^+, $\Theta_c^0(uudd\bar{c})$ and $\Theta_b^+(uudd\bar{b})$.

The study of the Θ^+ by Lattice QCD is a challenging work. One of the biggest challenge is how to choose the baryonic operator. Furthermore, since the Θ^+ can be close to the KN threshold, it is essential in any lattice spectroscopy calculation to reliably distinguish between genuine five-quark bound states and meson-baryon scattering states. In these status, here, the independent four Lattice calculations are introduced.

Sasaki using double exponential fits, found a state consistent with the Θ^+ also in the $I = 0$, $J^P = 1/2^-$ channel [15]. He also managed to identify the charmed analogue of the Θ^+ 640 MeV/c^2 above the DN threshold.

Csikor *et al.* using a different operator identified a state in the $I = 0$, $J^P = 1/2^-$ channel with a mass consistent with the observed Θ^+ and the lowest mass found in the opposite parity $I = 0$, $J^P = 1/2^+$ channel was significantly higher [16].

Liu *et al.* reported that they were not able to see any KN-state compatible with the Θ^+ in either parity isosinglet channel [17].

Chiu and Hsieh, in disagreement with the first two studies, found a positive parity isosinglet state compatible to the observed Θ^+, whereas the lowest state they found in the negative parity state had much higher mass [18].

Ishii *et al.* have studied both the positive- and negative-parity pentaquark baryons with $I = 0$ and spin $J = 1/2$ in anisotropic quenched lattice QCD [19]. The lowest negative-parity pentaquark state is found to have a mass of 1.75 GeV/c^2, while the lowest one with positive-parity appears at 2.25 GeV/c^2. They claim that the negative-parity state is not a compact pentaquark state but an S-wave NK-scattering state.

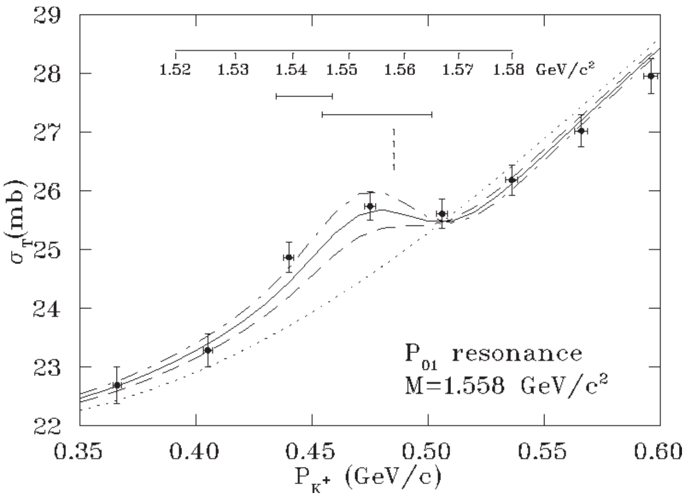

Figure 1.3: K^+d total cross section corrected for the effects of both the beam momentum spread and Fermi momentum distribution measured by T. Bowen *et al.* [21]. Calculations using a weak scattering approximation for the p-wave resonance by W.R. Gibbs are also shown by smooth curves [28]. The dash-dotted, solid, and dashed curves correspond to width of 1.2, 0.9, and 0.6 MeV/c^2, respectively.

1.2.2 K^+N scattering and width of Θ^+

Because the Θ^+ baryon is considered to be a resonance state of K^+ and neutron, a K^+d scattering is the most straightforward way to search for the resonance. However there was no clear evidence of the resonance in the region around 1530 MeV/c^2 from the past K^+d scattering data. A question why the Θ^+ was missed in the past experiments is raised. The answer to the question probably lies, at least partly, in the very small width of the Θ^+ which appears to be emerging from the step size of momentum of K^+. At the first stage from the report by LEPS, discussions whether the Θ^+ could be consistent with the past K^+d scattering data have been done vigorously in connection with the width of the Θ^+. Here, at first, the experimental data of the past K^+d scattering are reviewed. Then recent re-analyses with these scattering data are reviewed.

The K^+N scatterings such as K^+p and K^+d scattering were measured mostly with bubble chambers in the 1960's and 1970's [21, 22, 23]. The isospin $I = 0$ amplitude has to be extracted from the K^+d scattering which is the mixture of $I = 0$ and $I = 1$ states. To extract this amplitude, we have to correct the effect of beam momentum spread and Fermi momentum distribution. If the mass of the Θ^+ is assumed to be 1530 MeV/c^2, then the momentum of K^+ on resonance in K^+n scattering is 420 MeV/c. Such low momentum K^+ beams were provided by degrading initial beams of higher momenta. Therefore the resulting beams had momenta with spread of typically 6% (FWHM). Moreover the Fermi motion of a neutron in a deuteron had to be corrected. Due to the difficulty of treatment of these unfolding procedures, there was disagreement between the cross sections measured in different experiments. Figure 1.3 shows one of the results after these corrections by T. Bowen *et al.* [21].

One of the first to discuss the relation of the past scattering database and the width of the Θ^+ is Nussinov. He evaluated a peak cross section at the resonance in isospin $I = 0, J^P = 1/2^+$ P-wave channel to be $\sim$ 37 mb. In the past experiments, the intervals of measured momentum points were typically 30 MeV/c. If the Θ^+ is narrow, it could escape the detection if there is a gap in the database at the resonant energy. However the resonance structure should be spread out by the Fermi momentum of a neutron so that it should be noticeable. Considering these effects of Fermi motion, he concludes that the width of the Θ^+ must be less than 6 MeV/c^2 [24].

Arndt, who is one of the authors of the reference [25] where partial wave analysis was done for the database of K^+-nucleon scattering before the report of LEPS , reanalyzed the database focusing on the energy region around 1540 MeV/c^2. He checked the change of χ^2 in fitting the database considering that there is a resonance structure around 1540 MeV/c^2 with some width. From the change of this χ^2, he concludes that the resonance must have a width of the order of 1 MeV/c^2 or less [26].

Cahn and Tilling calculated the width from the result of DIANA experiment [29], where the Θ^+ was observed via charge exchange channel of $K^+n \to K^0p$, and obtained the width of 0.9 ± 0.3 MeV/c^2 [27]. They also estimated the upper limit of the width to be 1 MeV/c^2 $\sim$ 4 MeV/c^2 from the K^+d scattering data.

Gibbs shows the possible existence of a narrow resonance around 1550 MeV/c^2 [28] by comparing the calculation of K^+d total cross section taking into account double scattering of K^+ and Fermi motion correction of a neutron with the measured cross section by Bowen *et al.*. The calculation is shown in Figure 1.3 with the experimental result. The dash-dotted, solid and dashed curves correspond to widths of 1.2, 0.9 and 0.6 MeV/c^2 for positive parity resonance, respectively. The dotted curve is the background fit. Assuming a negative parity resonance gives lower mass.

As reviewed above, all analyses with K^+-nucleon data arrive at the conclusion that the width of the Θ^+ must be less than a few MeV/c^2. Such narrow width is unusual for hadron resonances. If the width of the Θ^+ is really narrow, by revealing the decay mechanism of this resonance we would obtain a new knowledge concerning the quark dynamics in the low energy region.

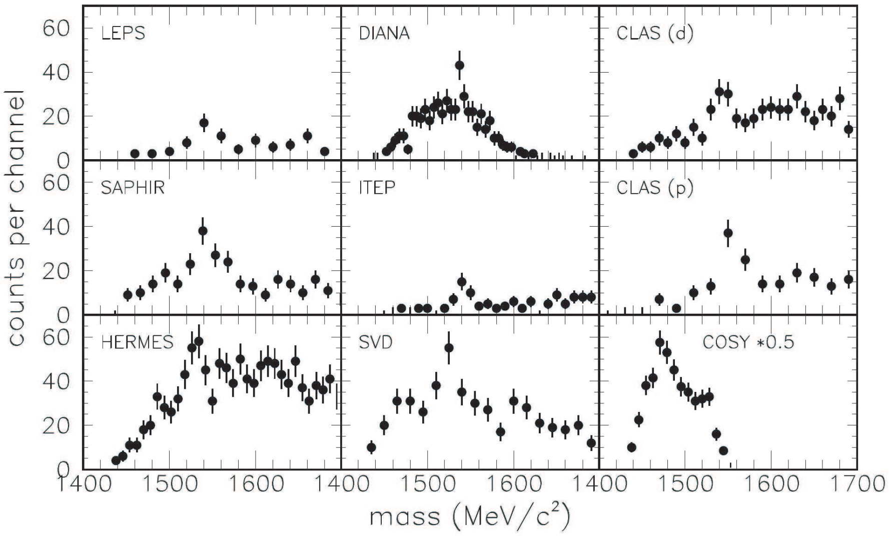

Figure 1.4: Data from experiments with positive evidence for the Θ^+. This figure is taken from Reference [10]

1.3 Experimental review

The first report on the evidence of the Θ^+ baryon with positive strangeness $S = +1$ [8] has been immediately confirmed by several collaborations with various reactions such as photon-induced reactions [30, 31, 33], K^+n charge exchange reaction [29], neutrino scattering [32], deep inelastic electron scatterings [34, 35], proton-proton reaction [36] and p-A reaction [37]. Moreover the possible existences of two more exotic particles, the Ξ^{--} and the Θ_c, have been indicated by NA49 collaboration at CERN [39] and H1 collaboration at DESY [40], respectively. The Ξ^{--} baryon with double strangeness $S = -2$ is one of the member of anti-decuplet and the minimum quark contents are $ddss\bar{u}$. The Θ_c baryon is the charmed analogue of the Θ^+ which has $\bar{c}$ quark instead of $\bar{s}$ quark. The results of published experiments with positive evidence are shown in Figure 1.4. When plotted this way, it is clear that the statistics of all experiments is not sufficient to claim a clear observation and better statistics is needed. Recently, null results have been reported from several high energy experiments where they searched for the Θ^+ with much higher statistics. However it should be pointed out that in these experiments many charged particles are produced in a interaction which make a huge combinatorial background. Moreover the Σ^{*+} resonances such as the $\Sigma(1670)$ are not seen. Most recently, CLAS collaboration has reported some results of a series of high statistical searches for the Θ^+. In some of the results, the Θ^+ has not been observed [53, 54]. Consequently, the situation of the Θ^+ is controversial. In this section these experimental results with both positive and negative results, which are summarized in Table 1.1 and 1.2 respectively, are reviewed.

Reference	Group	Reaction	Mass(MeV)	Width(MeV)	$\sigma's$
[8]	LEPS	$\gamma C \rightarrow K^+K^-X$	1540 ± 10	<25	4.6
[29]	DIANA	$K^+Xe \rightarrow K^0pX$	1539 ± 2	<9	4.4
[30]	CLAS	$\gamma d \rightarrow K^+K^-p(n)$	1542 ± 5	<21	5.2±0.6 [1]
[31]	SAPHIR	$\gamma p \rightarrow K^+K^0(n)X$	1540 ± 6	<25	4.8 [2]
[32]	ITEP	$\nu A \rightarrow K^0pX$	1533 ± 5	<20	6.7
[33]	CLAS	$\gamma p \rightarrow \pi^+K^+K^-(n)$	1555 ± 10	<26	7.8
[34]	HERMES	$e^+d \rightarrow K^0pX$	1526 ± 3	13 ± 9	∼5
[35]	ZEUS	$e^+p \rightarrow e^+K^0pX$	1522 ± 3	8 ± 4	∼5
[36]	COSY-TOF	$pp \rightarrow K^0p\Sigma^+$	1530 ± 5	<18	4-6
[37]	SVD	$pA \rightarrow K^0pX$	1526 ± 5	<24	5.6

Table 1.1: Published experiments with evidence for the Θ^+ baryon

Reference	Group	Reaction	Limit
[41]	BES	$e^+e^- \rightarrow J/\Psi \rightarrow \bar{\Theta}\Theta$	$< 1.1 \times 10^{-5}$ B.R.
[43]	BarBar	$e^+e^- \rightarrow \Upsilon(4S) \rightarrow pK^0X$	$< 1.0 \times 10^{-4}$ B.R.
[44]	Belle	$e^+e^- \rightarrow B^0\bar{B}^0 \rightarrow p\bar{p}K^0X$	$< 2.3 \times 10^{-7}$ B.R.
[45]	LEP	$e^+e^- \rightarrow z \rightarrow pK^0X$	$< 6.2 \times 10^{-4}$ B.R.
[46]	HERA-B	$pA \rightarrow K^0pX$	$< 0.02 \times \Lambda^*$
[47]	SPHINX	$pC \rightarrow K^0pX$	$< 0.1 \times \Lambda^*$
[48]	HyperCP	$pCu \rightarrow K^0pX$	$< 0.3\%$ K^0p
[49]	CDF	$p\bar{p} \rightarrow K^0pX$	$< 0.03 \times \Lambda^*$
[50]	FOCUS	$\gamma BeO \rightarrow K^0pX$	$< 0.02 \times \Sigma^*$
[51]	Belle	$K^+Si \rightarrow K^0pX$	$< 0.02 \times \Lambda^*$
[52]	PHENIX	$AuAu \rightarrow K^-\bar{n}X$	not given
[53]	CLAS	$\gamma p \rightarrow \bar{K}^0K^+n$	< 0.8 nb
[54]	CLAS	$\gamma d \rightarrow K^+K^-p(n)$	< 0.3 nb

Table 1.2: Published experiments with non-observation for the Θ^+ baryon

---

[1] This result was denied by the same collaboration with high statistical experiment [54]. In the high statistical measurement, there was no significant structure in the mass spectrum of nK^+. Assuming that the histogram of the high statistical measurement represents the true shape of the background, the signal size estimate of 5.2σ from previous data decreases to 2.9σ.

[2] The search via the same reaction with high statistics by the CLAS collaboration reported a null result [53]. The 95% C.L. upper limit on the total cross section via $\gamma p \rightarrow \bar{K}^0K^+n$ reaction was set to be 0.8 nb.

1.3.1 Positive evidence for Θ^+

Experiments with tag of $S = +1$

At LEPS, the photo production of hadrons has been studied using photons with energies of $1.6 \sim 2.4$ GeV produced by Compton backscattering of laser photon from 8 GeV electrons in the SPring-8 storage ring. The produced charged hadrons are detected by a forward spectrometer. The Θ^+ was searched for via $\gamma n \to K^-\Theta^+ \to K^-K^+n$ reaction where the neutrons in ^{12}C nuclei in Start Counter were used as a target [8]. After the correction of Fermi motion of neutron, they showed a peak in mass distribution of K^+n system as shown in Figure 1.5 (1). They claim that the mass is 1540 ± 10 MeV/c^2 and the Gaussian significance of the peak is 4.6σ. The observed width is consistent with the experimental resolution of the spectrometer and the upper limit of 25 MeV/c^2 is reported.

The DIANA collaboration at ITEP searched for the Θ^+ independently of LEPS, according to the prediction by Diakonov *et al.*. Using K^+ beam and a Xe bubble chamber, they searched for the Θ^+ via K^+n charge exchange reaction, $K^+n \to K^0p$ [29]. The range of each K^+ beam was required to be larger than 550 mm, which corresponded to the mean K^+ momentum of 470 MeV/c at a reaction point. They collected 1,112 events of charged exchange reaction of $K^+\text{Xe} \to K^0_S p\text{Xe}'$. In order to reject events where the proton or K^0_S were affected by the final state interaction in the Xe nuclei, they applied a cut for the angle of the proton and K^0_S. From the invariant mass spectrum of the proton and K^0_S after these analyses, the narrow peak with the statistical significance of 4.4σ corresponding to the Θ^+ was obtained at 1540 ± 2 MeV/c^2 as shown in Figure 1.5 (2). The measured width was also consistent with the resolution and the upper limit of 9 MeV/c^2 has been obtained.

The CLAS collaboration at Thomas Jefferson Laboratory is one of the central places of the research for the photo production of the Θ^+. Photon beams were produced by 2.474 and 3.115 GeV electrons incident on a bremsstrahlung radiator of thickness of 10^{-4} radiation length. They have reported the exclusive measurement on deuterium for the reaction $\gamma d \to K^+K^-p(n)$ where the final state neutron is reconstructed from the missing momentum and energy [30]. The most advantageous feature of this measurement is that Fermi motion correction is not needed. In addition to the cut to eliminate other hadron resonances such as ϕ meson and $\Lambda(1520)$ resonance, the missing momentum was required to be greater than 0.20 GeV/c in order to remove spectator neutrons. Finally they obtained mass spectrum of the K^+n system showing a sharp peak at the mass of 1542 ± 5 MeV/c^2 with the width of 21 MeV/c^2 corresponding to the experimental resolution as shown in Figure 1.5 (3). The peak count is 43 and the statistical significance has been estimated to be $4.6 \sim 5.8$ σ depending on the background shape.

The exclusive measurement on a proton target for the $\gamma p \to \pi^+K^-K^+(n)$ reaction has also been reported by the CLAS collaboration [33]. The undetected neutron was selected from the missing mass of $\gamma p \to \pi^+K^-K^+X$ reaction and ϕ meson was eliminated. Moreover they required a cut of $\cos\theta^*_{\pi^+} > 0.8$, where $\theta^*_{\pi^+}$ is the center-of-mass angle between the π^+ and the photon beam. This cut corresponds to an enhancement of the t-channel process where the intermediate N^* state decays into Θ^+ and K^-. From the nK^+ mass spectrum which is shown in Figure 1.5 (5), a narrow baryon state with mass M = 1550 ± 10 MeV/c^2 and width $\Gamma < 26$ MeV/c^2 was observed. The peak's statistical significance is $(7.8 \pm 1.0)\sigma$.

The SAPHIR collaboration at ELSA has reported the evidence for the Θ^+ in photoproduction of $\gamma p \to nK^+K^0_S$ reaction [31]. The incident photons are produced by the

ELSA electron beam via bremsstrahlung in a copper foil radiator. The K_S^0 was identified from the invariant mass of π^+ π^- pair and the neutron was also selected from the missing mass. The Θ^+ baryon is seen as a peak in the nK^+ invariant mass distribution with a 4.8 σ confidence level as shown in Figure 1.5 (4). The observed mass is 1540 ± 4 ± 2 MeV/c^2 and an upper limit of the width $\Gamma < 25$ MeV/c^2 has been obtained.

The Θ^+ has been shown from the exclusive measurement of $pp \rightarrow \Sigma^+ K^0 p$ reaction by the COSY-TOF collaboration, where hyperon resonances are measured via proton-proton reaction using a liquid hydrogen target and proton beams of incident momentum of 2.95 GeV/c [36]. The K_S^0 was identified by the decay into $\pi^+\pi^-$ pair. The angle between the $\pi^+\pi^-$ pair was required to be larger than 12 degree to eliminate $\Lambda \rightarrow \pi^- p$ events kinematically. The Σ^+ was selected from the missing mass of $pp \rightarrow K_S^0 pX$ reaction. After the correction of the acceptance, they have showed a peak with the statistical significance of $4 \sim 6$ σ at the mass M=1530±5 MeV/c^2 in the mass distribution of $K^0 p$ subsystem as shown in Figure 1.5 (6). The production cross section of the proton-proton reaction has been estimated to be $0.4 \pm 0.1(\text{stat.}) \pm 0.1(\text{syst.})$ μb.

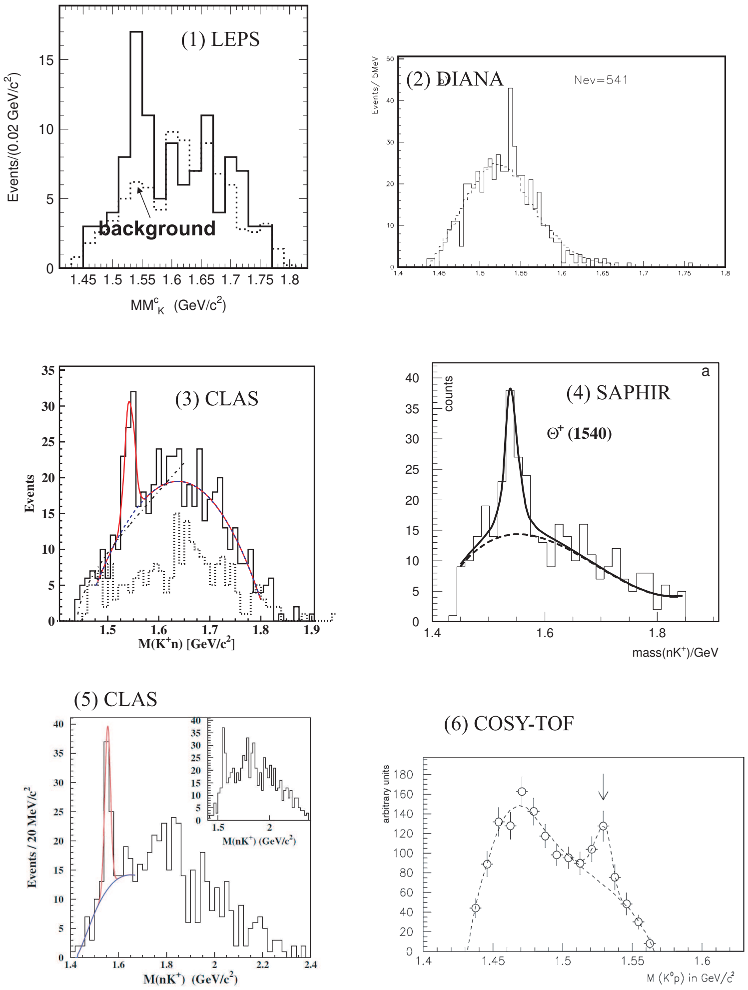

Figure 1.5: Experimental results with positive evidence where the positive strangeness is tagged.

The pK^0 experiments

Astratyan, Dologolenko and Kubantsev have reported a narrow peak in the mass distribution of pK_S^0 system produced via neutrino and anti-neutrino collisions with nuclei [32]. This is the re-analysis of past neutrino scattering data with big bubble chambers: WA21, WA25, WA59 (CERN) and E180, E632 (Fermilab). Three kinds of bubble chambers, hydrogen, deuterium and neon-hydrogen mix were used in these experiments. They have obtained the pK_S^0 mass distribution for the neon and deuterium data combined showing a narrow peak of 27 events at the mass of 1533±5 MeV/c^2 as shown in Figure 1.6 (1). Neutrino data do not allow one to determine the strangeness of the observed resonant state. They interpret the enhancement as a signal of the formation of the Θ^+, considering there are no known Σ^{*+} states in this mass region.

HERMES collaboration at DESY has reported the evidence for a narrow baryon state with $|S| = 1$ in quasi-real photo production on a deuterium target through the decay channel $pK_S^0 \rightarrow p\pi^+\pi^-$ [34]. The 27.6 GeV positron beams of the HERA storage ring interact on a longitudinally polarized deuterium gas target. The peak with the mass M=1528 $\pm$ 2.6(stat.) $\pm$ 2.1(syst.) and the width $\Gamma = 17 \pm 9$(stat.) $\pm$ 3(syst.) was observed in the mass distribution of pK_S^0 system as shown in Figure 1.6 (2).

The ZEUS collaboration also at DESY has reported the results of a search for the Θ^+ and the $\bar{\Theta}^-$ in the $K_S^0 p$ and $K_S^0 \bar{p}$ decay channels, respectively, in the central rapidity region of ep collision at center-of-mass energy of about 300 GeV [35]. The K_S^0 mesons were identified by their charged decay mode, $K_S^0 \rightarrow \pi^+\pi^-$. Protons and anti-protons were selected by the dE/dx distribution in the central tracking detector (CTD). They showed a peak structure in the mass distribution of $K_S^0 p$ and $K_S^0 \bar{p}$ systems at the mass of 1521.5 $\pm$ 1.5(stat.) GeV/c^2, when they selected events with 4-momentum transfers $Q^2 > 20$ GeV^2, as shown in Figure 1.6 (3).

The SVD collaboration measured the $pA \rightarrow pK^0X$ reaction using the 70 GeV proton beam at the IHEP [37]. In their analysis, events with no more than five charged particles from the primary vertex were analyzed to suppress the combinatorial background. The additional cuts were applied to momentum of proton (4 GeV/c $< P_p <$ 21 GeV/c) and the angle of the pK^0 system θ_{pK^0} at the center of mass frame ($\cos\theta_{pK^0} \leq 0$). As shown in Figure 1.6 (4), the invariant mass of the pK^0 system shows the excess at 1526 $\pm$ 3 MeV/c^2 above their background estimated by FRITIOF simulation in addition to the excess strength in the 1570∼1750 MeV/c^2 range, presumably due to Σ^{*+} resonance.

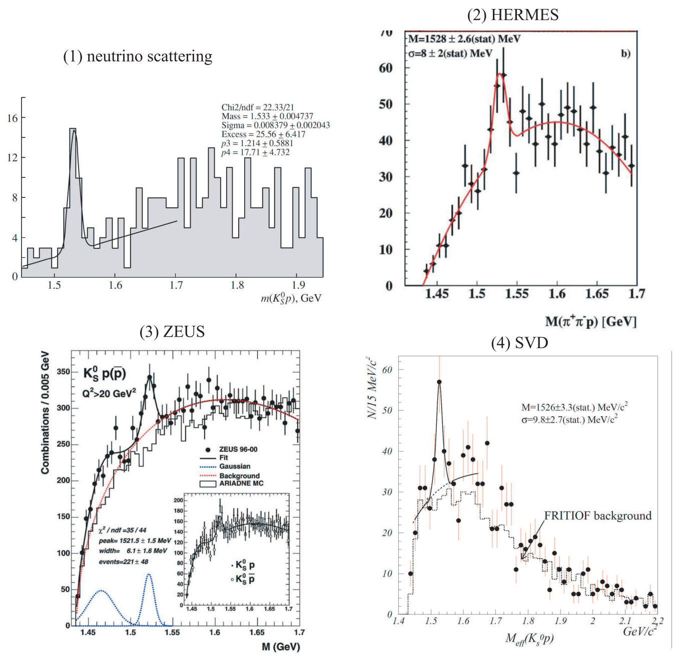
(1) neutrino scattering
(2) HERMES
(3) ZEUS
(4) SVD

Figure 1.6: Experimental results with positive evidence where the Θ^+ was searched for from the invariant mass of pK^0_S system.

1.3.2 Experiments with negative results

The reports of finding the exotic baryons such as the Θ^+ and the Ξ^{--} in low energy exclusive experiments have given the motivation for collaborations of high energy experiment to search for these objects. Naively, one might expect that these exotic baryons should be produced in high-energy experiments through fragmentation processes as the flux tube breaks when the struck quark exits the nucleon. The searches have been done in both e^+e^- annihilation experiments and the high-energy hadron beam experiments with much higher statistics and better detector resolution. In these experiments, mainly the inclusive measurements of K^0 and proton are reported and mass spectra of pK^0 system show no peak structure around the expected mass region of 1520 - 1560 MeV/c^2, while the ordinary hyperons such as $\Lambda(1520)$ or $\Xi(1530)$ are clearly seen. However, in these experiment many charged particles are produced in a interaction which make a huge combinatorial background. Moreover the Σ^{*+} resonances such as the $\Sigma(1670)$ are not seen. In this section, the null experiments are reviewed from the viewpoint of the e^+e^- experiments and hadron interaction experiments.

The e^+e^- experiments

The pentaquark production in e^+e^- annihilation needs at least 5 quarks and 5 anti-quarks from zero quark. Therefore experiments with a baryon in the beam or the target might have some advantage in pentaquark production. However e^+e^- interaction is also known for "democratic" production of hadrons. Baryons with nonzero beauty, charm, strangeness (up to three units) and/or orbital angular momentum have been observed with production rates that appear to depend on the mass and spin, but not quark content as shown in Figure 1.7. If pentaquarks are produced similarly, then one might expect a pentaquark rate as high as that for an ordinary baryon of the same mass and spin, i.e. about 8×10^{-4} Θ^+

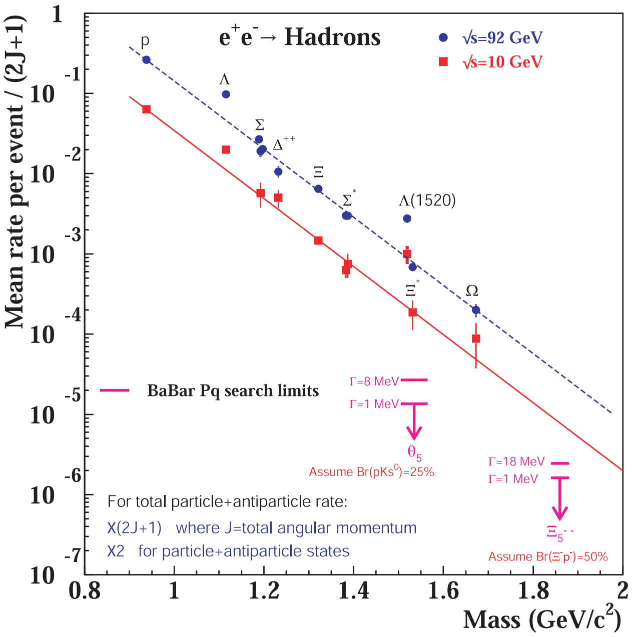

Figure 1.7: Baryon production rates in e^+e^- annihilation from experiments at the Z^0 (circles) and $\sqrt{s} \sim 10$ GeV (squares) as a function of baryon mass [42]. The vertical scale accounts for the number of spin and particle+antiparticle states, and the lines are chosen to guide the eye. The arrows indicate BABAR preliminary upper limits on spin-1/2 Θ^+ and Ξ^{--} pentaquark states, assuming the branching fractions shown, and are seen to lie below the solid line.

and about 4×10^{-5} Ξ^{--} per $e^+e^- \to$ hadrons event at $\sqrt{s} = 10.58$ GeV. Unfortunately anyone do not know whether this tendency of baryon production rate is applicable to pentaquark production.

The BABAR collaboration has shown the results of inclusive searches for the Θ^+ in data from the BABAR experiment at $\sqrt{s} = 10.58$ GeV, which includes both $e^+e^- \to q\bar{q}, q = udsc$, events and the production of $\Upsilon(4S)$ mesons, which decay into $B\bar{B}$ pairs [43]. They searched for the Θ^+ from the invariant mass of the pK^0_S system, where $K^0_S \to \pi^+\pi^-$. The invariant mass spectra are shown in Figure 1.8, where there is a clear peak at 2285 MeV/c^2 from $\Lambda_c^+ \to pK^0_S$ but no other sharp structure. The 95% CL upper limits on the yield per $q\bar{q}$ event and $\Upsilon(4S)$ decay have been obtained to be $5.0\times\ 10^{-5}$ and $18\ \times\ 10^{-5}$ assuming that the width of the Θ^+ is 1 MeV/c^2 and the branching ratio of the Θ^+ decay to $K^0_s p$ is 1/4. This results are roughly a factor of eight below the typical values measured for ordinary octet and decuplet baryons as shown in Figure 1.7.

The ALEPH collaboration has searched for the exotic baryons in the fragmentation of quarks from four million hadronic Z decays as a narrow peak in the invariant mass of combinations of reconstructed K^0_S and proton tracks with the resolution better than 5 MeV/c^2 [45]. They have set the 95% C.L. upper limit on the production rate times branching ratio of the Θ^+ and its antiparticle per hadronic Z decay to be $N_{\Theta^+} \cdot \mathrm{Br}(\Theta^+ \to pK_S) < 6.2 \times 10^{-4}$, which yields $N_{\Theta^+} < 0.0025$ assuming that the branching ratio is 25%. On the other hand, the production rate of $\Lambda(1520)$ per hadronic Z decay is found to be

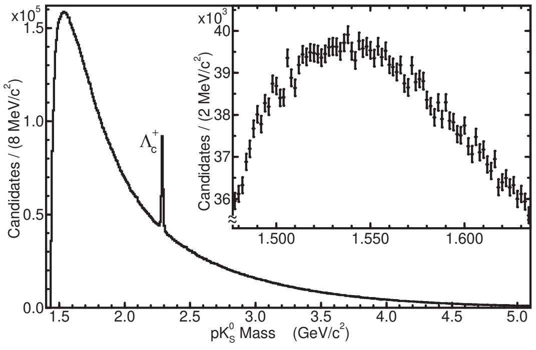

Figure 1.8: Distribution of the pK^0_S invariant mass obtained by the BABAR collaboration [43]. The sharp peak corresponding to Λ_c^+ is clearly recognized. The same data are plotted for the mass range around 1540 MeV/c^2.

$N_{\Lambda(1520)} = 0.033 \pm 0.004 \pm 0.003$.

The Belle collaboration has reported the upper limit of the production rate of the Θ^+ through the $B^0 \to \Theta^+ \bar{p}$ decay following $\Theta^+ \to K^0_S p$ using data sample recorded on the $\Upsilon(4S)$ resonance at the KEKB asymmetric energy e^+e^- collider [44]. They obtained the 90% confidence level upper limit of $Br(B^0 \to \Theta^+ \bar{p}) \cdot Br(\Theta^+ \to pK^0_S) < 2.3 \times 10^{-7}$.

High-energy hadron beam experiments

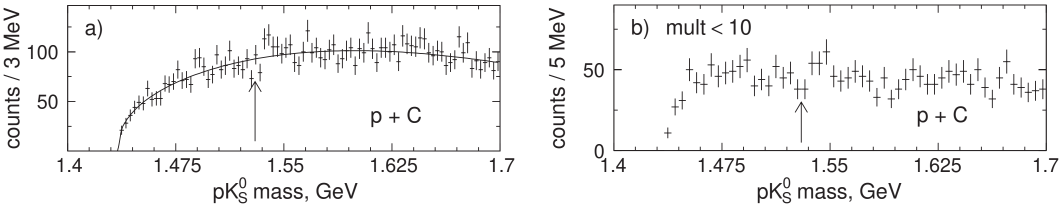

Figure 1.9: The pK^0_S invariant mass distributions obtained by HERA-B collaboration [46]. (a) data from the $p+C$ collisions and the background estimate (continuous line). (b) same data with requirement that a track multiplicity is less than 10.

HERA-B is a fixed target experiment at the 920 GeV proton storage ring at DESY utilizing a forward magnetic spectrometer with a large acceptance centered at mid-rapidity. They have searched for the Θ^+ from the pK^0_S decay in proton-nucleus collisions at $\sqrt{s} =$ 41.6 GeV using carbon, titanium and tungsten wire targets [46]. The invariant mass spectrum of the pK^0_S pairs is shown in Figure 1.9 for the $p+C$ data with the background determined from the event mixing. The distribution is smooth shape. The 95% C.L. upper limit of the particle ratio $\Theta^+/\Lambda(1520)$ at mid-rapidity ($y_{cm} \sim 0$) is obtained to be 2.7%.

The SPHINX collaboration has performed a search for the Θ^+ in a proton-induced reaction $p + C(N) \to \Theta^+ \bar{K^0} + C(N)$ on carbon nuclei at 70 GeV studying nK^+, pK^0_S and pK^0_L decay channels of the Θ^+ where K_L's and neutrons were detected in their calorimeter [47]. The performance of the calorimeter to detect the neutral particles was studied by reconstructing $\Lambda(1520) \to nK^0_S$ and $\phi \to K^0_L K^0_S$ decays. There was no significant structure in all invariant mass spectra of nK^+, pK^0_S and pK^0_L channels as shown in Figure 1.10. They have set an upper limit of particle ratio $\Theta^+/\Lambda(1520)$ to be less than 0.02 at 90% C.L..

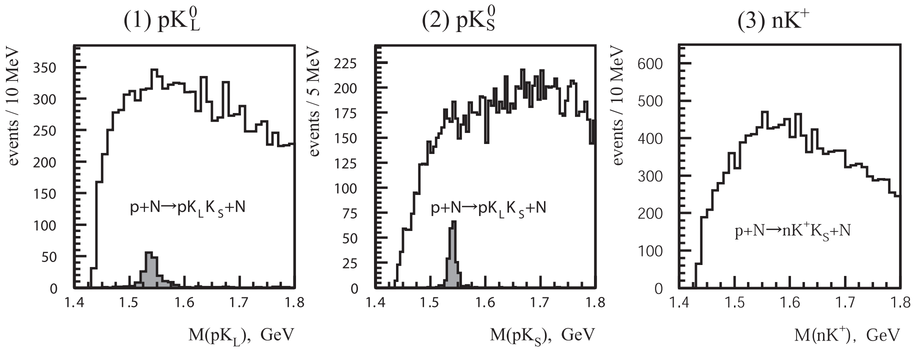

Figure 1.10: The mass spectra of (1) pK_L^0, (2) pK_S^0 and (3) nK^+ obtained by SPHINX collaboration [47]. The shaded histograms are Monte Carlo simulations.

The HyperCP experiment is designed principally to investigate CP violation in $\Xi^-/\bar{\Xi}^+$ decays produced by 800 GeV protons interacting in a copper target. In this experiment, there was a tungsten collimator just downstream of the copper target to select charged particles with momenta from about 120 to 220 GeV/c. However over a half of the triggered data were from events produced in the tungsten near the exit of the defining collimator and these events were used in the pentaquark search [48]. This experiment did not have particle identification. The K_S^0 mesons are reconstructed from the two charged particles with the opposite charges. Protons are selected by requiring charged tracks with $> 50\%$ of the total momentum. In the total sample of 106,000 $K_S^0 p$ and $K_S^0 \bar{p}$ candidates, there is no sign of a peak near 1.54 GeV/c^2. They find that the number of the Θ^+ is less than 0.3% of the $K_S^0 p$ candidates.

1.4 Search for the Θ^+ baryon with meson beams

As reviewed in the previous section, the present status of the Θ^+ is controversial. There are more than ten experiments which indicated the evidence of the Θ^+, while similar number of experiments claim the null results. In such a situation, the confirmation of existence (or non-existence) of the Θ^+ is urgent and crucially important.

It is true that the statistics in all experiments with positive results is not sufficient to claim a clear observation of the Θ^+, while several high-energy experiments report the null results obtained from searches with much higher statistics and better resolution. However Titov et al., using quark constituent coupling rules, shows that the production of the Θ^+ is suppressed relative to the $\Lambda(1520)$ resonance by about three orders of magnitude for high energy experiments [55]. Therefore, in order to confirm the existence of the Θ^+, high statistics experiments at low energy region with hadronic reaction become crucial. Many experimental data of the Θ^+ searches are from photo-production experiments. In general the Θ^+ production cross section via hadronic reaction is expected to be much larger than that via photo-induced reaction. Now, physical properties such as spin, parity and width have not been determined experimentally yet. The narrow width of the Θ^+ is the remarkable characteristics. The width of a few MeV or less is expected from the K^+-nucleon scattering data and is unusually narrow as a hadron resonance of which typical width is several ten MeV. The suppression of decay to KN mode might be related to the internal structure of the Θ^+. Therefore determination of spin and parity is indispensable to understand the reason of the narrowness. The measurement of these values needs more statistics. From these viewpoints, the study of the Θ^+ production using meson beam such

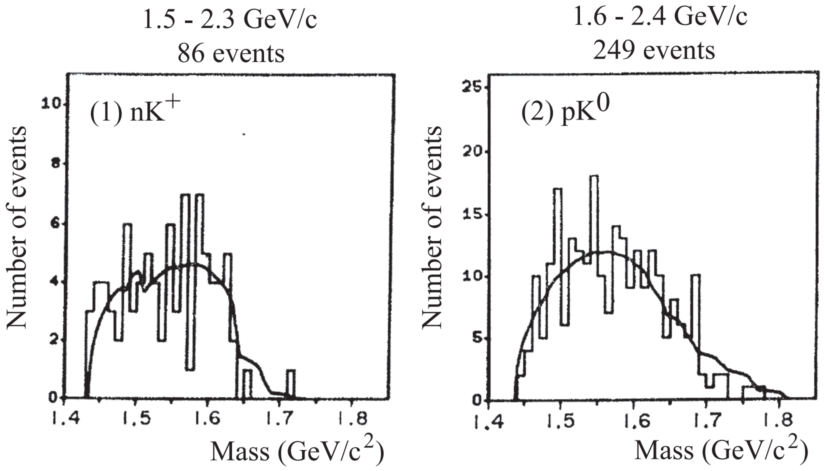

Figure 1.11: Invariant mass spectra of (1) nK^+ and (2) pK^0 produced by $\pi^- p$ reactions at π^- beam momentum of 1.5 - 2.4 GeV/c measured in the past bubble chamber experiment [56]. Although the statistics is poor, there is no structure around 1.54 GeV/c^2.

as π^- and K^+ is essential. Therefore we carried out an experiment to search for the Θ^+ via $\pi^- p \to K^- \Theta^+$ reaction. In this reaction, the threshold momentum is 1.71 GeV/c. We used 1.87 and 1.92 GeV/c π^- beam.

The $\pi^- p \to K^- X$ reaction near the Θ^+ production threshold was studied in 1960s using a bubble chamber [56]. The main backgrounds of the (π^-, K^-) reaction are ϕ production, $\Lambda(1520)$ production and 3-body phase space as following.

$$\phi \text{ production} : \pi^- p \;\to\; \phi n \to K^- K^+ n \qquad (\sigma = 30.0 \pm 8.0 \mu\text{b}) \tag{1.1}$$

$$\Lambda(1520) \text{ production} : \pi^- p \;\to\; \Lambda(1520) K^0 \to K^- K^0 p \quad (\sigma = 20.8 \pm 5.0 \mu\text{b}) \tag{1.2}$$

$$\text{phase space} : \pi^- p \;\to\; K^-(K^+ n / K^0 p) \qquad (\sigma \sim 25 \mu\text{b}) \tag{1.3}$$

The cross sections of these reactions were measured to be $30.0 \pm 8.8 \mu\text{b}, 20.8 \pm 5.0 \mu\text{b}$ and $\sim 25 \mu\text{b}$ respectively at beam momenta from 1.8 to 2.2 GeV/c. It is remarkable feature that in this momentum range the background is small because other channels do not open. In the past experiment the invariant masses of nK^+ and pK^0 were surveyed as shown in Figure 1.11. Any peak structure was not observed. However numbers of nK^+ and pK^0 events were only 86 and 249 respectively.

1.4.1 Theoretical calculation of the production cross section via $\pi^- p \to K^- X$ reaction

The understanding of production mechanism is quite important to understand the Θ^+. Therefore a measurement of the production cross section with a simple reaction is important experimentally. Theoretical calculations with hadronic models using effective interaction Lagrangians and form factors have been made by several authors [57, 58, 59, 60]. They try to understand the Θ^+ production mechanism via $\gamma N, NN, KN$ and πN reactions near the production threshold comprehensively.

For the calculation of the cross section via the $\pi^- p \to K^- \Theta^+$ reaction, the diagrams shown in Figure 1.12 were taken into account. The parity of the Θ^+ was assumed to be positive. Then the effective Lagrangians are

$$\mathcal{L}_{KN\Theta} \;=\; -i g_{KN\Theta} (\bar{\Theta} \gamma_5 K^+ n - \bar{\Theta} \gamma_5 K^0 p) + \text{H.c.} \tag{1.4}$$

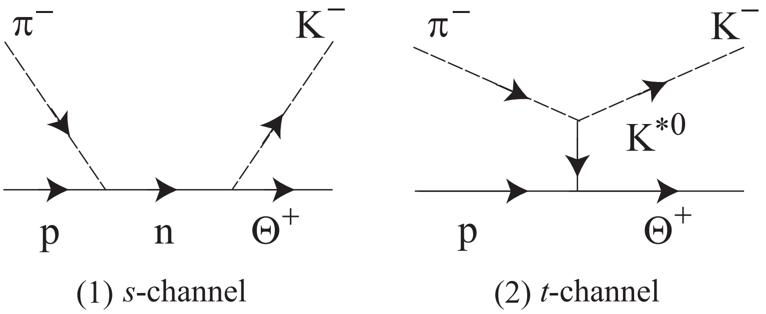

Figure 1.12: Diagrams for $\pi^- p \to K^- \Theta^+$ reaction.

$$\mathcal{L}_{\pi NN} = -ig_{\pi NN}\bar{N}\gamma_5\pi N \tag{1.5}$$

for the s-channel. For the K^* exchange, they used

$$\begin{aligned}\mathcal{L}_{K^*N\Theta} &= -g_{K^*N\Theta}(\bar{\Theta}\gamma^\mu K_\mu^{*+}n - \bar{\Theta}\gamma^\mu K_\mu^{*0}p) + \text{H.c.}\\ \mathcal{L}_{K^*K\pi} &= -ig_{K^*K\pi}\bar{K}\partial^\mu\pi K_\mu^* - \partial^\mu\bar{K}\pi K_\mu^* + \text{H.c..}\end{aligned} \tag{1.6}$$

In order to calculate the cross section using this formalism, the coupling constants should be determined. The coupling constant $g_{K^*K\pi}$ fixed by the experimental data for $K^* \to K\pi$ decay,

$$\Gamma_{K^*\to K\pi} = \frac{g_{K^*K\pi}^2}{2\pi M_{K^*}^2}|\mathbf{P}_\pi|^3, \tag{1.7}$$

is $g_{K^*K\pi} = 3.2$. They also used $g_{\pi NN}^2/(4\pi) = 14$ [61]. The coupling term of the Θ^+ is also estimated from the decay width as follows. The Lagrangian $\mathcal{L}_{KN\Theta}$ gives the decay width of $\Theta^+ \to KN$ as

$$\Gamma_{\Theta^+\to K^+n+K^0p} = \frac{g_{KN\Theta}^2}{2\pi}\frac{|\mathbf{P}_K|(\sqrt{M_N^2+\mathbf{P}_K^2}-M_N)}{M_\Theta}, \tag{1.8}$$

where M_N and M_Θ are the nucleon and Θ^+ masses, respectively, and $\mathbf{P}_K$ is the momentum of the kaon in the Θ^+ rest frame [3]. The authors determined the value of $g_{KN\Theta}$ considering the experimental upper limit of width around 9–25 MeV/c^2 and the KN scattering analysis. Concerning the coupling $g_{K^*N\Theta}$, there is no experimental information, since the decay of the Θ^+ into K^*N is not kinematically allowed. The only hint they used is that coupling constants for the ordinary hyperon production, $g_{K^*N\Lambda}$ and $g_{K^*N\Sigma}$, are ~-4.5 and ~-2.6, respectively, which are smaller than $g_{KN\Lambda}$ and $g_{KN\Sigma}$ by a factor of 2.4−3.5 or 1.2−1.8 [62]. From this observation, they expect that $g_{K^*N\Theta}$ would be smaller than $g_{KN\Theta}$. However, their relative phase is still unfixed. Thus, they treated $g_{K^*N\Theta}$ as a free parameter from $-g_{KN\Theta}$ to $g_{KN\Theta}$.

In order to estimate the realistic value of the cross section, form factors are needed at interaction vertices to take into account the finite sizes of hadrons. They adopt the

---

[3] In case of negative parity, the decay width Γ and coupling constant $g_{KN\Theta}$ are connected with the following equation,

$$\Gamma = \frac{g_{KN\Theta}^2}{2\pi}\frac{|\mathbf{P}_K|(\sqrt{M_N^2+\mathbf{P}_K^2}+M_N)}{M_\Theta}. \tag{1.9}$$

For example this equation gives $g_{KN\Theta} = 0.307$ with $\Gamma = 5$ MeV/c^2, which is about ten times lower than that for positive parity ($g_{KN\Theta} = 2.2$ with $\Gamma = 5$ MeV/c^2 for positive parity). Therefore if the parity is negative, the cross section is suppressed compared with that for positive parity.

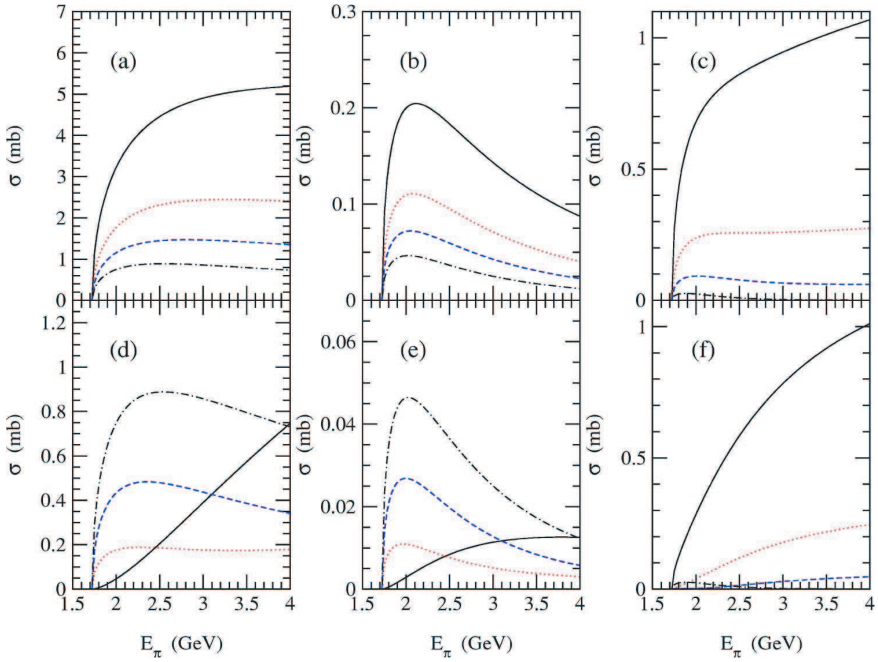

Figure 1.13: Calculated cross sections for the $\pi^- p \to K^- \Theta^+$ reaction by Y. Oh *et al.* [58]. The (a,d) are the results without form factor, (b, e) are that with the form factor of equation (1.10) with $\Lambda = 0.5$ GeV, and (c, f) are that with other form factor (See Reference [58]). In (a, b, c), the solid, dotted, dashed, and dot-dashed lines are with $g_{K^*N\Theta} = -2.2, -1.1, -0.5$ and 0.0, respectively. In (d, e, f), the solid, dotted, dashed, and dot-dashed lines are with $g_{K^*N\Theta} = 2.2, 1.1, 0.5$ and 0.0, respectively.

monopole form factor, which is a function of $\sqrt{s}$ only,

$$F(s) = \frac{\Lambda^2}{\Lambda^2 + \mathbf{q}_i^2}, \tag{1.10}$$

where Λ is the cut off parameter and $\mathbf{q}_i$ is the three-momentum of the initial state particles in the center of mass frame. The cut off parameter is taken to be $\Lambda = 0.5$ GeV based on fitting the measured cross section for the reaction $\pi N \to K\Lambda$ using similar hadronic Lagrangians [63].

In Reference [57], Liu and Ko calculated the cross section taking into account only the s-channel diagram. They used $g_{KN\Theta} = 4.4$, which corresponds to 20 MeV/c^2 width of the Θ^+. They predict that the cross section is about 50 μb. In this framework, the cross section is controlled by the $g_{KN\Theta}$ which is determined from the width by equation (1.8), because they take into account the only s-channel diagram. Therefore the cross section is proportional to the width of the Θ^+, since both the cross section and the width are proportional to $g^2_{KN\Theta}$. If the width is less than 20 MeV/c^2, smaller cross section will be obtained.

Y. Oh *et al.* calculated the cross section taking into account the s-channel diagram and the t-channel diagram where a K^* is exchanged [58]. They used $g_{KN\Theta}$=2.2, which corresponds to 5 MeV/c^2 width of the Θ^+, and the same cutoff value used by C. M. Ko *et al.*. Because there is no experimental information about $g_{K^*N\Theta}$, they used several values from -2.2 to 2.2 as $g_{K^*N\Theta}$. Figure 1.13 shows their results obtained without form factor (a, d), with form factor of equation (1.10) (b, e) and with other type of form factor (c, f) (See Reference [58]). The top ones, (a, b, c), show the calculations using

$g_{K^*N\Theta} = -2.2, -1.1, -0.5$ and 0.0. The bottom ones, (d, e, f), show the calculations using $g_{K^*N\Theta} = 2.2, 1.1, 0.5$ and 0.0. Due to the interference between the amplitudes of s-channel and t-channel, the cross section of the $\pi^-p \rightarrow K^-\Theta^+$ reaction is quite dependent on the magnitude of $g_{K^*N\Theta}$. When they used the form factor of equation (1.10), the calculated cross section ranges from about 2 μb to 190 μb as shown in Figure 1.13 (b, d). Therefore they mention that this reaction is suitable to give a guide to estimate the magnitude of $g_{K^*N\Theta}$.

In these calculations, the parameters which are not determined experimentally such as $g_{KN\Theta}$ and $g_{K^*N\Theta}$ are used. Therefore these calculation should be compared with experimental cross section. As mentioned above, the total cross section is dependent on the decay width, because both of them is related to coupling constant $g_{KN\Theta}$. Experimental information on total cross section is important to determine the decay width, or vise versa.

1.4.2 KEK-PS E522 experiment
– Search for the Θ^+ baryon via $\pi^-p \rightarrow K^-X$ reaction –

The present E522 experiment has been carried out at the K2 beam line of the KEK 12 GeV Proton Synchrotron in November 2002 and March 2004 [4]. We took $\pi^-p \rightarrow K^-X$ data with the motivation of the confirmation of the existence of the Θ^+. Now the K2 beam line is a unique beam line which can provide up to 2 GeV/c π beam and enables us to study the Θ^+ with this reaction near the production threshold. We used a π^- beam of 1.87 and 1.92 GeV/c. As a target, we used a scintillation fiber (SCIFI) target ($(CH)_n$) and a bulk target of polyethylene ($(CH_2)_n$).

In this thesis, we present the production cross section via $\pi^-p \rightarrow K^-\Theta^+$ reaction obtained from the present experiment.

---

[4] The main objective of this experiment was to search for H-dibaryon resonance with (K^-, K^+) reaction. We searched for the enhancement at the threshold region of the double-Λ system, which was first measured at KEK-PS E224 experiment [64], with much better statistics [65]. The (K^-, K^+) data was taken in November 2002. The (π^-, K^-) data to search for the Θ^+ was taken in March 2004.

Chapter 2

Experiment

2.1 Overview

We have performed the E522 experiment at the K2 beam line of KEK 12 GeV Proton Synchrotron in 2004. The main objective of this experiment was to search for H-dibaryon resonance with (K^-, K^+) reaction. At KEK-PS E224 experiment, the enhancement was observed at threshold region of the double-Λ system [64]. In the present experiment we searched for this enhancement, which was a candidate of H-dibaryon resonance, with ten times larger statistics [65]. Besides this reaction, we optionally took $\pi^- p \rightarrow K^- X$ data, because the search for the Θ^+ via mesonic reaction became crucial to confirm its existence and the K2 beam line was a unique beam line which could provide up to 2 GeV/c π beam.

We used π^- beams of 1.87 and 1.92 GeV/c. As a target, we used a scintillation fiber (SCIFI) target ($(\mathrm{CH})_n$) and a bulk target of polyethylene ($(\mathrm{CH}_2)_n$). The SCIFI target was 20 cm long, and was the same one used in the hyperon-nucleon scattering experiment (KEK-PS E289) [66]. It was mainly used to detect decay particles from $^{12}\mathrm{C}(K^-, K^+\Lambda\Lambda)$ reaction for the H-dibaryon resonance search. For (π^-, K^-) data, we mainly used the 10 cm long polyethylene target to enhance the contribution from free protons. The SCIFI target was also used to detect tracks of the charged particles other than K^- produced by reactions. At the beam momentum of 1.87 GeV/c, 2.9×10^9 and 3.0×10^9 π^- beam particles were irradiated to the SCIFI and the polyethylene targets, respectively. At 1.92 GeV/c, 7.4×10^9 π^- beam particles were irradiated to only the polyethylene target. For the calibration we took the following data. In order to estimate the contribution from carbon in the SCIFI and polyethylene targets, we took data with a carbon target. The (π^+, K^+) data were analyzed to measure Σ^+ peak position for the calibration of the missing mass spectrum.

The experimental setup consisted of two parts; one part was a beam line spectrometer to analyze momentum of each incident beam particle and the other part was a forward spectrometer to detect scattered particles.

The K2 beam line is designed to transport charged particles up to 2.0 GeV/c. Figure 2.1 (a) shows the beam line spectrometer. The π^- beam was bent by 15 degree at the bending magnet (D2) and focused at the target by two quadrapole magnets (Q6, Q7). The typical intensity of π^- was 3.3×10^5 counts during 2 sec. spill with primary proton beam of 1.1×10^{12}. This intensity was determined by adjusting the acceptance slit and the momentum slit considering the memory size of the memory module (MP) used in the data acquisition system. Each beam particle was defined by the hit of T1 and T2 counters placed about 7.2m apart each other and π^- was selected at a trigger by two aerogel Čerenkov counters (BAC1,2), of which threshold velocity was 0.971, placed just upstream of the T2 counter. The beam momentum was analyzed with 5 wire chambers placed upstream and

(a) Beam line setup

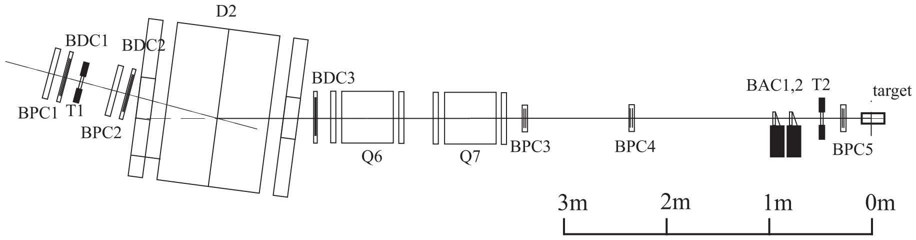

(b) KURAMA spectrometer setup

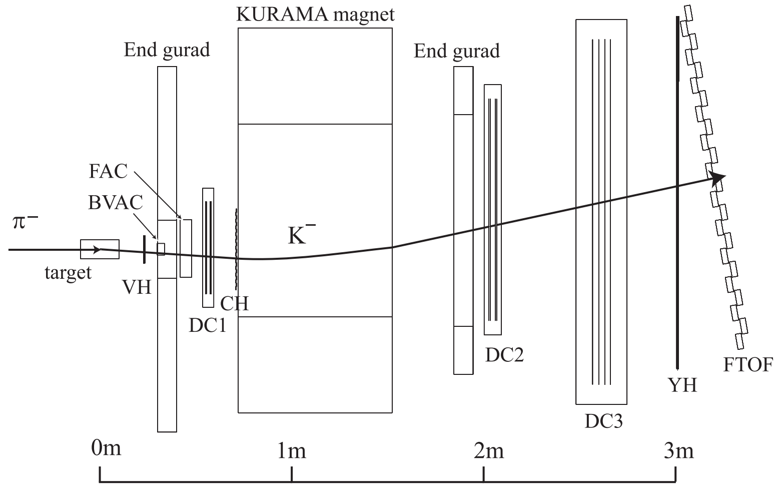

Figure 2.1: The schematic view of E522 experimental setup.

downstream of the D2 magnet. The momentum resolution is estimated to be $\sigma(p) = 8.9$ MeV/c from a simulation. Between two quadrapole magnets (Q6, Q7) and the target, 3 proportional chambers were placed to measure the beam direction. The timing for all detectors was determined by the T2 counter.

The scattered particles were detected by the forward spectrometer shown in Figure 2.1 (b). The KURAMA magnet is 80 cm long and magnetic field strength is 0.93T. The momentum of each scattered particle was measured using 3 drift chambers (DC1,2,3) and scintillation hodoscopes (VH, CH) placed upstream and downstream of KURAMA. The momentum resolution is 1.9 % (r.m.s.) for 0.8 GeV/c K^-. The time-of-flight of each scattered particle was measured by a TOF wall (FTOF) placed at end of the spectrometer. A typical time resolution was 132 ps. Two Čerenkov counters (BVAC, FAC) were installed between the target and KURAMA to veto π^-. Besides this particle identification with these Čerenkov counters at trigger level, we selected the charge and momentum range of each scattered particle at 1st trigger level using the hit combination of each segments of CH hodoscope and FTOF. Momentum of each particle was determined using the hit combination. By combining time-of-flight information of the hit FTOF segment with this momentum information, the mass of scattered particle was calculated. We selected K^- with this mass trigger (MT) at the 2nd trigger level. This mass trigger rejected mainly π^- which survived due to the inefficiency of the Čerenkov counters.

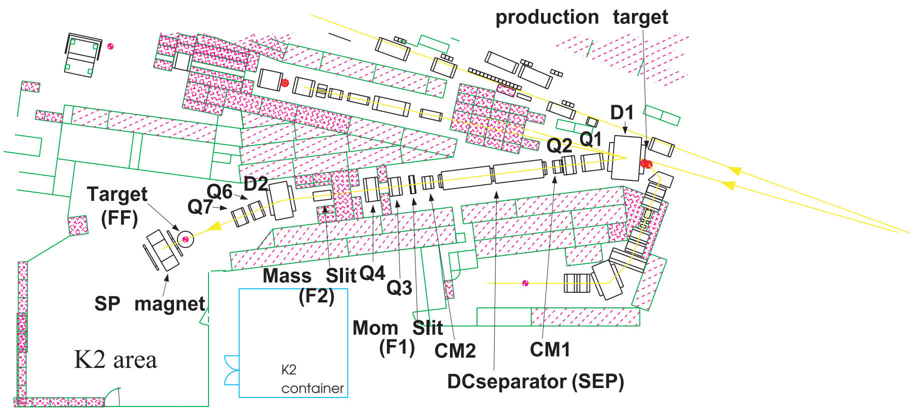

Figure 2.2: Layout of the K2 beam line at KEK 12 GeV proton synchrotron.

2.2 K2 beam line

In a 12 GeV proton synchrotron, the protons were first accelerated in a Cockcroft-Walton (to 750 keV), and then in a linac (to 40 MeV), before they were injected into the booster. From the booster, after acceleration, the 500 MeV protons were eventually injected into the main ring in which they got accelerated to energies of 12 GeV. This experiment was conducted at East Counter Hall, where proton beams were extracted slowly to the EP2 beam line during 2 sec in a 4 second cycle. The accelerated protons were delivered to the production target in the EP2-A beam line to produce the secondary particles such as pions and kaons into the K2 beam line. The zero degree production of the secondary particles was chosen in order to optimize the production rate of secondary particles from the primary protons incident on the nuclear target.

The K2 beam line was designed to optimize three important characteristics of low energy kaon beam, i.e. the kaon beam intensity, the mass separation quality and the optical beam quality [67]. It consists of two dipole magnets, D1 and D2, six quadrupole magnets, Q1-Q4 and Q6-Q7, a sextupole magnet, SX, an electromagnetic separator, SEP, a pair of vertical correction magnets, CM1 and CM2. The secondary beam starts from the production target. The first dipole magnet (D1) separates the secondary beam from the primary beam and deflects the secondary beam with the angle of 23 degree. The pair of quadrupole magnets (Q1, Q2) transform the beam parallel vertically and focus the beam horizontally at F1 where the momentum slit is located. The second quadrupole magnet doublet (Q3, Q4) focuses the beam vertically at F2, where the mass slit is placed. Finally the beam is focused horizontally and vertically at the final focus (FF) by the final quadrupole magnet doublet (Q6, Q7). The beam size at the FF, that is the experimental target, is shown in Figure 2.3. The sextupole magnet, SX, is placed to minimize the chromatic aberration at F2. The unwanted particles are deflected from the central beam orbit by the electric field of the electrostatic separator (SEP) with the aid of the correction magnets CM1 and CM2. The SEP has 6 m length, and was operated with ± 300 kV for kaon beam and ± 150 kV for pion beam between the positive and negative electrodes. The gap of the electrodes is 10cm and filled with a mixture of Ne (64 %) and He (36 %) gases with the pressure of 2×10^{-4} Torr typically.

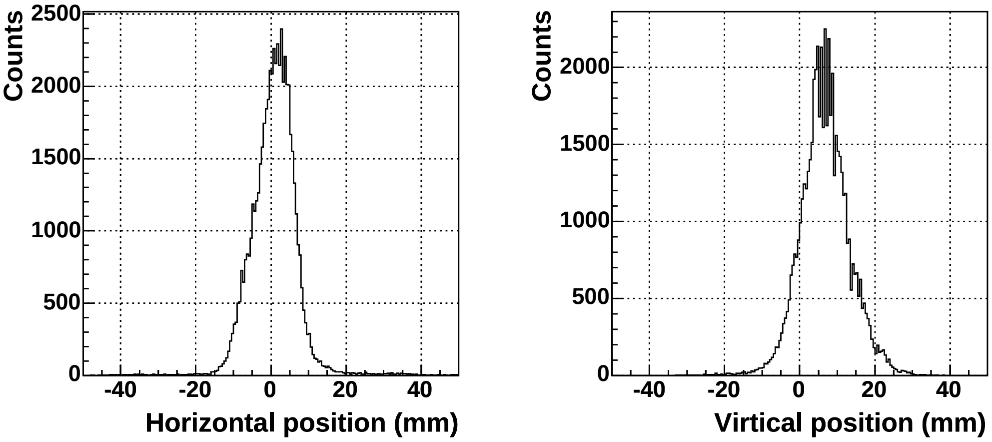

Figure 2.3: Typical beam profile at the experimental target.

anode wire spacing	1 mm	
anode wire diameter	10 μm	
anode wire material	Au-plated W	
cathode material	graphite	
operation voltage	4 kV	
gas mixture	Ar 75.3%, Isobutane 23.7%, Freon 1.0%	
	active area (mm × mm)	efficiency %
BPC1	112 (x) × 64 (y)	X:94.6 / Y 89.6
BPC2	112 (x)	X:99.8
BPC3	112 (x) × 64 (y)	X:92.1 / Y:95.4
BPC4	112 (x) × 64 (y)	X:96.2 / Y:99.2
BPC5	80 (x) × 64 (y)	X:98.2 / Y:98.2

Table 2.1: Specifications of the BPCs

sense wire spacing	5 mm	
sense wire diameter	10 μm	
potential wire voltage	1.5 kV	
cathode plane voltage	1.45 kV	
gas mixture	Ar 80%, Isobutane 20%	
	active area (mm × mm)	efficiency %
BDC1	160 mm (x and x’)	X:77.3/ X’:54.1
BDC2	160 mm (x and x’)	X:99.3/ X’:84.3
BDC3	160 mm (x and x’)	X:97.2/ X’:81.6

Table 2.2: Specifications of the BDCs

2.3 Beam line spectrometer

The K2 beam line is designed to transport the charged particles up to 2.0 GeV/c beam momentum. Figure 2.1 (a) shows the setup of the beam line spectrometer which consists of two scintillation counters (T1, T2) and two aerogel Čerenkov counters (BAC1, 2) for the particle identification and five proportional chambers (BPC1 - 5) and three drift chambers (BDC1 - 3) to measure the momentum and the direction at the target of each beam particle.

The T1 and T2 were made of the plastic scintillators (Bicron BC418), of which sizes were 5-mm thick, 5-cm high and 10-cm and 5-cm wide, respectively. Scintillation lights were collected by fast photo-multipliers (PMTs), HAMAMATSU H2431-50 from both horizontal ends. These counters were placed about 7.2 m apart each other (T1 was placed upstream of D2 and T2 was placed just upstream of a target), and were mainly used to measure the time-of-flight of each incident particle. The obtained time-of-flight resolution was 70 ps (r.m.s). The T2 also served as the start counter which determined the trigger timing.

The two aerogel Čerenkov counters, BAC1 and BAC2, were installed just upstream of T2 for the particle identification of beam particles at the trigger level. Figure 2.4 shows the schematic view and the photograph of BAC1, 2. Each of them consisted of a hydrophobic-silica-aerogel block, with the size of 10 cm (wide) × 7 cm (high) × 3 cm (thick) for BAC1 and the size of 8 cm (wide) × 8 cm (high) × 3 cm (thick) for BAC2. The index of the aerogel was 1.03, which corresponded to the threshold velocity of $\beta = 0.971$ for Čerenkov radiation. In the (K^-, K^+) trigger, these counters were used as a veto to reject lighter particles (π, μ, e) than K^- mesons. In the (π^-, K^-) trigger, these were used as a coincidence.

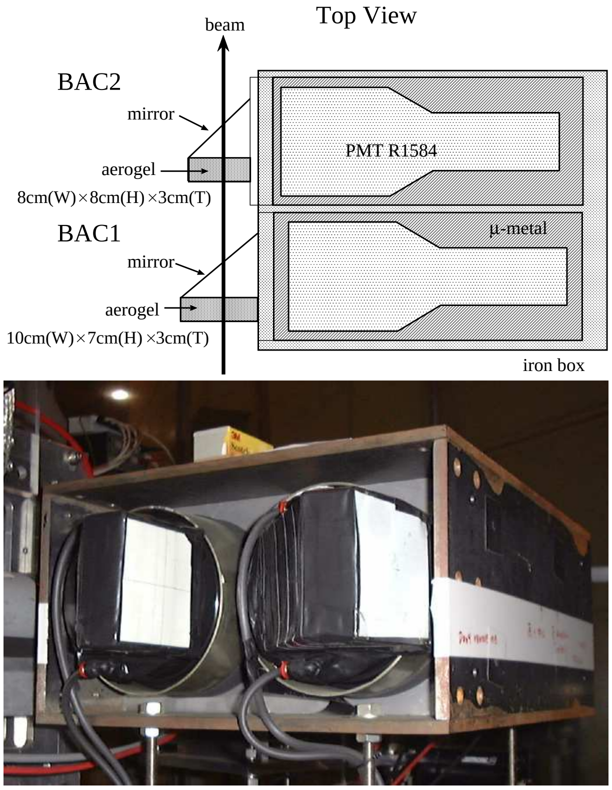

Figure 2.4: Schematic view (up) and photograph (down) of BAC1, 2.

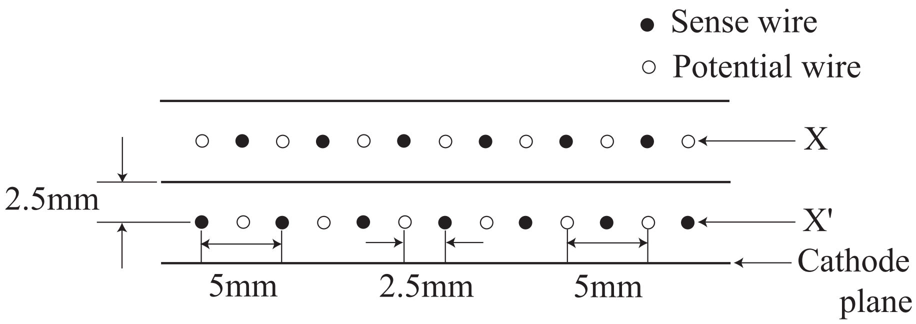

Figure 2.5: The cell structure of BDC's.

For the tracking detectors for beam particles, five multi-wire proportional chambers (BPC1 - BPC5) and three multi-wire drift chambers (BDC1 - BDC3) were used. Each of BDCs had two planes, X and X', whose cell structure is shown in Figure 2.5. Mixed gas of argon (80%) and isobutane (20%) was used. BPC1, BDC1, BPC2 and BDC2 were placed upstream of the D2 magnet. BDC3 was placed between the exit of the D2 magnet and the entrance of the Q6 magnet. These chambers were used to analyze the momentum of each incident particle. BPC3, BPC4 and BPC5 were placed between the exit of the Q7 magnet and the target, and these chambers were used to measure the beam directions and the reaction vertex points. Their specifications are summarized in Table2.1 and 2.2. The efficiencies of BDCs were significantly low due to the dead channels of the readout electronics. Figure 2.6 shows the beam profile of BDC3. For the tracking at the entrance of the D2 magnet, there were some redundancies (6 (total planes) - 2 (parameters)) to solve the straight track by fitting the position information. Therefore the efficiency to find the upstream track was typically 96.0%. However, in order to analyze the momentum of each incident particle we had to connect the upstream track to BDC3 which needed the both hits at X and X' planes to solve the left-right ambiguity. Therefore the inefficiency of BDC3 led up to the inefficiency of the momentum analysis of beam particles directly as described in Section 3.9.2.

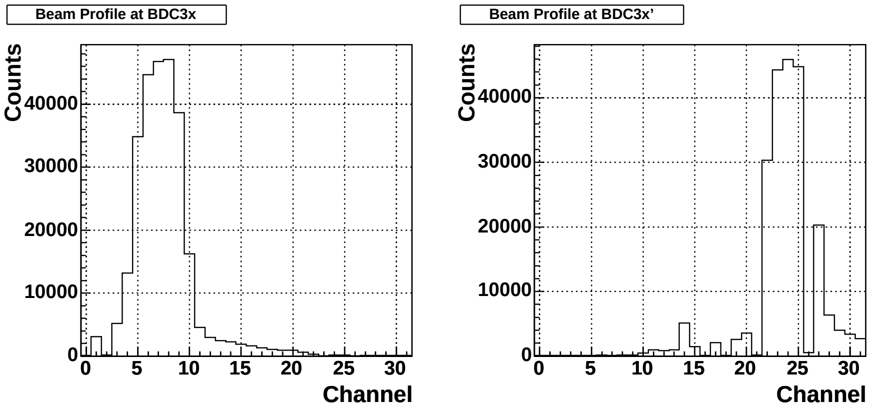

Figure 2.6: Typical beam profile at BDC3 X (left) and X' (right). There were some missing wires due to the dead channels of the readout electronics.

2.4 Forward spectrometer

Scattered K^- mesons produced in the $\pi^- p \rightarrow K^- X$ reaction were detected by the forward spectrometer. Figure 2.7 shows the kinematical relation between momentum and scattering angle of outgoing K^-'s within the acceptance of the forward spectrometer obtained from a simulation. There is a correlation between the scattering angle and the momentum in the $\pi^- p \rightarrow K^- \Theta^+$ relation since it is two body reaction, as shown by red points in Figure 2.7. The momentum from the Θ^+ production ranges around 0.85 GeV/c. On the other hand, the momentum of K^- from the background reaction ranges from 0.4 GeV/c to 1.1 GeV/c without any correlation. In this section, the detector system to identify K^- mesons with momentum from 0.4 GeV/c to 1.1 GeV/c and analyze momenta are described in detail.

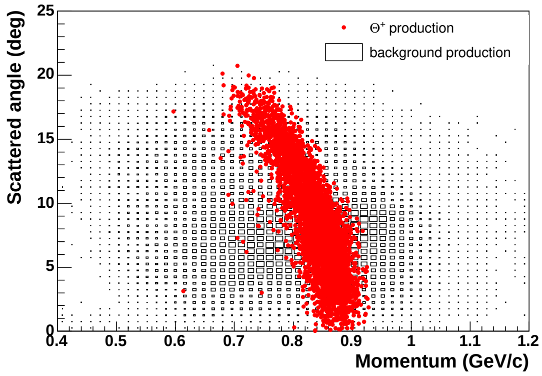

Figure 2.7: Kinematical relation between the scattering angle and the momentum in the $\pi^- p \rightarrow K^- X$ reaction within the spectrometer acceptance. The red points represent it for the Θ^+ production. The black boxes represent it from the background reactions including ϕ production, $\Lambda(1520)$ production and phase space.

2.4.1 Spectrometer magnet

The spectrometer magnet (KURAMA) is a window-frame conventional dipole magnet. The aperture of the magnet was 100(W) × 50(H) cm^2 and the iron yokes were 80 cm long. The KURAMA magnet was sandwiched by two end-guard plates of 10 cm (T) iron. The downstream end-guard had a 60-cm gap and 110-cm aperture, while the front end-guard had a 30-cm gap and 50-cm aperture. The front one was smaller than the other in order to minimize the fringing field at the target point, because the magnetic field distorted images of tracks in the electrostatic-type IIT. The total length was 164cm including the two end-guard plates at the entrance and the exit. The magnet center was located 15 cm horizontally from the beam axis in order to obtain a large acceptance for particles with one charge, i.e. positive charged particles in the (K^-, K^+) data and negative charged particles in the (π^-, K^-) data.

The spectrometer system was optimized so that the acceptance became maximum for the scattered K^+ with mean momentum of 1.1 GeV/c in the (K^-, K^+) reaction. Therefore the acceptance for K^- mesons in the (π^-, K^-) reaction decreases to about 80% with the same operation of the spectrometer magnet at (K^-, K^+) reaction, because the mean momentum of K^- was 0.8 GeV/c. In this experiment, however, the one more point to be considered was the missing mass resolution, because the Θ^+ is considered to be narrow and better missing mass resolution improves our experimental sensitivity. Therefore we operated the same magnetic field of about 0.93 Tesla to obtain better missing mass resolution. The acceptance was 0.14 sr for K^- with momentum of 0.8 GeV/c.

The magnetic field was calculated by interpolating from a field map which was measured at past experiment (E224) [68]. The magnetic field is shown in Figure 2.8 with the position of detectors.

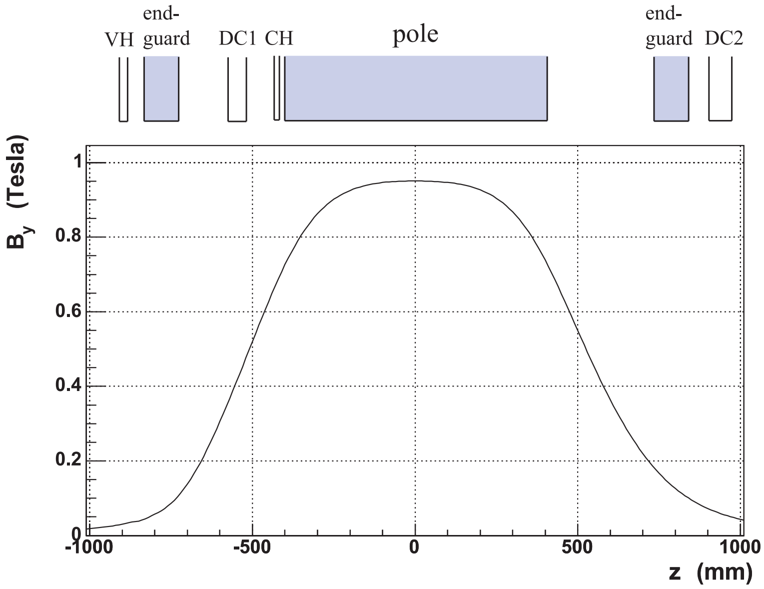

Figure 2.8: The magnetic field of KURAMA. Field strength of Y-direction (vertical) along the beam direction (Z) at X=0, Y=0 (magnet center in horizontal and vertical). The position of detectors are illustrated above the histogram.

2.4.2 Čerenkov counters

Two kinds of aerogel Čerenkov counters (BVAC, FAC) were used to reject the unwanted scattered particles at the trigger level. As shown in Figure 2.1 (b), BVAC was located in the center of the front end-guard and had relatively small size. The BVAC covered only beam spot because in the (K^-, K^+) reactions BVAC was mainly used to reject K^- beams which did not interact at the target. On the other hand FAC was located just downstream of the front end-guard and had the same size with the hole of the end-guard to eliminate the scattered π particles. In (π^-, K^-) reaction, both Čerenkov counters were used to reject π^-.

The BVAC consisted of a silica-aerogel block, with the size of 60 mm (wide) × 40 mm (high) × 20 mm (thick). The schematic view of BVAC is shown in Figure 2.9. The Čerenkov lights were collected from top and bottom with PMTs (HAMAMATSU R6608ASSY), which were fine-mesh type for operation in strong magnetic field, and had UV-transparent input windows. The refractive index was 1.05, which corresponded to the threshold velocity of $\beta = 0.952$ for Čerenkov radiation. Therefore, in the (K^-, K^+) data, the non-interacting K^+ beam of 1.66 GeV/c ($\beta = 0.959$) were rejected by BVAC, while the scattered K^+ with momentum less than 1.4 GeV/c ($\beta < 0.943$) could be alive. In the (π^-, K^-) data, the momentum range of K^- was 0.4∼1.1 GeV/c. The BVAC was used to discriminate the π particles.

The FAC consisted of a silica-aerogel block, with the size of 300 mm (wide) × 210

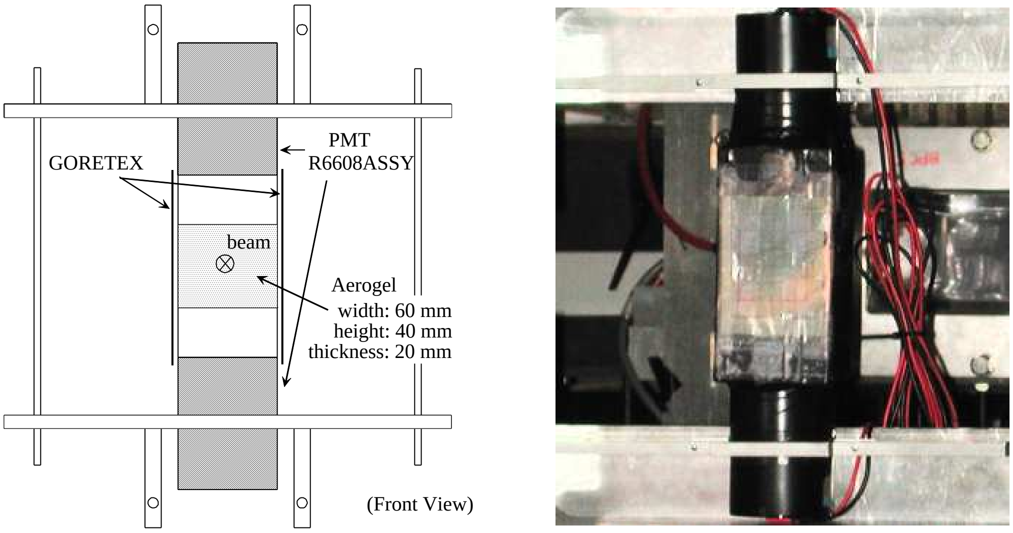

Figure 2.9: Schematic drawing and photograph of BVAC

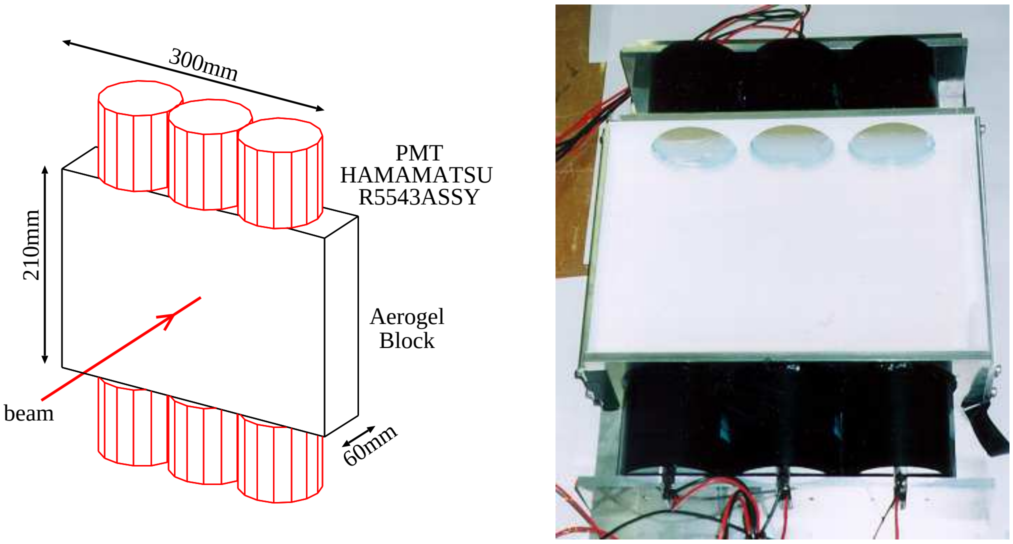

Figure 2.10: Schematic drawing and photograph of FAC

mm (high) × 60 mm (thick). The schematic view of FAC is shown in Figure 2.10. It was viewed by six fine-mesh-type PMTs, HAMAMATSU R5543ASSY, from top and bottom ends. The refractive index was 1.041 and the corresponding Čerenkov β-threshold was 0.962.

The efficiencies of the Čerenkov counters were measured at five β points using π^- and K^- beams of 1.67 and 1.4 GeV/c and π^- beam of 230 MeV/c. The typical ADC spectra are shown in Figure 2.11 where the open histograms were data for 1.67 GeV/c π^- and the hatched histograms were data for 1.4 GeV/c K^-. The threshold of the discriminator was shown by arrows. Figure 2.12 shows the efficiencies of BVAC and FAC as a function of β. The efficiency of FAC for π's with $\beta > 0.99$ was slightly low value of 95.4%, while the BVAC had sufficient efficiency more than 99.9%. The π particles which passed through the FAC veto were eliminated with the charge trigger and the mass trigger (see section 2.6). The over-killing rates of the K^-'s with momenta less than 1 GeV/c were 6.9±1.0%

	VH		CH	YH	FTOF
array direction	x	y	x	y	x
# of channels	32	18	24	6	24
thickness [mm]	2	2	2	5	30
width [mm]	6.6	9.0	19	200	80
spacing [mm]	4.4	6.0	17.5	180	75
PMT type	R5600U	R3164-10	H3165-01	H1161	H1949
scintillator type	SCSN-50	SCSN-50	SCSN-50	SCSN-56	SCSN-56
effective area [mm(x)×mm(y)]	143×110		421.5×300	1700×1100	1805×1200

Table 2.3: Specifications of the plastic scintillator hodoscopes. All PMTs are HAMAMATSU and all scintillators are KURARAY.

and 4.7±0.8% for BVAC and FAC, respectively.

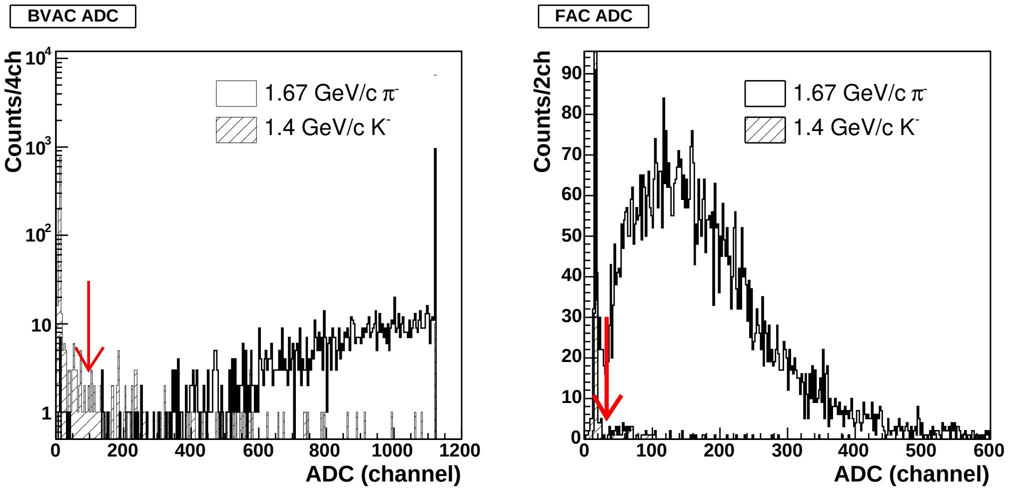

Figure 2.11: The typical ADC spectra of BVAC (left) and FAC (right). These spectra were linear sums of signals of all PMTs connected to each Čerenkov counters. The open histograms were data for 1.67 GeV/c π^- and the hatched histograms were data for 1.4 GeV/c K^-. The arrows represent the threshold positions of the discriminators.

2.4.3 Trigger hodoscopes

Four kinds of scintillator hodoscopes (VH, CH, YH and FTOF) were used in the forward spectrometer. The VH and CH were used as not only online trigger counters but also tracking detectors. The YH defined the acceptance of the spectrometer and were used as online trigger counter. The FTOF was used as not only online trigger counters but also time-of-flight counter. The specifications of these hodoscopes are summarized in Table 2.3.

Vertex hodoscope

The Vertex Hodoscope (VH) was located just downstream of the target. The schematic view of VH is shown in Figure 2.13. The VH consisted of 32 and 18 segments of scintillator

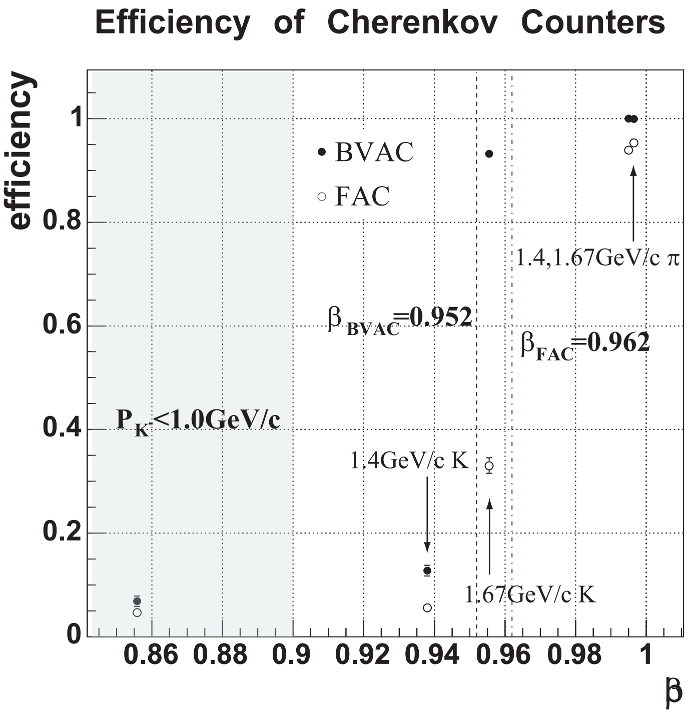

Figure 2.12: The efficiencies of BVAC (black circle) and FAC (open circle) as a function of β. The dashed line at $\beta = 0.952$ and the dot-dashed line at $\beta = 0.962$ are corresponding to the thresholds for Čerenkov radiation of BVAC and FAC, respectively. For the π^- beams with β more than 0.99, which was main background for (π^-, K^-) reaction, efficiency of FAC was a little low (95.4%), while efficiency of BVAC was more than 99.9%. The over-killing rates for the K^-'s of which momenta were less than 1.0 GeV/c were 6.9±1.0% and 4.7±0.8% for BVAC and FAC, respectively.

for horizontal (X) and vertical (Y) directions, respectively. The size of each X segment was 6.6 mm (wide) × 110 mm (high) × 2 mm (thick) and each segment was staggered with overlapping of 2.2 mm each other. The size of each Y segment was 9 mm (wide) × 143 mm (high) × 2 mm (thick) and each segment was staggered with overlapping of 3 mm each other. The scintillation lights were collected by one PMT connected to vertical end for X segments and horizontal end for Y segments. This VH was used as a tracking detector with position resolution of $2.2/\sqrt{12}$ mm and $3.0/\sqrt{12}$ mm for X and Y segments, respectively. The VH was also used as trigger counter to reject neutral particle events such as K^0 production where the neutral particle decayed after VH and the decay products made triggered event.

Charge hodoscope

The Charge Hodoscope (CH) was installed just upstream of the pole pieces of KURAMA as shown in Figure 2.14, in order to select the charge of each scattered particle together with hit information of FTOF. The CH was used for the first-level trigger as well as the second-level trigger. The CH consisted of 24 scintillators each of which was 19 mm wide, 300 mm height and 2.0 mm thick. The signals were read by one PMT connected via long light guide.

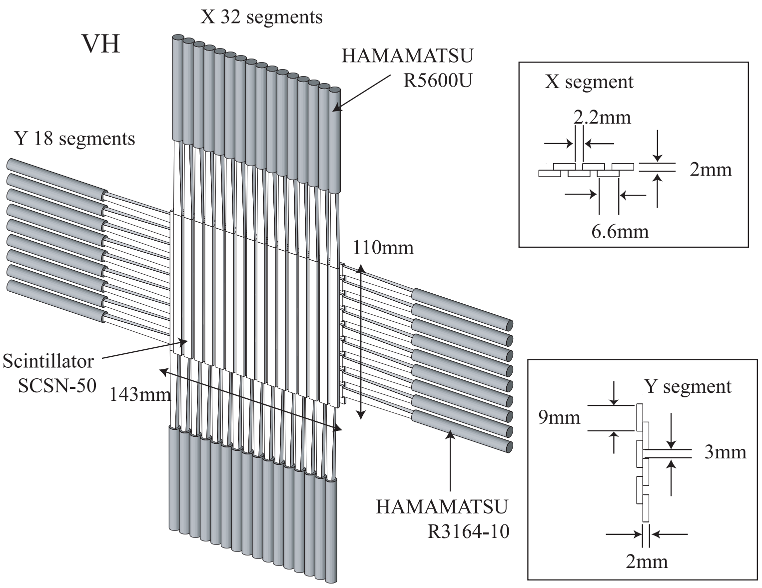

Figure 2.13: Schematic view of VH.

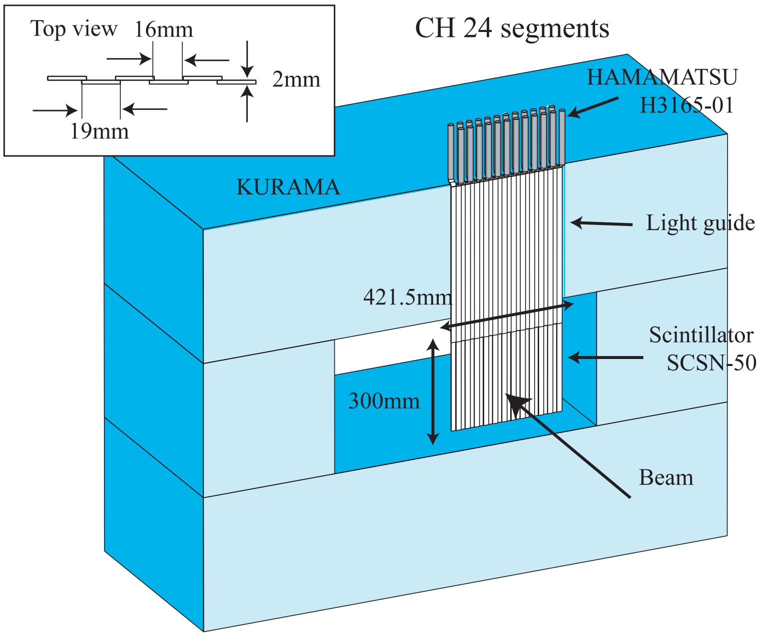

Figure 2.14: Schematic view of CH and the KURAMA magnet.

Y hodoscope

The geometrical acceptance of vertical direction was defined by the Y hodoscope (YH) which was located in front of FTOF. The YH consisted of 6 segments of scintillation counter with the size of 1700 mm (wide) × 200 mm (high) × 5 mm (thick) as shown in Figure 2.15. The signals of the scintillators were read from both horizontal ends connected to PMTs via lucite light-guides. These segments were also staggered with overlapping of 10 mm each other. In order to minimize the reaction events at YH, thin scintillators with 5 mm thickness were used.

Forward TOF

Time-of-flight information of each scattered particle was measured by TOF wall (FTOF) located in the most downstream of the forward spectrometer. The schematic view of FTOF is shown in Figure 2.15. The FTOF consisted of 24 segments of scintillation counter with the size of 80 mm (wide) × 1200 mm (high) × 30 mm (thick). Each segment was made of the plastic scintillators (SCSN-56) and its scintillation lights were collected by two PMTs (HAMAMATSU 1949) via lucite light guide. These segments were staggered with overlapping of 5 mm each other. The FTOF was located at the distance of 3333 mm from the target position and rotated from the beam direction by 10 degree to maximize the spectrometer acceptance. The resolution of time-of-flight from T2 to FTOF was obtained to be 132 ps as the mean value of all segments. The FTOF was also employed to measure vertical hit positions of particles on FTOF, which were given by the time difference of the two signals from the PMT's on the top and bottom.

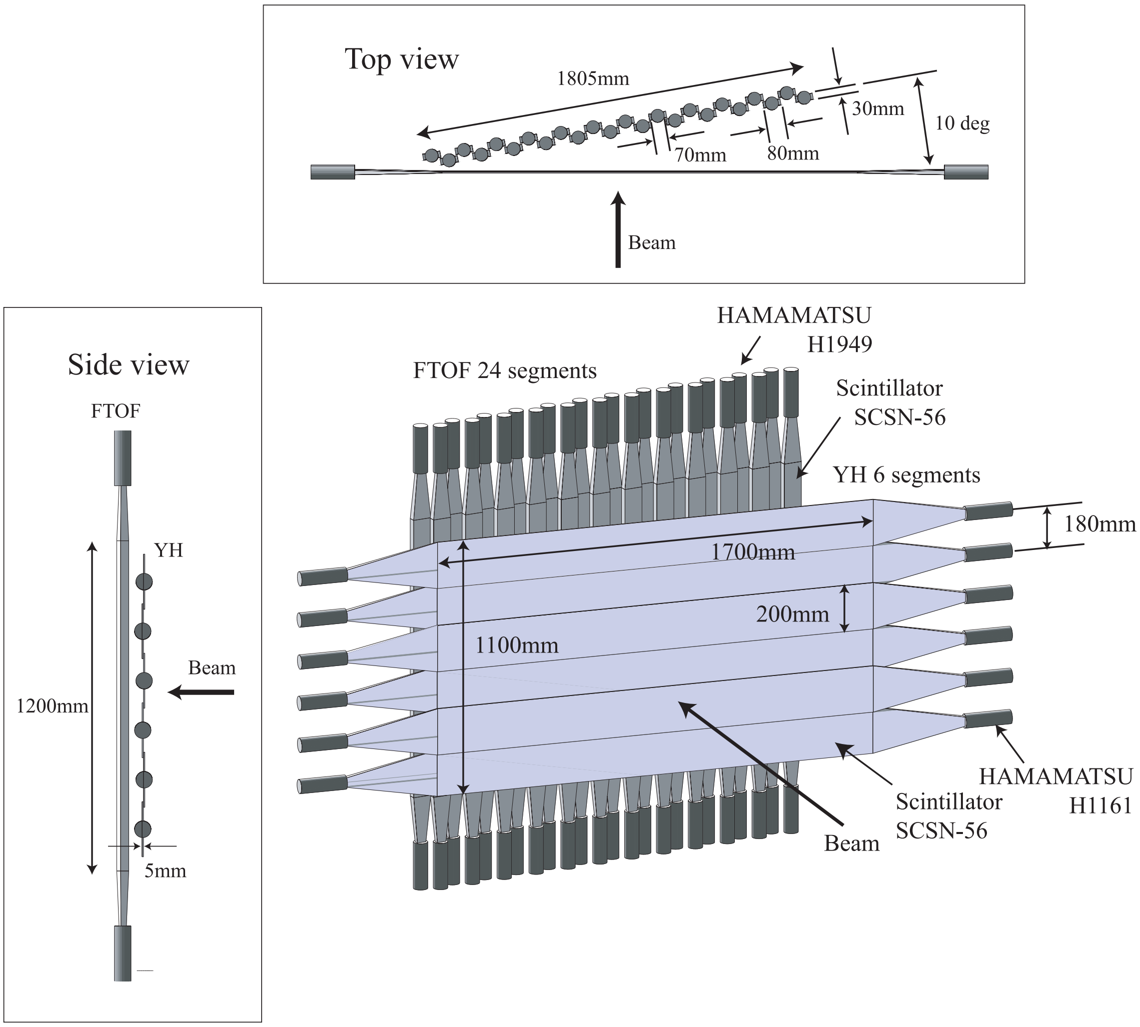

Figure 2.15: Schematic view of YH and FTOF.

	DC1	DC2	DC3
plane # of read wire	X X' Y U XX':48 / Y:32 / U:40	X X' Y Y' XX':128 / YY':96	X X' Y Y' XX':32 / YY':16
anode wire			
spacing (mm)	10.0	9.0	X: 56.0/ Y: 60.0
diameter (μm)	20.0	20.0	20.0
HV (V)	-	-	1000.0
material	Au-plated W	Au-plated W	Au-plated W
potential wire			
diameter (μm)	75	200	150
HV(V)	-1850	-1900	-3000
material	Au-plated Cu-Be	Al	Au-plated Cu-Be
position resolution (μm rms)	XX':200 / Y:200 / U:400	XX':210 / YY' 200	XX':230 / YY':240
efficiency (%)	X : 99.6 X' : 99.6 Y : 98.6 U : 98.1	X : 94.1 X' : 99.7 Y : 97.5 Y' : 99.4	X : 99.0 X' : 99.9 Y : 99.9 Y' : 99.6
effective area [mm(x)×mm(y)]	500×350	1200×1200	1800×900
gas mixture	Ar 50%, C_2H_6 50%		

Table 2.4: Characteristics and performance of Drift Chambers.

2.4.4 Drift chambers

The trajectories of scattered particles were reconstructed using drift chambers (DC1, DC2 and DC3) together with VH and CH. The characteristics of the drift chambers are summarized in 2.4.

The effective area of DC1 was 500 mm in width and 350 mm in height. The DC1 was installed between the front end-guard and pole pieces of KURAMA. There were four planes to measure the X, X', Y and U coordinates. The X and X' planes were staggered by the drift space of 5 mm. In the U plane, the sense wires were tilted by 15 degrees from the vertical direction. The cell structure of DC1 is shown in Figure 2.16 (a). The cathode plane were made of 15-μm-thick Kapton foils with aluminum coating on both sides.

The DC2 had an effective area of 1200 × 1200 mm^2 with 4 planes of X, X', Y and Y'. The DC2 was located at the end point of downstream end-guard and covered the full aperture of the magnet. The sense wires were surrounded by hexagonally located potential wires as shown in Figure 2.16 (b).

The DC3 had a sensitive area of 1800 mm in horizontal direction and 900 mm in vertical direction. The DC3 was located 530 mm downstream of DC2. The chamber had 4 planes of X, X', Y and Y' and the cell structure are shown in Figure 2.16 (c) for X, X' and (d) for Y, Y'.

The mixed gas of Ar-ethane (1:1) was used for all drift chambers.

The typical efficiencies of each chamber plane are also summarized in Table 2.4. To estimate this efficiency, at first, the trajectory of particle which did not decay was selected by connecting the tracks upstream and downstream of KURAMA by Runge-Kutta method. Then we checked the hit information of each plane corresponding to the track. The efficiencies of DC2X and DC2Y is a little low due to dead channels of readout electronics.

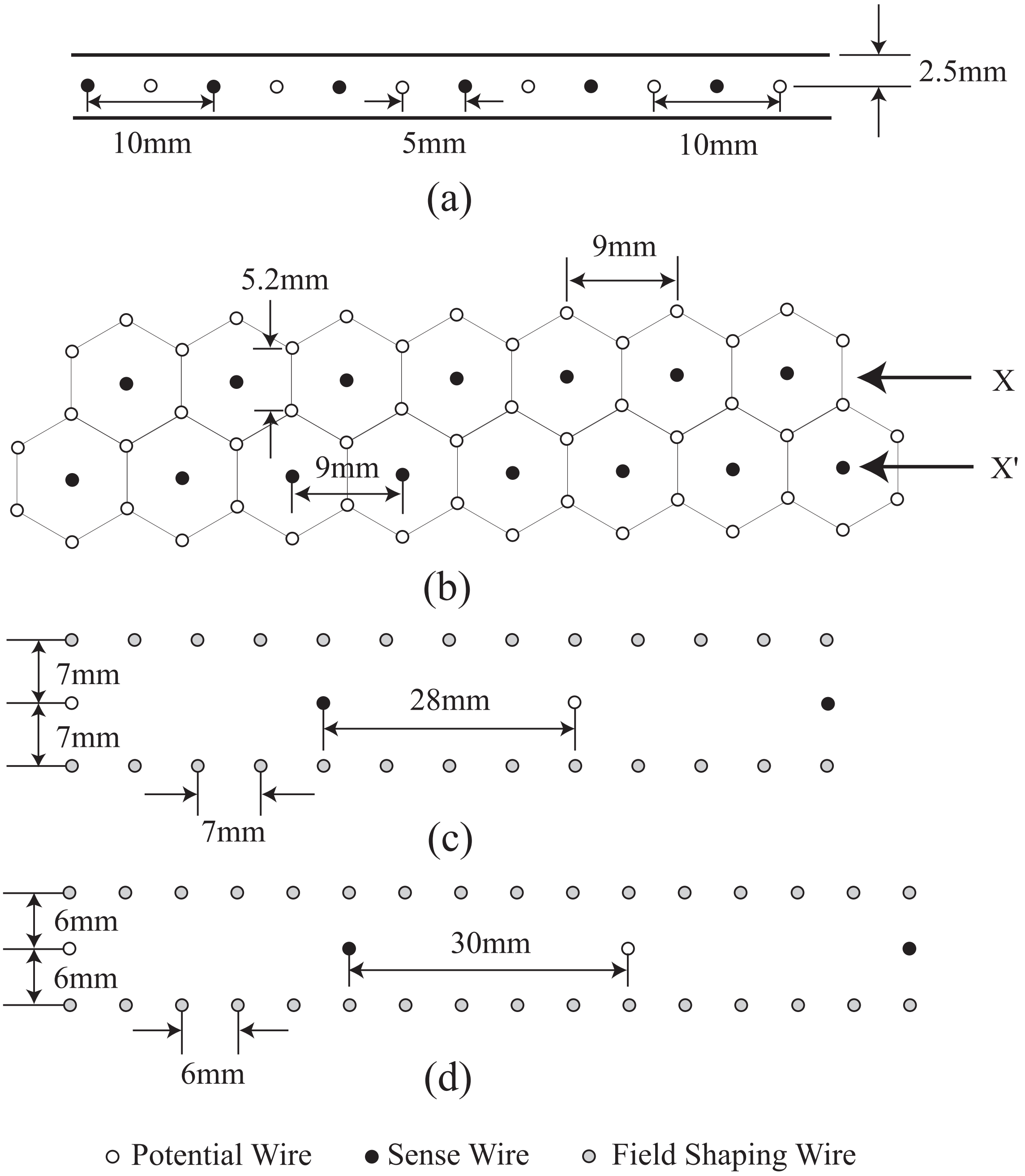

Figure 2.16: Cell structure of (a) DC1, (b) DC2, (c) DC3-X X' planes and (d) DC3-Y Y' planes.

2.5 Target

We used two kinds of targets.The first one was the Scintillating Fiber (SCIFI) target ($(\mathrm{CH})_n$) which was mainly used as an active target to measure the tracks of charged particles at a reaction point in the (K^-, K^+) reaction. The other one was a bulk target of polyethylene ($(\mathrm{CH}_2)_n$) to enhance the contribution from free protons. In the (π^-, K^-) reaction, the polyethylene target was mainly used.

2.5.1 Polyethylene target

The polyethylene ($(\mathrm{CH}_2)_n$) target with thickness of 10 cm and cross section of 10 × 10 cm^2 was used. The density was 1.0 $\mathrm{g/cm}^3$.

2.5.2 Scintillating fiber active target

The scintillating fiber (SCIFI) target was 20 cm long and was the same one used in the hyperon-nucleon scattering experiment (KEK-PS E289). It worked as a 4π tracking detector to measure tracks of charged particles produced in the (K^-, K^+) and (π^-, K^-) reactions. By reading out from two directions, we can reconstruct the event topologies three-dimensionally. Figure 2.17 shows a schematic view of the SCIFI active target system. The SCIFI active target system consisted of a SCIFI block, four image intensifier tubes to amplify the photon image, and CCD to read out and digitize the image data. Event topology around the reaction vertex was obtained with this system as image data of u-z and v-z projections. The SCIFI target had a large effective volume ($10 \times 10 \times 20$ cm^3) and consisted of thinner scintillating fibers (300×300 $\mu\mathrm{m}^2$ square cross section). The material of the fiber was polystyrene ($(\mathrm{CH})_n$) and the density was 1.03 $\mathrm{g/cm}^3$. The detail description of each parts is given in Appendix A.

The typical image of $^{12}\mathrm{C}(K^-, K^+\Lambda\Lambda)$ and $\pi^- p \to K^- K^0 p$ reactions are shown in Figure 2.18 and 2.19, respectively.

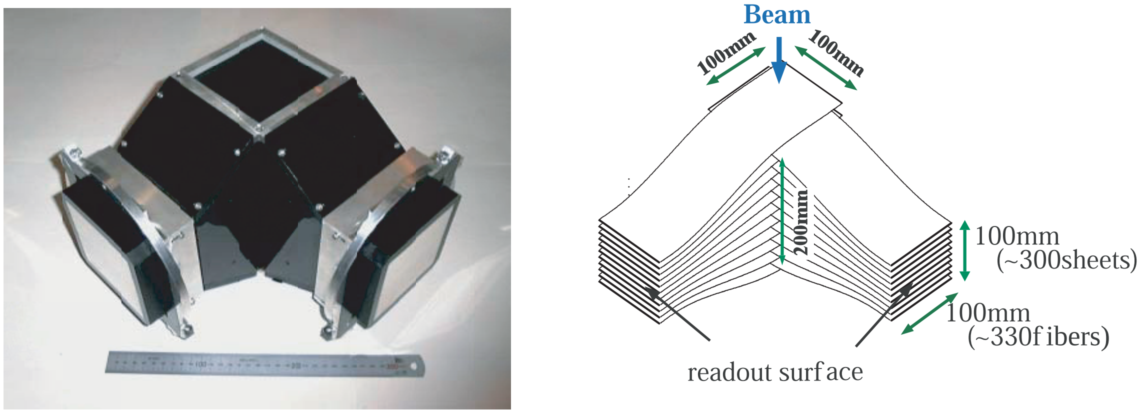

(a) Photograph of SCIFI target

(b) SCIFI block

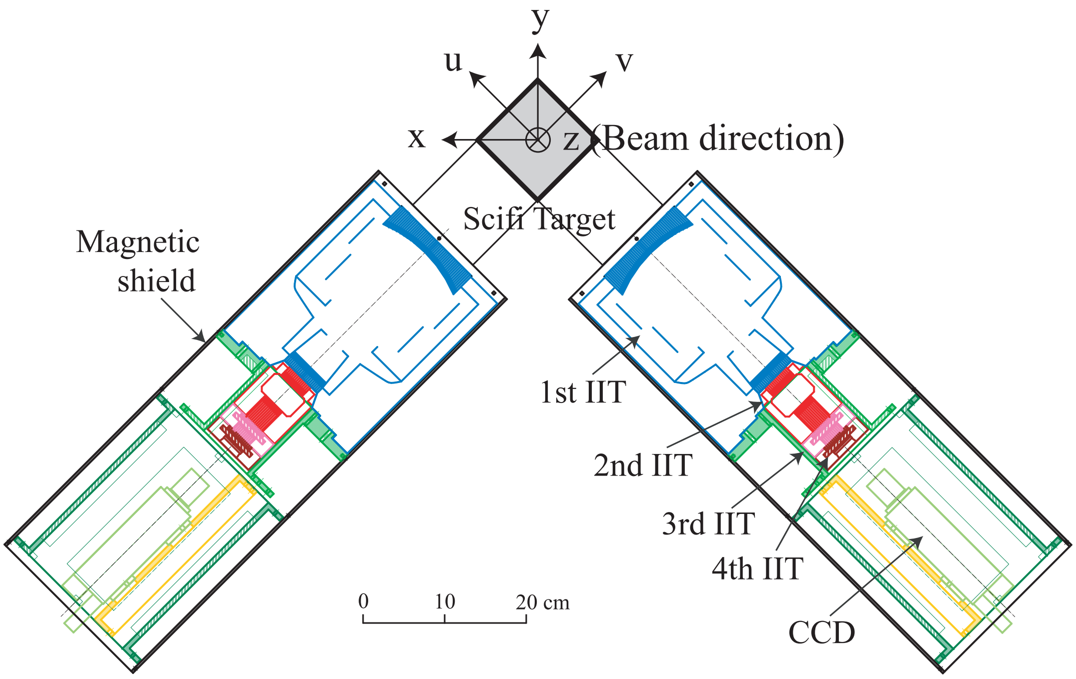

(c) SCIFI Active Target system

Figure 2.17: Schematic view of the SCIFI active target system. (a) photograph of the SCIFI target. (b) schematic view of the structure of the SCIFI block. The SCIFI block was assembled by stacking the fiber sheets, each of them contained about 330 fibers. The fiber sheets of each direction were bundled at the readout arms to make readout surfaces of 100 mm × 100mm. (c) schematic view of the total target system including readout devices. The target system was located in the direction of u and v which are rotated ±45 degree from the y axis. The shaded region is the effective volume of 100 mm × 100 mm. The readout system consisted of four IITs and a CCD camera. The first and second stages were electrostatic-type image intensifiers. The third and fourth one were micro-channel plate (MCP) type and were gatable. The CCD camera was also gatable type.

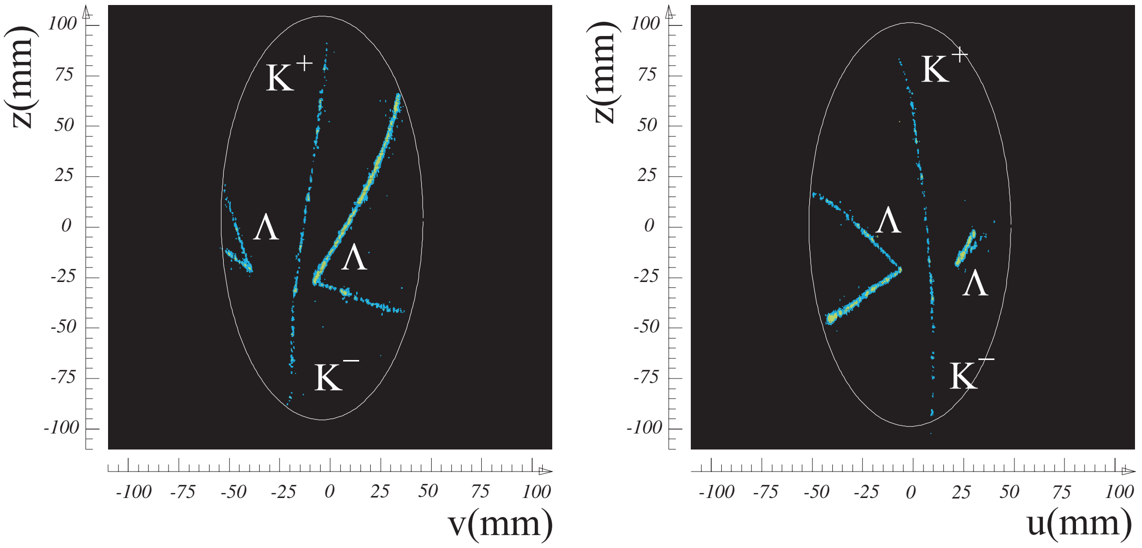

Figure 2.18: A typical image of ^{12}C$(K^-, K^+\Lambda\Lambda)$ reaction. The two image data are corresponding to the v-z and u-z projections taken from each side of the SCIFI target. The size of the fiducial areas are shown by the ellipses. Double Λ's were produced at the (K^-, K^+) reaction vertex. The Λ decaying into π^- and proton is shown as a clear V-topology.

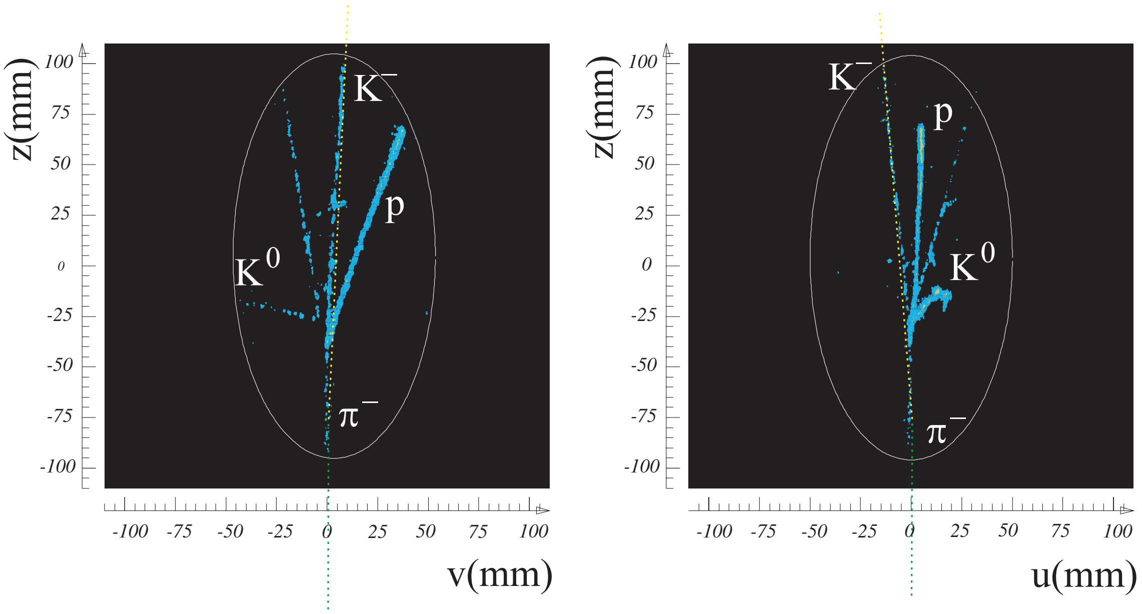

Figure 2.19: A typical image of $\pi^- p \rightarrow K^- K^0 p$ reaction. The green and yellow dotted lines were reconstructed tracks of π^- and K^- using the position detectors (wire chambers, hodoscopes). The K^0_S decaying into π^+ and π^- is shown as a clear V-topology. The proton stopped in the SCIFI target.

2.6 Trigger

The experimental setup was optimized for the (K^-, K^+) reaction. The trigger system was also designed to have a sufficient performance for the selection of the true (K^-, K^+) events from many background events. In the (π^-, K^-) reaction, the trigger was made with some modifications of the (K^-, K^+) trigger. Therefore, an explanation of the (K^-, K^+) trigger is given before we describe the (π^-, K^-) trigger.

In the (K^-, K^+) reaction, the main analysis was focused on the image data taken by the SCIFI active target system. Because the SCIFI system needed a long data taking time of several milli seconds, the sufficient rejection power of unwanted events at the trigger level was indispensable. The K^- beams were selected using the Čerenkov counters (BAC1, 2). For the forward spectrometer part, we had to select K^+ particles from the large backgrounds of π^+ and proton. Scattered π^+ and non-interacted K^- beam were rejected by the Čerenkov counters (BVAC, FAC). The charge of each scattered particle was selected using the hit combination of each segments of CH and FTOF (Charge Trigger). At this stage, the main background event of the (K^-, K^+) reaction was the (K^-, p) event. To eliminate these (K^-, p) events, we used the Mass Trigger, which used digitized time-of-flight information of the hit FTOF segment, as the second level trigger. After the selection using this trigger system, the trigger rate was 30 events/spill for 23,000 K^- beams per spill. This trigger rate was acceptable for the operation of the SCIFI system.

In the (π^-, K^-) reaction, the scattered K^- particle was selected in the same way. While the main background for the scattered K^+ in the (K^-, K^+) reaction was proton event, an anti-proton could not be produced in the (π^-, K^-) and this enabled us to select the K^- particle more easily.

2.6.1 First-level trigger

The role of the first-level trigger was to select a π^- beam and an outgoing K^- particle using fast signals from scintillation hodoscopes and Čerenkov counters. The logic diagram of the first-level trigger is shown in Figure 2.20. The incident beam particles were tagged by the signals of T1 and T2. In order to select π^- beams, BAC1, 2 were used as a coincidence. The main background for scattered K^- particles was π^- which was eliminated by BVAC and FAC. However, some π^- beam-through events and elastic scattering events survived due to the inefficiency of FAC (4.6%). In order to eliminate these π^- events, we adjusted the accepted region of the Charge Trigger (CT) as described below. The Charge Trigger module was a programmable matrix coincidence module and selected the charge of the scattered particle by checking whether the hit combination of CH and FTOF was within the accepted region which is surrounded by the red line in Figure 2.21. The CT also selected momenta of scattered particles roughly. Momenta of π^- events were around 1.9 GeV/c and are corresponding to the hatched ellipse region in Figure 2.21. On the other hand, momenta of K^- ranged from 0.4 GeV/c to 1.1 GeV/c as shown by boxes (not filled) in Figure 2.21. Therefore we adjusted this region to accept almost all momentum range of K^- within the spectrometer acceptance and reject high momentum π^- particles. Finally, the "OR"ed signal of YH was required to cut off the neutral particles hitting FTOF.

Thus the first-level trigger was defined by

$$T1 \otimes T2 \otimes BAC \otimes \overline{BAVC} \otimes \overline{FAC} \otimes CT \otimes YH. \tag{2.1}$$

Gate signals of ADCs and common start/stop signals of TDCs for detectors of the spectrometer were made by the first-level trigger. For the operation of SCIFI target, the gate signals of the third and fourth IITs were also made by this signal. The rate of the first-level trigger was typically 320/spill for the beam intensity of 3.3×10^5 π^-/spill.

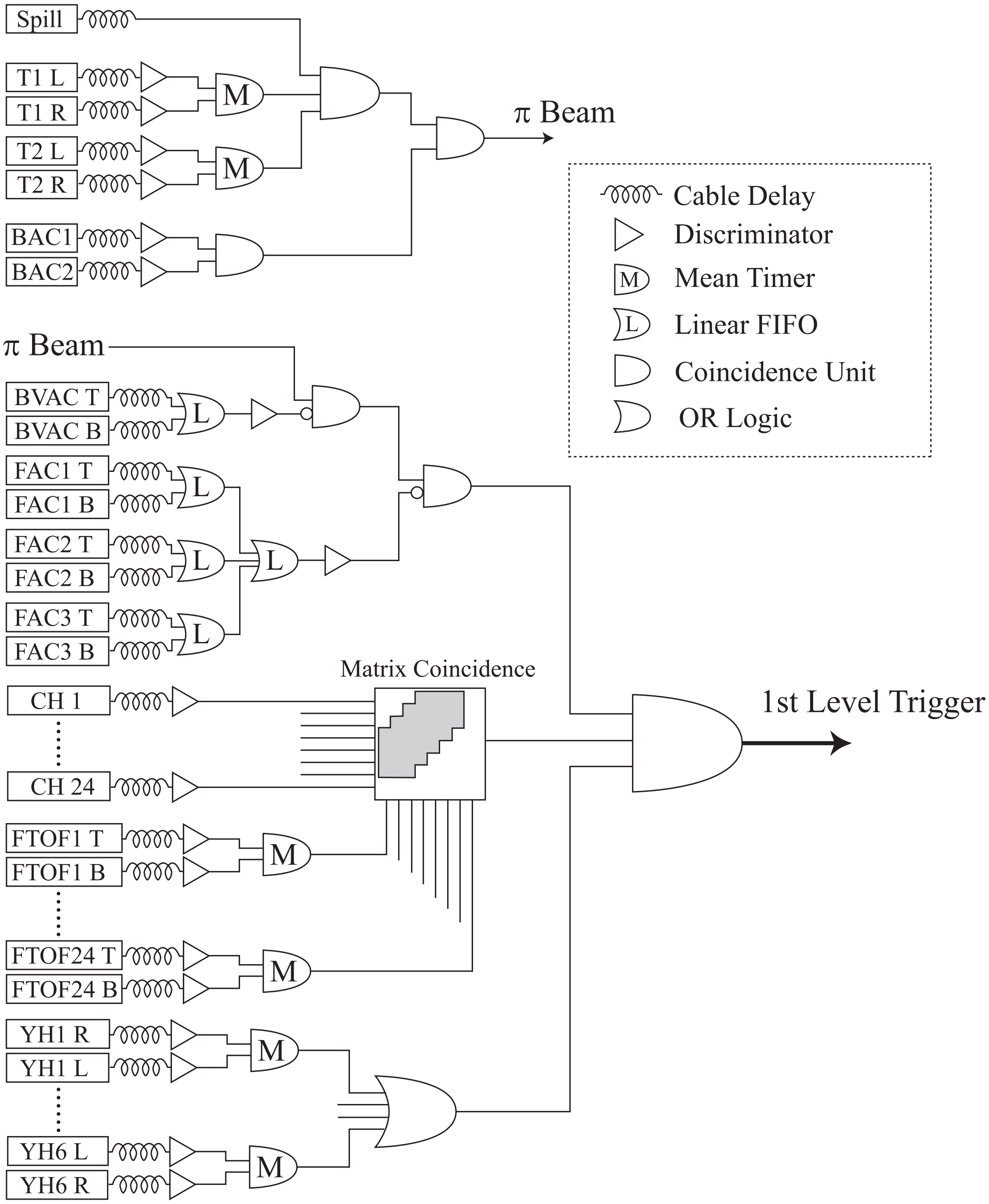

Figure 2.20: Logic diagram of the first-level trigger.

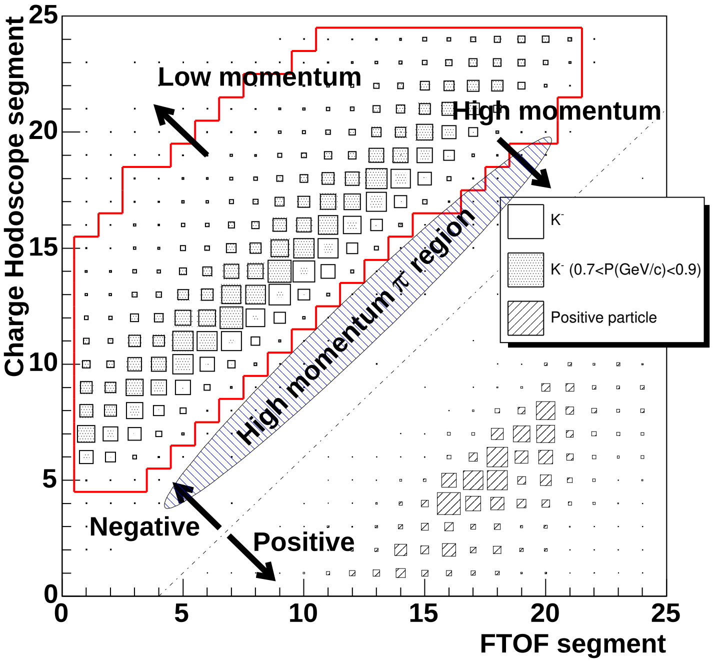

Figure 2.21: The combination of the hit CH and FTOF segments. The open, shaded and hatched histograms are the combinations for K^-'s, K^-'s with momentum of 0.7 GeV/c $< p <$ 0.9 GeV/c and positive particles, respectively. The particle identifications were done by offline analysis. The region surrounded by the red line was the accepted region of the CT. From the hit combination the momenta of the scattered particles are roughly selected; to the direction of the arrow titled "High momentum", momenta become larger and to the direction of the arrow titled "Low momentum", momenta become lower. The momenta of π^- beam-through events and elastic scattering events are corresponding to the hatched ellipse region.

2.6.2 Second-level trigger

The second-level trigger was defined by

$$1st\ level\ trigger \otimes (VHx \otimes VHy) \otimes MT. \tag{2.2}$$

We required the hit of VH to eliminate the background triggers caused by the neutral particles such as K^0_S mesons. The mass trigger (MT) was the main component of the second-level trigger and the detail explanation of MT are given bellow. This mainly rejected the π^- mesons accepted at the first-level trigger.

Mass trigger

As described at the explanation of CT, the momenta of outgoing particles were determined using the hit combination of CH and FTOF. For events with the same hit combination, the difference of their masses should appear as the difference of their time-of-flight. The typical time-of-flight spectra are shown in Figure 2.22 where the peaks corresponding to K^- and π^- are clearly seen. The particle identification can be done by setting a suitable window against time-of-flight for each combination of CH and FTOF.

The trigger scheme for the mass trigger is illustrated in Figure 2.24. The timing information of the CH and FTOF signals were digitized with LeCroy 4303 TFC (Time-to-Fera Converter) and LeCroy 4300B FERA (Fast Encoding and Read out Adc) modules (FERET). The hit addresses and the timing information of FTOF were stored in the memories in the FERA modules, and the hit information of CH was stored in a LeCroy 2375 Data Stack module. The hit addresses of CH and FTOF were send to a LeCroy 2372 MLU (Memory Lookup Unit) module and decoded into momentum information. Another MLU stored the trigger windows against the FTOF TDC data for corresponding combinations of CH and FTOF. It selected the particle masses by combining the FTOF timing data and the momentum information obtained by the first MLU.

The decision time of the mass trigger was about 14 μs. The trigger rate was 85 per spill for the π^- beam intensity of 3.3×10^5. The contamination due to the π^-'s were reduced to typically 42% with the mass trigger. The overkilling rate of K^- mesons was 4.3% (see Section 3.9.7)

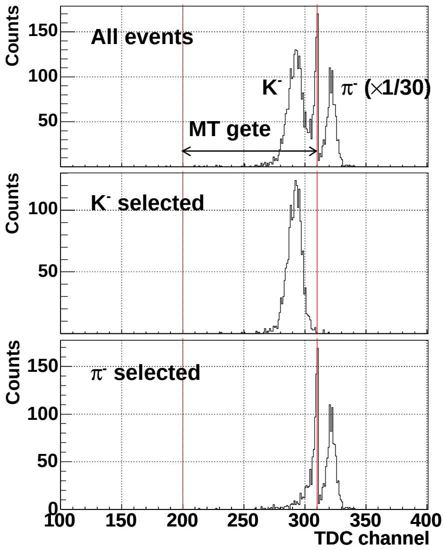

Figure 2.22: Time-of-flight spectra between T2 and FTOF against the events where there were hits at CH segment 13, 14 and FTOF segment 9. The top spectrum is for all particles. The peaks corresponding to K^-'s and π^-'s are clearly seen. The middle and bottom spectra are for K^-'s and π^- selected in the offline analysis. The red lines are the accepted window for the mass trigger. The data outside of this window were collected for the check of the efficiency of the mass trigger with the prescale factor of 30.

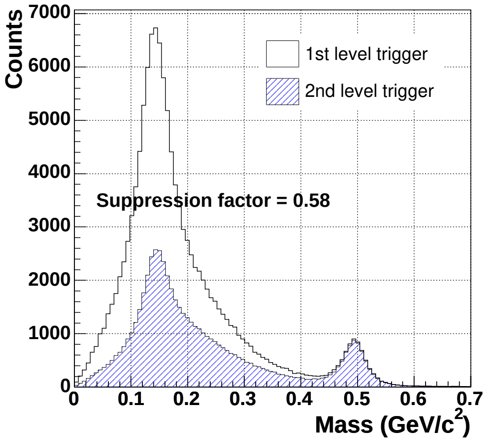

Figure 2.23: Mass distribution of outgoing particles with the first level trigger (open histogram) and the 2nd level trigger (hatched histogram). The π^- particles were reduced to typically 42%.

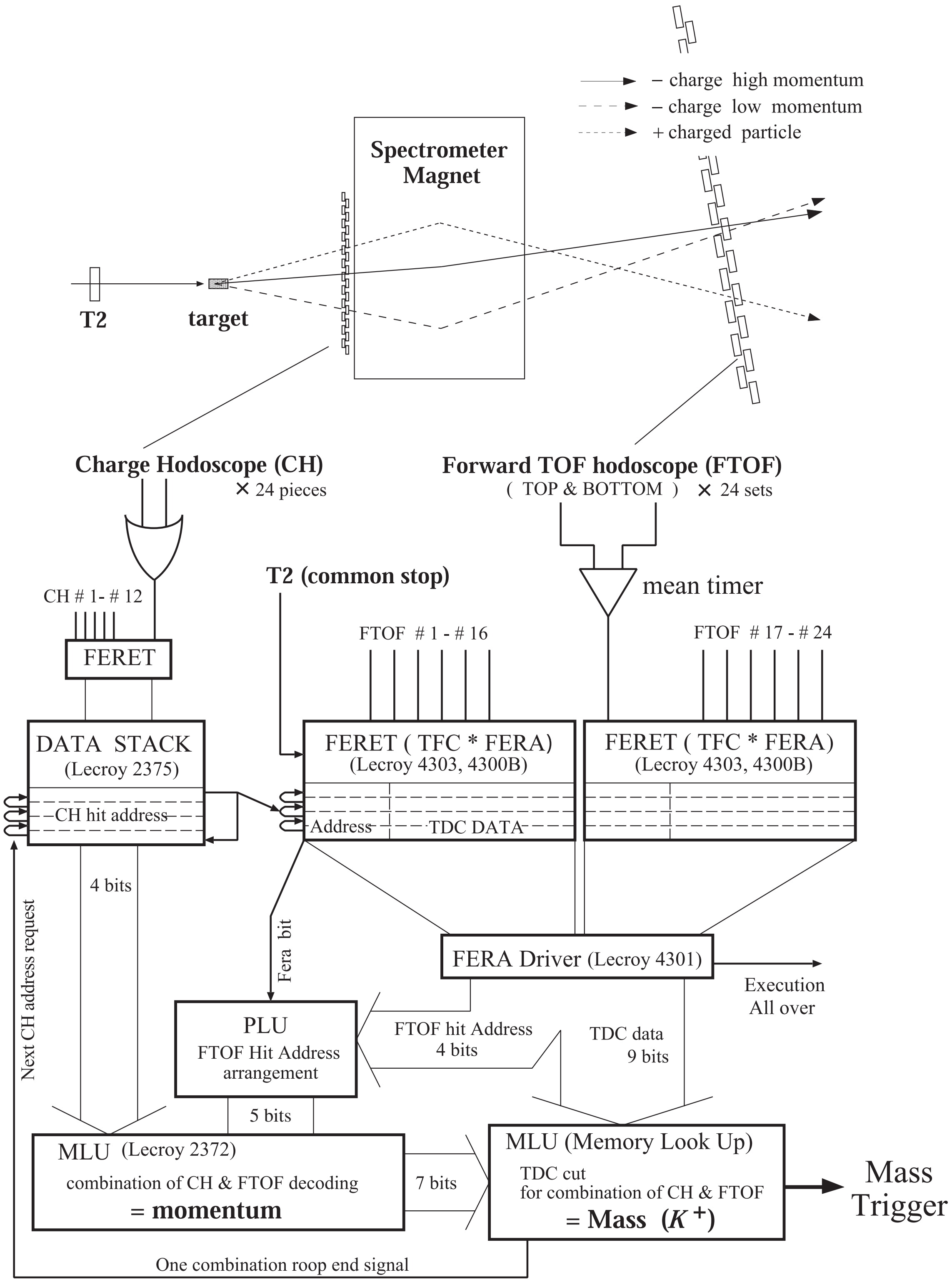

Figure 2.24: Logic scheme of the mass trigger.

2.7 Data acquisition and monitoring

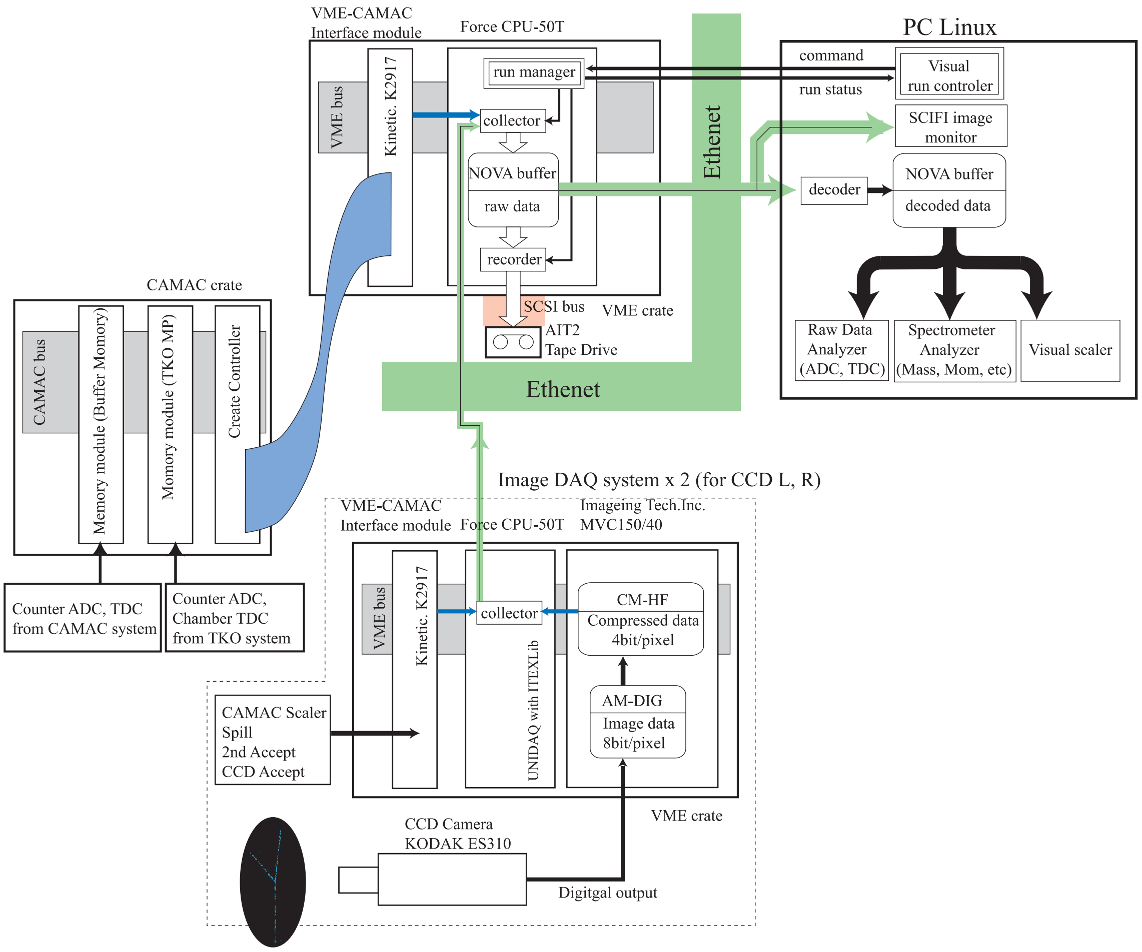

Figure 2.25: Schematic diagram of the data flow during the data acquisition and monitoring. See text for detail.

The data flow of the data acquisition is illustrated in Figure 2.25. The signals of counters and chambers of the spectrometer were digitized by ADCs and TDCs of CAMAC and TKO standard. The conversions of the signals were started at the timing of the first-level trigger. When the second-level trigger was accepted, the digitized data were send to CAMAC memory modules (Buffer Memory, TKO MP). When the second-level trigger was rejected, the data were cleared. Data were stored during one spill in the memory modules and were collected at the end of the spill by the DAQ system which is called ”Spectrometer DAQ” here to distinguish from ”Image DAQ” for SCIFI sub DAQ system. The Spectrometer DAQ was operated by a Unix operating system on a VME on-board computer (FORCE SPARC CPU-50T). The data of the spectrometer as well as scaler and some trigger flags were acquired by a ”collector” process from CAMAC memory modules via VME-CAMAC interface modules.

For the data acquisition of SCIFI image data, the independent sub DAQ systems called ”Image DAQ” were used for each CCD camera. The Image DAQ was also operated by a Unix operating system on a VME on-board computer (FORCE SPARC CPU-50T). The CCD camera we used was Kodac MEGAPLUS Camera ES310. The readout of the CCD data was triggered by the external signal made from the second-level trigger. The digital data were compressed from 8 bit to 4 bit using the real time image processing module (Imaging Technology Coop. MVC 150/40). At the end of the spill, the image data were transfered to the ”collector” process of the Spectrometer DAQ via Ethernet. The Image DAQ also collected scaler data such as ”spill”, ”number of 2nd accept”, ”number of CCD accept” for each event. These scaler information were used for the event matching between the spectrometer and CCDs.

The data during one spill of the spectrometer and CCDs (if we used the SCIFI target) were transfered to the ”collector” process of the Spectrometer DAQ. The collected data were managed by a NOVA buffer manager, and recorded in a AIT2 tape by a ”recorder” process. In order to monitor the data during the data acquisition, some on-line analyzers were executed on a personal computer operated by a Linux 2.0 operating system. A ”decoder” process took the raw data from the NOVA buffer of the Spectrometer DAQ and decoded for some on-line analyzers. The decoded data were managed by a linux-local NOVA buffer manager. The data of the spectrometer were monitored by two ”analyzer” program. One was ”raw data analyzer” which checked raw data such as ADC, TDC spectra and hit profiles of wire chambers. Another one was ”spectrometer analyzer” which calculated momenta and masses of scattered particles, and so on. The ”spectrometer analyzer” was much helpful to adjust the CT accept region at the online level. The CCD images were sent to an online monitoring software directory from the Spectrometer DAQ buffer manager and monitored by human eyes. The run control (start, stop, pause or resume) was carried out from the Linux PC via Ethernet.

2.8 Data summary

Table 2.5 shows the data summary. For the $\pi^- p \to K^- X$ reaction, we used π^- beams of 1.87 and 1.92 GeV/c. At 1.92 GeV/c, only the polyethylene target was used. In order to estimate the contribution from carbon in the SCIFI and polyethylene targets, carbon target data were taken. The (π^+, K^+) data were taken to measure Σ^+ for the calibration of the missing mass spectrum. The (K^-, K^+) data were also used for momentum correction and only the analyzed data size is listed in Table 2.5.

P_{beam} (GeV/c)	reaction	target	N_{Beam} ($\times 10^8$)	data taking time
1.87	(π^-, K^-)	SCIFI	29	20.5 hour
		polyethylene	30	14.5 hour
		^{12}C	8.4	2.5 hour
	(π^+, K^+)	polyethylene	1.4	2 hour
1.92	(π^-, K^-)	polyethylene	74	31.5 hour
		^{12}C	8.4	2.5 hour
	(π^+, K^+)	polyethylene	4.3	3.5 hour
1.67	(K^-, K^+)	SCIFI	14	$\sim$ 3 day

Table 2.5: Data summary, where P_{beam} is the beam momentum and N_{Beam} is the number of beam particles irradiated on each target.

Chapter 3

Analysis

3.1 Outline

The goal of our analysis is to obtain the missing mass spectrum of the $\pi^- p \to K^- X$ reaction and derive the production cross section of the Θ^+ with the π^- induced reaction. In this chapter, the analysis procedures are described. The contents consist of three parts as explained bellow.

In the first part, the analysis procedure to find good (π^-, K^-) events will be described with attention to the performance of the analysis and the cut points. The outline of the first part is following.

1. Selection of the incident π^- and determination of the momentum (Section 3.2).

The particle identification was done by the time-of-flight between T1 and T2. To calculate the momentum, the trajectory was reconstructed using the hit information of beam line chambers and a transfer matrix.

2. Determination of the momentum of the outgoing particle and selection of K^- (Section 3.3).

The trajectory of the outgoing particle was reconstructed using the information of tracking detectors and field map of KURAMA. The mass was obtained from the momentum information and time-of-flight between T2 and FTOF.

3. Determination of the reaction vertex (Section 3.4).

The reaction vertex was obtained as the closest distant point between the incident π^- and the outgoing K^-.

In the second part, momentum resolutions for incident and outgoing particles are studied by reconstructing the Σ^+ from the missing mass spectrum of the $\pi^+ p \to K^+ X$ reaction (Section 3.6). Then the expected missing mass resolution for the Θ^+ is shown (Section 3.7). Good performance of the analysis is also confirmed by using the (π^-, K^-) data (Section 3.8).

In the final part, for the preparation of deriving the cross section, various efficiencies such as decay factor of the outgoing K^- and the acceptance of the spectrometer are obtained (Section 3.9).

Monte Carlo simulation

In order to estimate not only these values such as decay factor and the acceptance of the spectrometer but also the missing mass resolution for the Θ^+, we have developed the Monte Carlo simulation program based on the GEANT4 [72]. All materials of the spectrometer are included in this program. It simulates trajectories of particles through the experimental apparatus taking into account decay in flight, energy loss, multiple scattering, and hadronic reaction of the particles. The realistic chamber performances such as resolutions and efficiencies are also taken into account. The output data produced by the simulation were analyzed by the same analysis code used for the real data.

3.2 Analysis of π^- beam

3.2.1 Identification of π^- mesons

The incident particles were identified with the information of time-of-flight between the T1 and T2 counters placed about 7.2 m apart. Figure 3.1 shows spectra of the time-of-flight. The typical time resolution after the ADC pulse height correction was 72 ps. We selected $\pm 3\sigma$ region of its time resolution as good events as shown by arrows in Figure 3.1. The bump around -750 ps might be considered to be K^- because it is consistent with the time difference between π^- and K^-. Therefore the contamination of K^- in the selected region was negligible. By this cut, 94.2% of the total events were accepted.

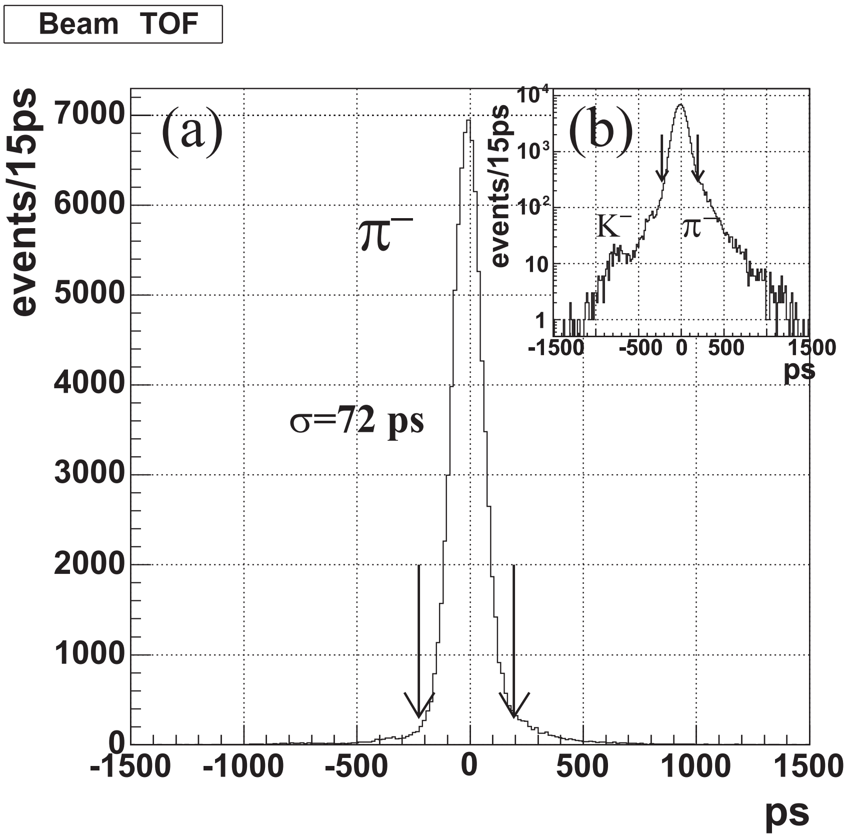

Figure 3.1: TOF spectra of incident particles (a) in a linear scale and (b) in a logarithmic scale . The arrows indicate the selection window for π^- mesons which is the $\pm 3\sigma$ region of its time resolution. The bump around -750 ps might be K^- mesons.

3.2.2 Momentum analysis of π^- mesons

The momenta of the incident particles were calculated by fitting the hit positions of the beam line chambers upstream and downstream of the D2 magnet (BDC1, 2, 3 and BPC1, 2) with the second order transfer matrix calculated by TRANSPORT [70]. The concept of beam optics and the detail procedure of momentum analysis are described here.

A beam line is comprised of a set of magnetic elements such as bending magnets or quadrupole magnets placed sequentially at intervals along an assumed reference trajectory.

The trajectory moving along the beam line can be described by the beam optics. At any specified position in the system, an arbitrary charged particle is represented by a vector X defined below.

$$X = \begin{pmatrix} x \\ \theta \\ y \\ \phi \\ \delta \end{pmatrix} \tag{3.1}$$

Definitions:

x = the horizontal displacement of the arbitrary ray with respect to the assumed central trajectory.
θ = the horizontal angle of the ray with respect to the assumed central trajectory.
y = the vertical displacement of the ray with respect to the assumed central trajectory.
ϕ = the vertical angle of the ray with respect to the assumed central trajectory.
δ = $\delta p/p$ is the fractional momentum deviation of the ray from the assumed central trajectory.

The optical element such as magnets can be represented by a matrix and the position of the charged particle after the optical elements is represented by the equation

$$X_i(l) = \sum_j R_{ij} X_j(0) + \sum_{jk} T_{ijk} X_j(0) X_k(0), \tag{3.2}$$

where $X(0)$ is the initial coordinate vector and $X(l)$ is the final coordinate vector of the particle, and R and T are the the first order and the second order transfer matrices respectively.

The first and second order transfer matrices were calculated using TRANSPORT, which is the program code developed for the design of static-magnetic beam transport system [70]. In this analysis, we used hit positions of BPC1, 2 and BDC1, 2, 3 and the matrix of the D2 magnet. In this case, the position vector was three components vector (x, θ, δ) and the first order transfer matrix was 3×3 matrix. The initial values of x and θ were given by the local tracks at the entrance of the D2 magnet obtained by fitting the hit positions at these chambers. The trajectory of beam was connected to BDC3 using the transfer matrix. The particle momentum was determined by minimizing the following χ^2 value. The χ^2 value is defined as

$$\chi^2 \equiv \frac{1}{n-3} \sum_{i=1}^{8} H_i \left(\frac{P_i - f_i(\overrightarrow{X}_{in})}{w_i} \right)^2 \tag{3.3}$$

$$n = \sum_{i=1}^{8} H_i \tag{3.4}$$

$$H_i = \begin{cases} 1 & \text{if } i\text{th plane has a hit} \\ 0 & \text{if } i\text{th plane has no hit} \end{cases} \tag{3.5}$$

where P_i and w_i denote the hit position and resolution of i-th plane. The calculated position by the transfer matrix at i-th plane is denoted by $f_i(\overrightarrow{X}_{in})$, where $\overrightarrow{X}_{in}$ is the initial coordinate vector at the entrance of D2 magnet. The particle momentum is denoted by $p = p_0(1+\delta)$, where p_0 is the central momentum.

The typical χ^2 distribution of 1.92 GeV/c π^- beam is shown in Figure 3.2. The χ^2 distributions with each degrees of freedom, that is (number of hit planes − 3), are also shown in Figure 3.2, where the smooth lines represent the expected reduced χ^2 distributions with the corresponding degrees of freedom. The obtained χ^2 distribution was consistent with the expectation except a tail towards large χ^2. We selected confidence level = 95% region for χ^2 cut when the number of hit planes was 5, 6 and 7. In case of hit number of 8, the χ^2 distribution was slightly broader. Therefore we selected confidence level = 99% region. The selected regions are shown by arrows in Figure 3.2 for each degrees of freedom. The efficiency of this cut was 84.6% as the result of rejecting the large χ^2 events. The obtained momentum distributions are shown in Figure 3.3. The events of which momenta were less than 1.8 GeV/c or larger than 2.0 GeV/c were rejected considering the momentum acceptance of the beam line.

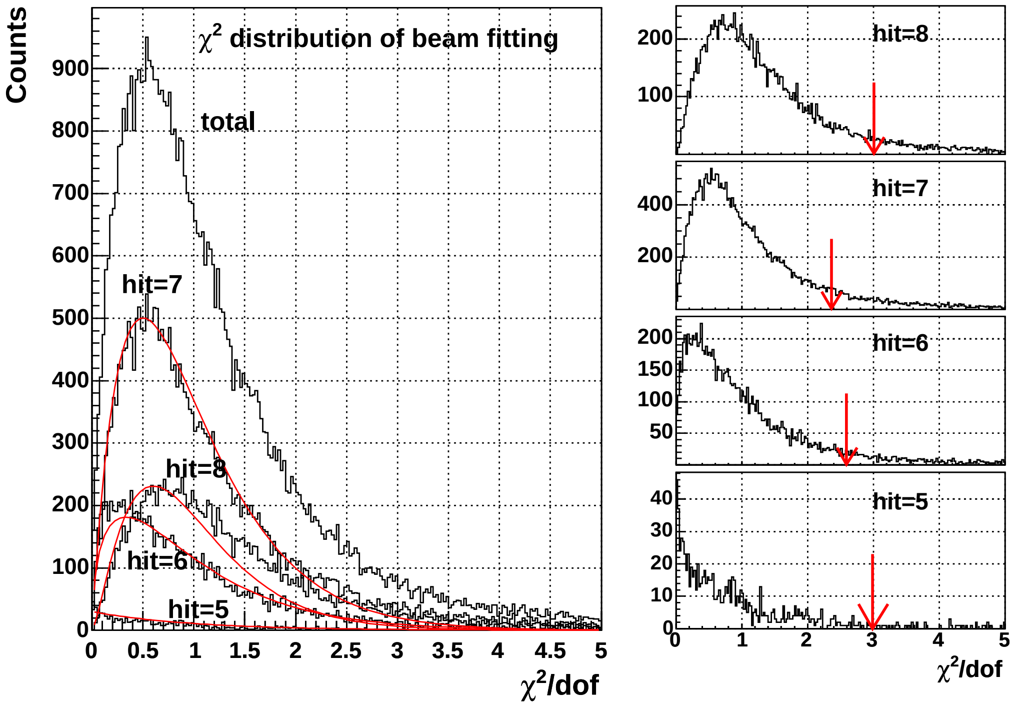

Figure 3.2: χ^2 distributions of the beam tracking using the transfer matrix. The smooth lines represent the expected reduced χ^2 distributions with the corresponding degrees of freedom. Right figures represent the χ^2 distributions for each degrees of freedom. The arrows show the cut positions which are corresponding to 95% confidence level for hit plane number of 5, 6 and 7 and 99% confidence level for hit plane number of 8.

The momentum resolution of this tracking method was estimated with a Monte Carlo simulation. Figure 3.4 shows the results of the same analysis using the hit information for each chamber produced in the simulation. The χ^2 and momentum distribution are shown in (a) and (b), respectively, and these are consistent with the real data. Figure 3.4 (c) is the plot of the differences between generated momenta and calculated momenta. From this plot, the momentum resolution was obtained to be σ=8.9 MeV/c. This resolution was taken into account in the Monte Carlo simulation to estimate the missing mass resolution of this spectrometer system.

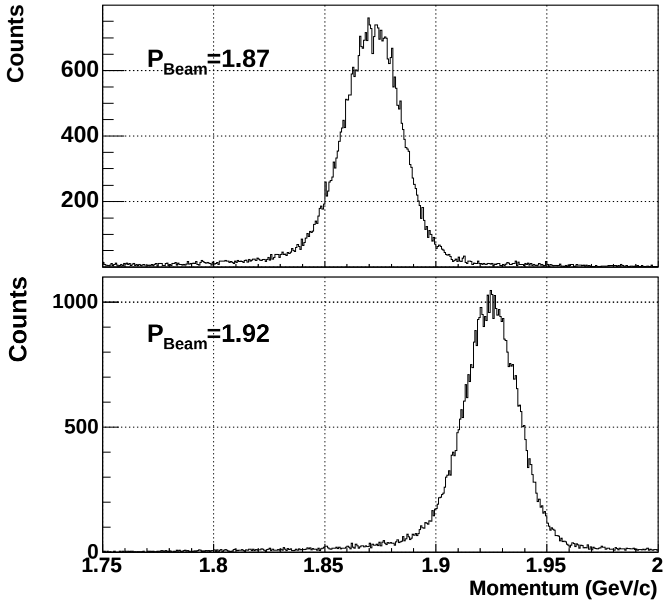

Figure 3.3: Obtained momentum distributions for the beam momenta of 1.87 GeV/c (top) and 1.92 GeV/c (bottom).

The beam direction at the target was measured by three proportional chambers (BPC3, 4, 5) located with the distance of 1 m for BPC3 – BPC4 and 2 m for BPC4 – BPC5. The angular resolutions were estimated to be 0.008 degree for both horizontal and vertical directions.

3.3 Analysis of outgoing particles

3.3.1 Measurement of momentum

The trajectories of outgoing particles were reconstructed using the position information of the drift chambers (DC1,2,3) and the hodoscopes (VH,CH) and the magnetic field strength calculated with the field map. First, straight tracks were defined locally at the entrance and exit of the KURAMA magnet by VH·DC1·CH and DC2·3 using a least-square method, respectively. To find tracks, all combinations of the left/right ambiguity were examined, because the trajectory had a large angle and we could not use the pair plane information. The trajectory with minimum χ^2 was selected as the reconstructed track. In multi track events, chamber hits corresponding to each track were required not to be duplicate for all planes.

From here, we call the local track at the entrance "up-track" and the local track at the exit "down-track". Then, we have to combine the up-track with the down-track. In

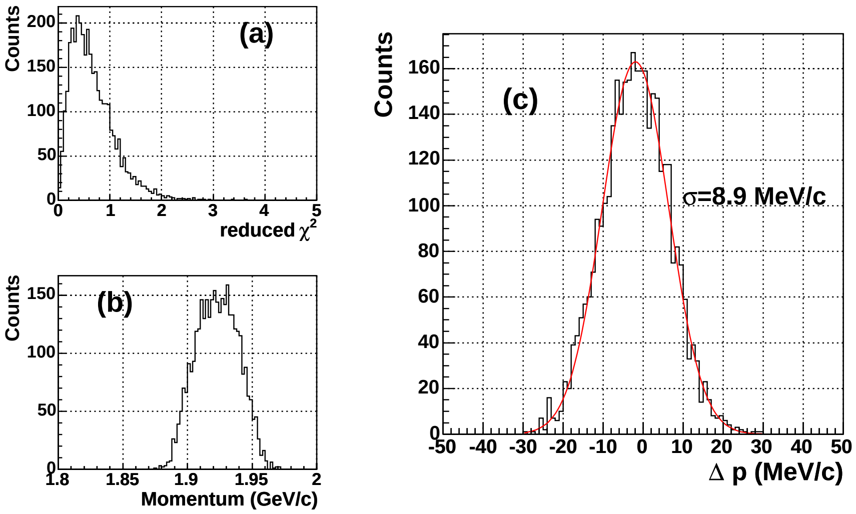

Figure 3.4: Results obtained from a Monte Carlo simulation. (a) χ^2 distribution. (b) momentum distribution. (c) the differences between generated momenta and calculated momenta. The momentum resolution was obtained to be σ=8.9 MeV/c.

order to find a good combination of these tracks, the following consistencies were checked. Finally, the trajectory was reconstructed using the Runge-Kutta tracking method [71].

Consistency between FTOF and down-track

The consistency between the down-track and the hit FTOF segment was checked to reject events where outgoing particles decayed before arriving at FTOF. Figure 3.5 (left) shows the difference between the horizontal position at FTOF calculated from the down-track and the center position of hit segment. Figure 3.5 (right) shows the difference between the vertical position at FTOF calculated from the down-track and the y position calculated by the time difference from the signals of the top and bottom PMTs. The vertical position resolution of FTOF was typically 22 mm (σ). The cut positions are shown by arrows.

Consistency between up-track and down-track in vertical plane

If there was no x component in the magnetic field, the up-track and down-track would be identical in the vertical plane. In reality, the magnetic field had some x components and the two tracks in the vertical plane were a little different. However the difference should not be so large. Figure 3.6 shows the difference between the y position at DC1Y calculated from down-track and the hit information of DC1Y and the difference between slopes (dy/dz) of up-track and down-track in the vertical plane. In order to reject decay events, we set the accept regions for each plot shown by the arrows. This region was determined by the Monte Carlo simulation. In order to connect the up-track and down-track in the vertical plane, the combination with the smallest difference was chosen.

Consistency between up-track and down-track in horizontal plane

In the horizontal plane, the trajectory was bent in the magnetic field. We defined the following values, "*bendpoint*", "l_{up}" and "l_{down}". The *bendpoint* is the crossing point of the up-track and down-track in the horizontal plane. The l_{up} and l_{down} are the distance

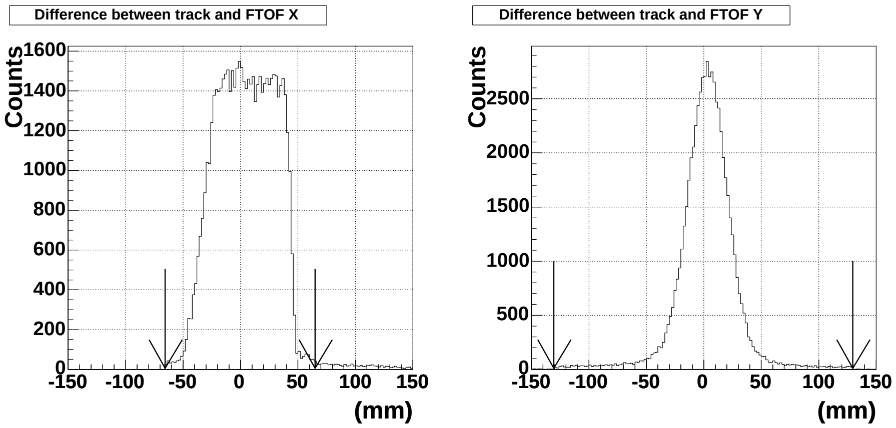

Figure 3.5: (left) Difference between the horizontal position at FTOF calculated from the down-track and the center position of the hit FTOF segment. (right) Difference between the vertical position at FTOF calculated from the down-track and the y position calculated by the time difference of the top and bottom PMTs. The arrows show the cut positions.

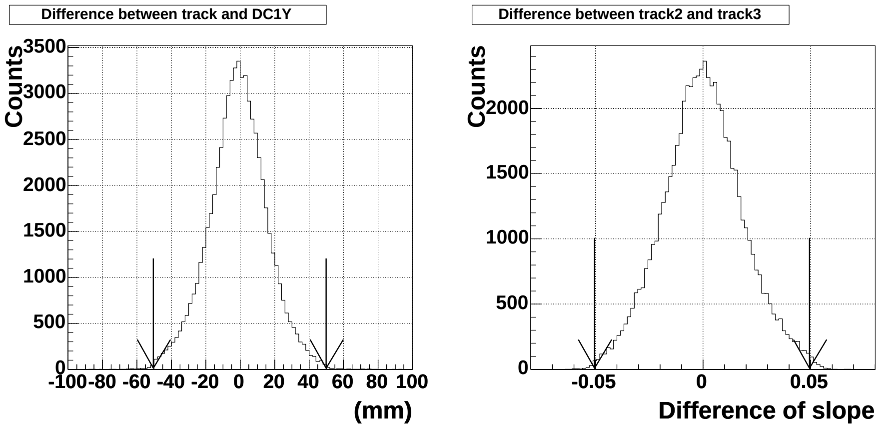

Figure 3.6: (left) Difference between the y position at DC1Y calculated from down-track and the hit information of DC1Y. (right) Difference between slopes (dy/dz) in the vertical plane of up-track and down-track. The arrows show the cut positions.

between the entrance point of the KURAMA and the *bendpoint* and the distance between the *bendpoint* and the exit point of the KURAMA. Figure 3.7 shows the difference between l_{up} and l_{down}. We accepted the events within the arrows. In order to connect the up-track and down-track in the horizontal plane, the combination with the minimum difference was chosen.

Runge-Kutta tracking

In order to connect the up-track and down-track considering the equation of motion of the particle in the magnetic field, we used the Runge-Kutta tracking method [71]. The field strength was calculated using the field map mentioned in Section 2.4.1. The Runge-Kutta tracking has the following five parameters to be determined,

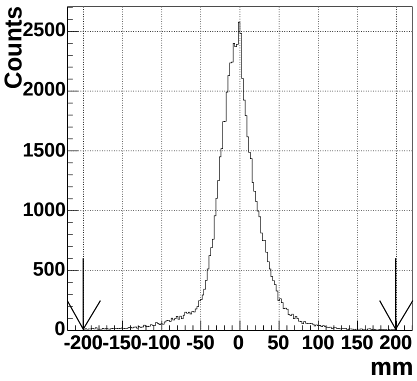

Figure 3.7: Difference between l_{up} and l_{down}. The arrows show the cut positions.

x_{FTOF} : x coordinate of hit position at FTOF,
y_{FTOF} : y coordinate of hit position at FTOF,
a_{FTOF} : slope in the horizontal plane (dx/dz) at FTOF,
b_{FTOF} : slope in the vertical plane (dy/dz) at FTOF,
p_0 : Q/p charge divided by momentum.

The momentum was determined as $p = 1/p_0$. The values obtained from the local tracking were used as initial values of these parameters. These parameters were calculated to minimize the χ^2 value defined below and the calculation was iterated until the convergence criterion of $\delta\chi^2 = (\chi^2_{k+1} - \chi^2_k)/\chi^2_k < 10^{-3}$ was satisfied, where k is the number of iterations and χ^2_k is the χ^2 value for the k-th iteration. The χ^2 value of each track is defined as

$$\chi^2_{RGK} = \frac{1}{n-5} \sum_{i=1}^{n} \left(\frac{x_i^{tracking} - x_i^{data}}{w_i} \right)^2 , \tag{3.6}$$

where n is the number of the chamber planes with a hit, $x_i^{tracking}$ and x_i^{data} are the hit positions on the i-th plane in the tracking and the data, respectively, and w_i is the position resolution of i-th plane. The typical number of the iteration was five.

Figure 3.8 shows the obtained χ^2 distributions for the (π^-, K^-) and (π^+, K^+) data. The calculated momentum distribution for the (π^-, K^-) trigger data is shown as the open histogram in Figure 3.9. The momentum distribution for K^-'s is also shown in Figure 3.9 by the hatched histogram where K^-'s were selected by mass cut discussed in Section 3.3.2. In the (π^-, K^-) reaction, the momenta of scattered K^-'s ranged from 0.4 to 1.1 GeV/c. Therefore the effect of multiple scattering made the χ^2 distribution of the Runge-Kutta tracking broader than ideal one. To study the cut position, we compared with the distribution obtained by the Monte Carlo simulation as shown by the hatched histogram in Figure 3.8. The simulated χ^2 distribution reproduced real data except for a long tail towards large χ^2, not only for the (π^-, K^-) data but also for the (π^+, K^+) data as shown in Figure 3.8 (b) where the typical momenta of K^+'s were around 1.6 GeV/c. From this study, we selected $\chi^2 < 6.0$ region where the χ^2 distribution was almost consistent with the simulation.

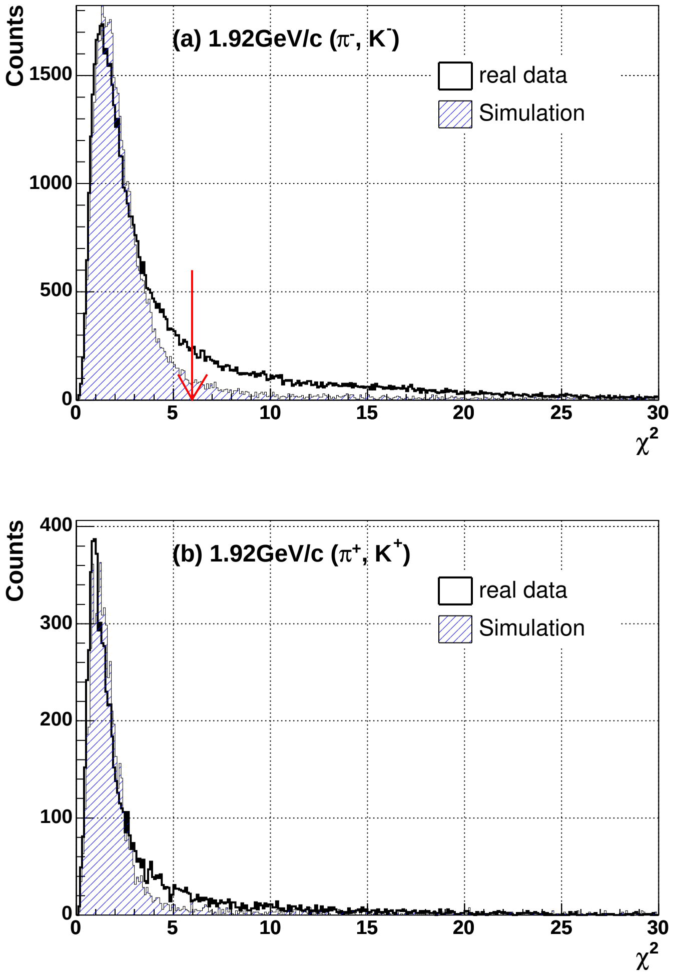

Figure 3.8: The χ^2 distributions of the Runge-Kutta tracking (a) for the (π^-, K^-) data and (b) for the (π^+, K^+) data at the beam momentum of 1.92 GeV/c. The open histogram shows the obtained distribution from real data and the hatched histogram shows one obtained by the simulation. The arrow shows the cut position of the χ^2 cut which was determined considering that the data and simulation were almost consistent for the events with smaller χ^2 than this cut position.

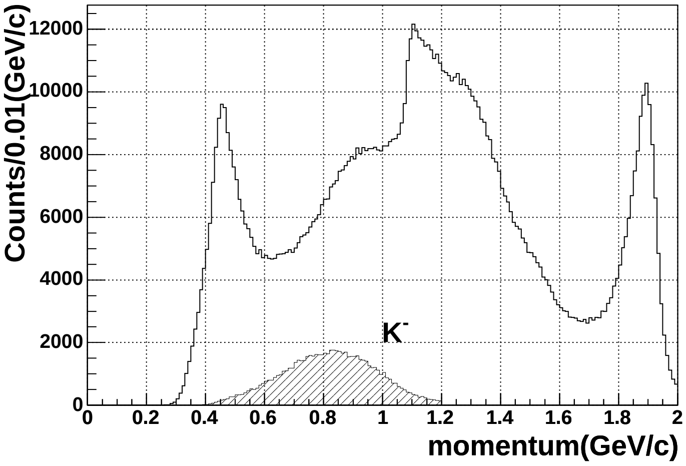

Figure 3.9: Reconstructed momentum using the Runge-Kutta tracking for the (π^-, K^-) trigger data. The hatched histogram represents the momentum distribution for K^- selected by mass cut discussed in Section 3.3.2. The peak around 1.9 GeV/c is corresponding to the π^- beam-through events. The events with momenta between 0.45 GeV/c and 1.1 GeV/c were suppressed if the particle was not K^- because we rejected particles other than K^- using the mass trigger.

3.3.2 Mass reconstruction of outgoing particles

The mass of each outgoing particle was reconstructed using the information of the momentum, flight length and flight time. The momentum and flight length were obtained by the Runge-Kutta tracking as discussed in Section 3.3.1. The flight time was obtained from the time-of-flight between T2 and FTOF. Because this time-of-flight included both the flight time of π^- between T2 and the reaction point and the flight time of K^- between the reaction point and FTOF, we subtracted the contribution of π^- using the distance between T2 and the obtained vertex point which will be described in Section 3.4. Then we obtained the flight time of K^-. The velocity and mass of the outgoing particle were calculated by the following equations,

$$\beta = \frac{L}{T \times c}, \tag{3.7}$$

$$M = P \times \frac{\sqrt{1-\beta^2}}{\beta}, \tag{3.8}$$

where L, T and P denote the flight length, flight time and momentum, respectively. Figure 3.10 shows the obtained mass spectrum.

In order to adjust the absolute value of the mass, the calibration of the time-of-flight between T2 and FTOF is important. The calibration was done in the following way. At first, the outgoing particles which might be considered to be π^- were selected using only time-of-flight information. Then we calculated the predicted time-of-flight (T_{pred}) using the momentum, flight length, and mass of π^-. We obtained the time difference (ΔT) between the T_{pred} and the measured time-of-flight ($T_{measure}$),

$$\Delta T = T_{pred} - T_{measure}. \tag{3.9}$$

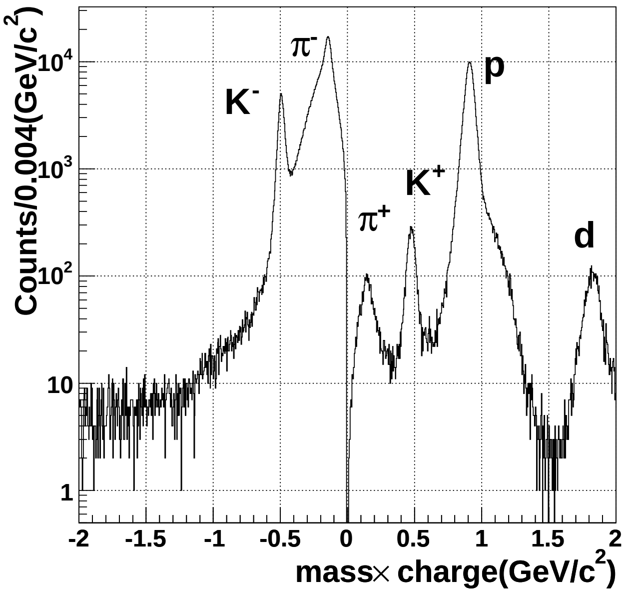

Figure 3.10: Distribution of obtained masses of outgoing particles

The time offset was adjusted to make ΔT be zero. The mass resolution of π^- was almost determined by the resolution of the time-of-flight. Conversely, there were few effects propagated from the error of the momentum measurement. Therefore we used π^- for the calibration. The time resolution was obtained from ΔT spectra to be 132 ps as the mean value of 24 segments of FTOF.

Mass resolution

Figure 3.11 shows the mass resolution (σ of mass square) as a function of momentum for proton, K^- and π^-. In case of proton and K^-, we divided into two event sets with $\chi^2_{RGK} < 5$ and $\chi^2_{RGK} > 5$ and obtained mass resolution for each event set. We recognized that the resolution became worse for larger χ^2_{RGK} events.

The mass resolution is parametrized by the following equation,

$$\sigma^2_{M^2} = 4M^4\left(1+\left(\frac{M}{p}\right)^2\right)a_1^2 + 4M^4p^2a_2^2 + 4p^2(p^2+M^2)\left(\frac{c}{L}a_3\right)^2, \qquad (3.10)$$

where a_1, a_2 and a_3 are parameters, M is the nominal values (PDG values) of mass of π^-, K^- and proton and c is the speed of light. The flight length (L) is set to 3280 mm which is the typical value for the spectrometer. The first and second term of equation (3.10) represent the contribution of momentum resolution. The momentum resolution can be evaluated as

$$\left(\frac{\sigma_p}{p}\right)^2 = \frac{a_1^2}{\beta^2} + p^2a_2^2. \qquad (3.11)$$

The first term is the contribution of multiple scattering. The second term represents the contribution of the resolution of the spectrometer.The third term of equation (3.10) is the contribution of the time-of-flight.

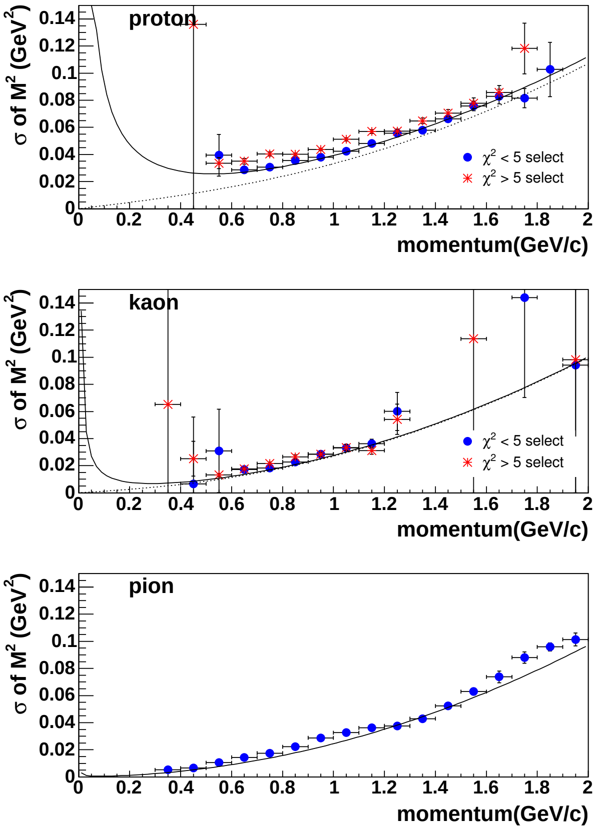

Figure 3.11: Mass resolution as a function of momentum for proton (top), K^- (middle) and π^- (bottom). The solid lines represent the expected resolution from the equation (3.10). The dotted lines show the contribution of the time-of-flight resolution. For proton and K^-, the momentum resolutions were obtained for two event samples. The circle points show the obtained resolution for events where the the χ^2 is less than 5. The star points show the resolution for events where the the χ^2 is larger than 5. For π^-, the mass resolution is almost determined by the resolution of time-of-flight and the solid and dotted lines are same.

The parameter a_1 and a_2 were obtained by fitting the same plot as Figure 3.11 obtained from the Monte Carlo simulation with the equation of (3.10). The obtained values were $a_1 = 0.00557$ and $a_2 = 0.0091$. We used $a_3 = 132$ ps as the resolution of time of flight. The solid lines in Figure 3.11 show the expected mass resolution obtained from equation (3.10) using these parameters. The dotted lines show contribution of time-of-flight resolution. It is not shown for π^- because it is same with the solid line. The mass resolution was almost reproduced by the parameterization function. The contribution from momentum resolution appears in the mass resolution significantly for proton, while the mass resolution for other particles were almost determined by time-of-flight resolution. For proton, the obtained mass resolution was almost consistent with the expected one. Therefore we believe that the best possible intrinsic-resolution of the spectrometer is obtained. The momentum resolution was obtained to be 1.0% (rms) for 0.8 GeV/c K^-.

Selection of the scattered K^- mesons

Because the mass resolution is a function of momentum, the scattered K^-'s were selected by the mass gate which was dependent on the momentum. In order to determine the mass gate, the mass spectrum for each momentum was fitted with two Gaussian peaks and an exponential background of contamination of π^- as shown in Figure 3.12 (a). The gate was determined as $\pm 3\sigma$ region of the broader Gaussian peak for each momentum as shown by the red lines in Figure 3.12 (b). The K^- identification efficiency is expected to be larger than 99.7%. The π^- contamination ratio within the mass gate was estimated by integrating the background function obtained by the fitting between the mass gate and is shown in Figure 3.12 (c). For the momentum range of $0.6 < p < 0.9$ GeV/c which is corresponding to the Θ^+ production, the π^- contamination was obtained to be ~3%.

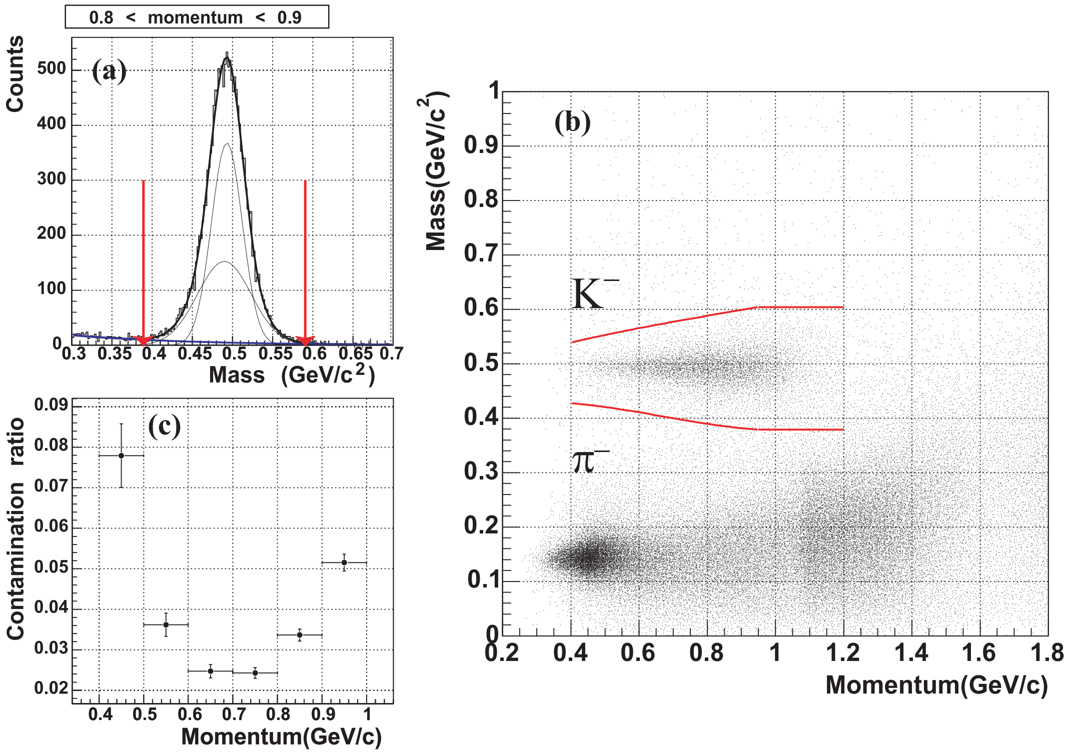

Figure 3.12: (a) Mass spectrum of outgoing particles with momentum of 0.8 GeV/$c < p <$ 0.9 GeV/c. The histogram was fitted with the two Gaussian peaks and an exponential background. The arrows show the $\pm 3\sigma$ region of the broader Gaussian peak. (b) Scattered plot of momentum and mass. The lines represent the mass gate obtained as $\pm 3\sigma$ region for each momentum. (c) Contamination ratio of π^- within the mass gate.

3.3.3 Momentum correction

We found that there was the correlation between momenta and scattering angles in the horizontal plane at the target ($\frac{dx}{dz}$) of scattered particles by investigating the scattered plot of $\frac{dx}{dz}$ and Σ^+ peak position obtained from the (π^+, K^+) reaction as shown in the left figure of Figure 3.13. This correlation appears to be caused by imperfection of the used field map. Because the field map was measured at the experiment several years ago and in the present experiment the additional materials such as the magnetic shields of image intensifier tube (IIT) for SCIFI detector were added, there can be some differences between the field map and the real magnetic field. In order to obtain better missing mass resolution, we have to correct momentum to remove such correlation. Because the Σ^+ events were not sufficient statistically and the momentum range was larger than that of the (π^-, K^-) reaction, the (K^-, p) reaction was used to correct the momentum as described following.

The same kind of correlation existed between $\frac{dx}{dz}$ and the calculated proton mass at (K^-, K^+) data set as shown in Figure 3.14 (bottom). Because the effect of momentum for mass of π^+ and K^+ is smaller than that for proton as described in Section 3.3.2, the correlation for π^+ and K^+ did not appear. We corrected the momentum so as to make the calculated proton mass constant in every $\frac{dx}{dz}$ region as shown in 3.14 (top) where events with momentum of 0.4 GeV/c $< p <$ 1.1 GeV/c were selected in order to obtain the corrected momentum of the same range with the (π^-, K^-) reaction. The missing mass spectrum of the (π^+, K^+) reaction applied this correction is shown in the right figure of Figure 3.13, where this correlation is removed. We also applied this correction to the (π^-, K^-) data.

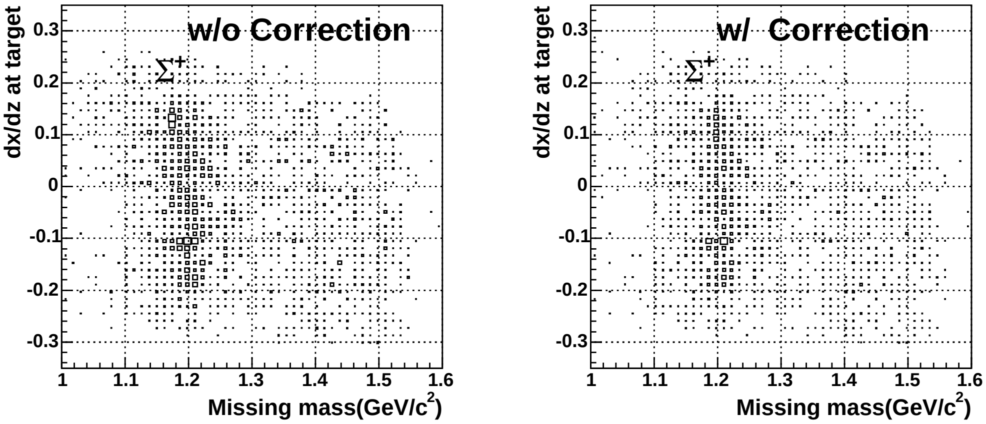

Figure 3.13: Scattered plot between missing mass of the (π^+, K^+) data and the scattering angle in the horizontal plane at the target ($\frac{dx}{dz}$) without momentum correction (left) and with momentum correction (right). The loci are corresponding to Σ^+.

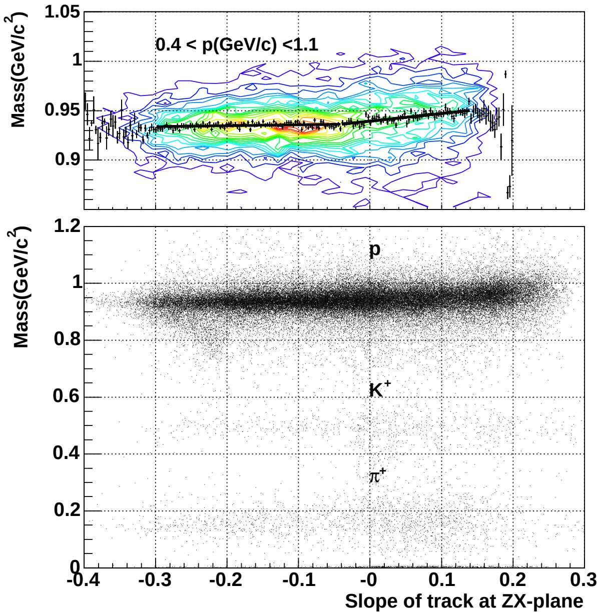

Figure 3.14: Scattered plots between the $(\frac{dx}{dz})$ at the target and masses obtained from (K^-, K^+) data set. Top figure is the expansion around proton mass where the momentum range of 0.4 GeV/c $< p <$ 1.1 GeV/c was selected.

3.4 Vertex reconstruction

The reaction vertex point $(x_{vtx}, y_{vtx}, z_{vtx})$ was obtained by the closest distance between tracks of beam and outgoing particles. Figure 3.15 shows the vertex distribution of the (π^-, K^-) reaction. The beam size (1.4 × 1.3 cm^2) was small enough in comparison with the target size. Therefore any cut was not applied for x_{vtx} and y_{vtx}. In the distribution of z_{vtx}, the image corresponding to the polyethylene target and the VH are clearly recognized. We required the vertex point to be less than 80 mm from the target center as shown by the arrows in Figure 3.15. The background events attributed to materials other than the target were estimated from the analysis of the empty target data and the contamination ratio was obtained to be 0.6%. Because the SCIFI target enabled us to see particle trajectories as image data, we could estimate the efficiency of this vertex cut precisely by comparing the vertex position calculated by the spectrometer (vtx_{SP}) and one obtained by the image data (vtx_{SCIFI}). Figure 3.16 (top) shows the typical SCIFI image which zooms into the vertex point. The vtx_{SCIFI} was obtained by human eyes. Figure 3.16 (bottom) shows the vtx_{SP} distribution for events with -50 mm $< vtx_{SCIFI} <$ 50 mm , where ±50mm is thickness of the polyethylene target. By applying the cut of -80 mm $< vtx_{SP} <$ 80 mm for these events, the efficiency of this vertex cut was obtained to be 92.8±0.5%.

We also checked the distribution of the closest distance between tracks of beam and outgoing particles at the vertex point as shown in Figure 3.17. The events where the closest distance was greater than 7mm, which corresponded to 3σ, were rejected considering that beam or outgoing particles reacted more than 2 times in the target.

Scattering angle was determined by the local tracks of the π^- beam and scattered K^-. The scattering angle for the (π^-, K^-) events ranged from 0 degree to 20 degree and mean value of the scattering angle was 8.2 degree as shown in Figure 3.18.

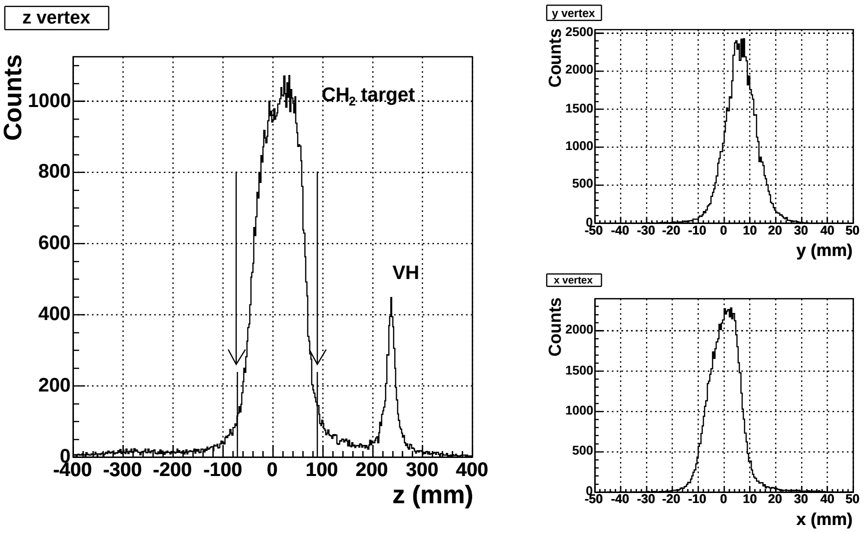

Figure 3.15: Vertex distributions of the (π^-, K^-) reaction. The arrows show the cut position for the vertex cut.

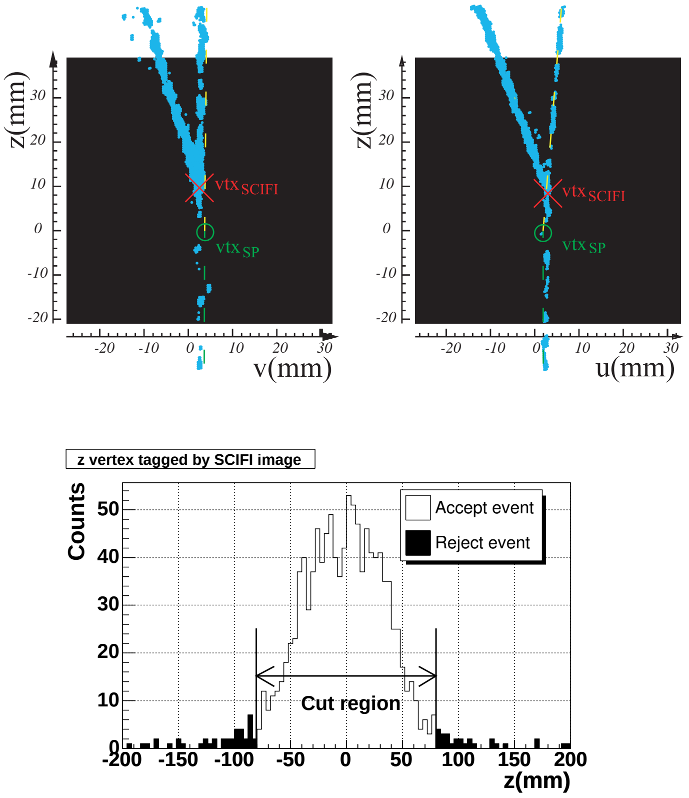

Figure 3.16: (top) Typical SCIFI image around the vertex point. The vtx_{SCIFI} and vtx_{SP} are the vertex point obtained from image data and analysis of spectrometer, respectively. (bottom) vtx_{SP} distribution for events with -50 mm $< vtx_{SCIFI} <$ 50 mm , where ±50mm is thickness of the polyethylene target. The open and solid histogram represent the accepted and rejected event by the vertex cut. The accepted ratio was 92.8±0.5%.

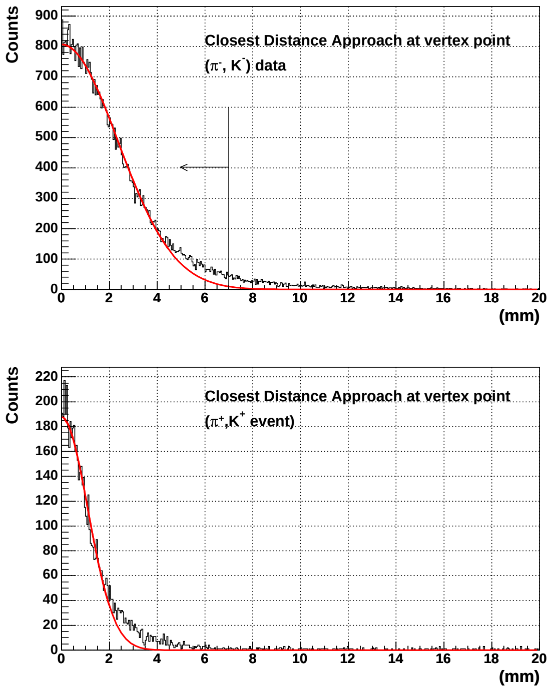

Figure 3.17: Distribution of the closest distance between tracks of beam and outgoing particles at the vertex point. The solid lines show the fitting results with a Gaussian function. The accepted region is shown by an arrow which corresponds to the 3σ point of the fit.

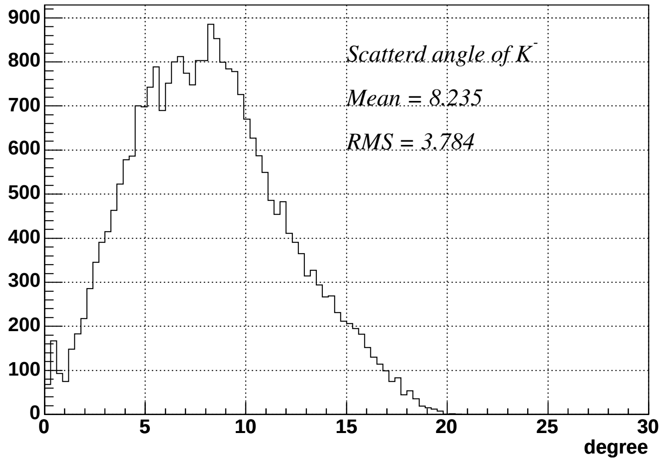

Figure 3.18: Scattering angle distribution of the (π^-, K^-) reaction.

cut	criteria	efficiency(%)
	π^- selection	
Time-of-Flight cut	3σ region	93.8 ± 0.1
beam χ^2 cut	C.L. 95% region	84.6 ± 0.1
beam momentum cut	$1.8 < P_{\pi^-}(\mathrm{GeV}/c) < 2.0$	94.8 ± 0.1
	K^- selection	
mass-momentum cut	3σ region (p dependent)	> 99.7
Runge-Kutta χ^2 cut	$\chi^2_{RGK} < 6$	72.7 ± 0.2
	vertex selection	
vertex cut	$-80 < z_{vtx}(\mathrm{mm}) < 80$	92.8 ± 0.5
closest distance cut	< 7mm (3σ)	97.8 ± 0.1
total		49.6 ± 0.3

Table 3.1: Summary of the analysis cuts and their efficiencies. Errors are statistical ones. This is a cut summary applied for the events where beam and outgoing particles are found in the analysis program.

3.5 Summary of the analysis cut

We have mentioned the analysis procedure of the (π^-, K^-) data. In order to select good (π^-, K^-) events, we applied the following cuts for the events where beam and outgoing particles were found in the analysis program,

1. selection of π^- in the beam and its momentum analysis,
2. identification of the scattered K^- and its momentum analysis,
3. selection of the reaction vertex point,

as described in the previous sections. Here, we summarize the criteria and efficiencies of these cuts in Table 3.1. The efficiencies will be used to derive the production cross section of the Θ^+.

3.6 Missing mass spectrum of the $\pi^+ p \to K^+ X$ reaction

In the missing mass spectrum of the $\pi^- p \to K^- X$ reaction, there might not be any peaks of hadron resonances other than the Θ^+. Therefore it is quite important to check the validity of the analysis from the missing mass spectrum of calibration data. In this experiment, we measured the $\pi^+ p \to K^+ \Sigma^+$ reaction for this purpose.

Missing mass is defined as the invariant mass of an undetected residual system assuming the target particle to be at rest. In the reaction $1 + 2 \to 3 + X$, where 1 is the incident particle, 2 is the target particle, and 3 is the outgoing particle, the missing mass M_X is calculated as,

$$M_X = \sqrt{(E_1 + M_2 - E_3)^2 - (p_1^2 + p_3^2 - 2p_1 p_2 \cos\theta)}, \qquad (3.12)$$

where E_i and p_i is the energy and momentum of particle i, M_2 is the rest mass of the target particle, and θ is the scattering angle of the particle 3 from the direction of the particle 1. The p_1 and p_3 is the momentum at the reaction point. The energy loss in the target was corrected using the reconstructed momenta of the incident and outgoing particles with their directions and the calculated vertex point. The vertex resolution decreased for the events with small scattering angle. When the scattering angle was less than 4 degree, the energy loss was corrected assuming that the reaction vertex was the center of the target.

Figure 3.19 shows the missing mass spectrum of the (π^+, K^+) reaction at the beam momentum of 1.92 GeV/c. The peak due to Σ^+ is clearly observed. The beam momentum was normalized so as to make the obtained Σ^+ peak consistent with the PDG value. We fitted this spectrum with two Gaussian functions assuming that the broad peak was attributed to quasi-free reactions in carbon and the narrow one was attributed to free protons. The obtained width of the narrow peak was 33.3±4.8 MeV/c^2 (FWHM) which was almost consistent with the expected value of 28.3 MeV/c^2 from the Monte Carlo simulation. To estimate the missing mass resolution in the simulation, the position resolutions of the drift chambers, the momentum resolution of the beam spectrometer and the effects of the energy loss and the multiple scattering in materials for incident and outgoing particles were taken into account.

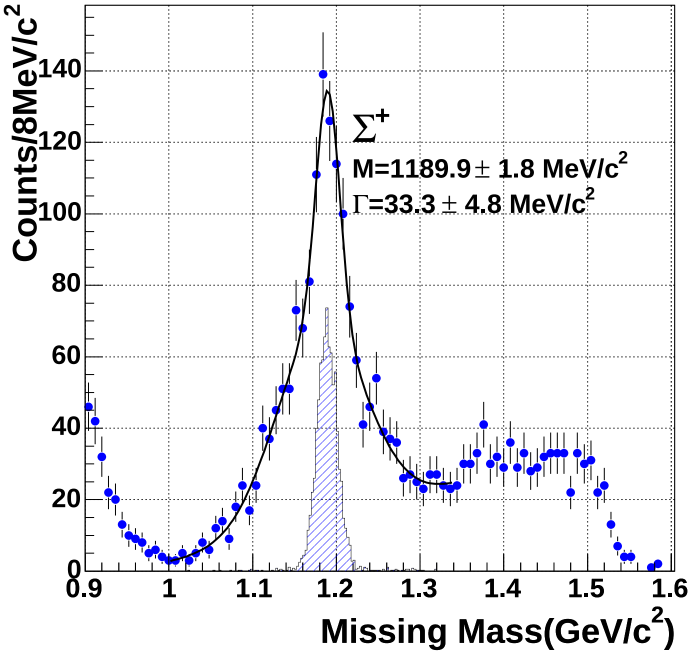

Figure 3.19: Missing mass spectrum of the (π^+, K^+) reaction with a polyethylene target. The beam momentum was adjusted so as to make the obtained Σ^+ peak consistent with the PDG value. The hatched spectrum is the expected spectrum from the simulation. The obtained peak width of 33.3 ± 4.8 MeV/c^2 (FWHM) is almost same with the expected value of 28.3 MeV/c^2.

3.7 Missing mass resolution for Θ^+

Using the same Monte Carlo simulation, the missing mass resolution for the Θ^+ was estimated to be 13.4 MeV/c^2 (FWHM). In the Θ^+ production, the momentum of the outgoing particle is much lower than that in the Σ^+ production. Therefore the missing mass resolution for the Θ^+ is better than that for the Σ^+ hyperon.

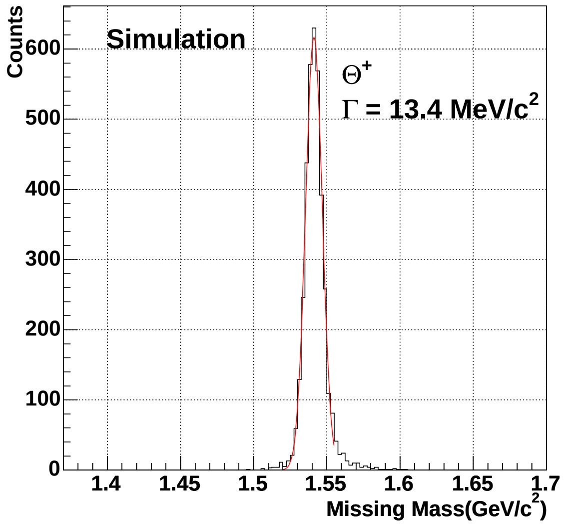

Figure 3.20: Expected missing mass spectrum for the Θ^+. The missing mass resolution was obtained to be 13.4 MeV/c^2 (FWHM).

3.8 Consistency in the (π^-, K^-) data

In Section 3.6, we confirmed that the expected resolution was obtained using the $\pi^+p \rightarrow K^+\Sigma^+$ reaction. Because the polarities of the KURAMA magnet and magnets in the beam line were inverse in the (π^+, K^+) and (π^-, K^-) reactions, it was desirable to confirm the validity of the missing mass resolution for the Θ^+ by reconstructing some particles from a missing mass or invariant mass using the (π^-, K^-) data. For this purpose, we checked by the following two ways. The first one was to reconstruct the invariant mass for the multi-track events detected in the forward spectrometer and check the width and peak position of the reconstructed particle. The other was to reconstruct K^0_S meson from the missing mass of the $\pi^-p \rightarrow K^-pX$ reaction using the image data.

3.8.1 Invariant mass spectrum

The forward spectrometer had a small acceptance for multi particles with different charges, because it was designed to have the maximum acceptance for particles with negative charge. However there were some multi-track events, of which fraction was small, where the both particles were detected in the spectrometer. Figure 3.21 shows the invariant mass spectrum of π^- and proton system. We can recognize the sharp peak corresponding to Λ hyperon. The blue histogram is the background shape estimated using the mixed event technique and reproduces well the spectrum other than the peak. The hatched histogram is the expected spectrum obtained from the Monte Carlo simulation. The mass and width were obtained to be $M = 1113.7 \pm 0.4$ MeV/c^2 and $\sigma = 2.4 \pm 0.3$ MeV/c^2, respectively, by fitting the histogram after the subtraction of the estimated background as shown in Figure 3.21 (b). The width was consistent with the expectation. The obtained mass was slightly shifted from the world average value of $M = 1115.683 \pm 0.006$ MeV/c^2.

Figure 3.22 shows the invariant mass distribution of K^- and proton system where the peak corresponding to $\Lambda(1520)$ is seen. The histogram was fitted with a Gaussian function and background which was assumed to be an exponential function. The obtained results were that the mass was $M = 1520.5 \pm 2.6$ MeV/c^2 and the width was $\sigma = 13.4 \pm 2.2$ MeV/c^2. The obtained width was consistent with the simulated value of 12.7 MeV/c^2 obtained from the Monte Carlo simulation within the error. The world average mass is 1519.5±1.0 MeV/c^2 and the obtained mass was consistent within the error.

From these results, we checked that the obtained widths for the reconstructed particles were consistent with the simulated values. Therefore we concluded that we obtained the expected momentum resolution for outgoing particles. The obtained peak positions were slightly shifted from the world average values. The shift will be discussed in relation to the systematic error of absolute value in the missing mass of the $\pi^- p \to K^- X$ reaction in Section 4.2.1.

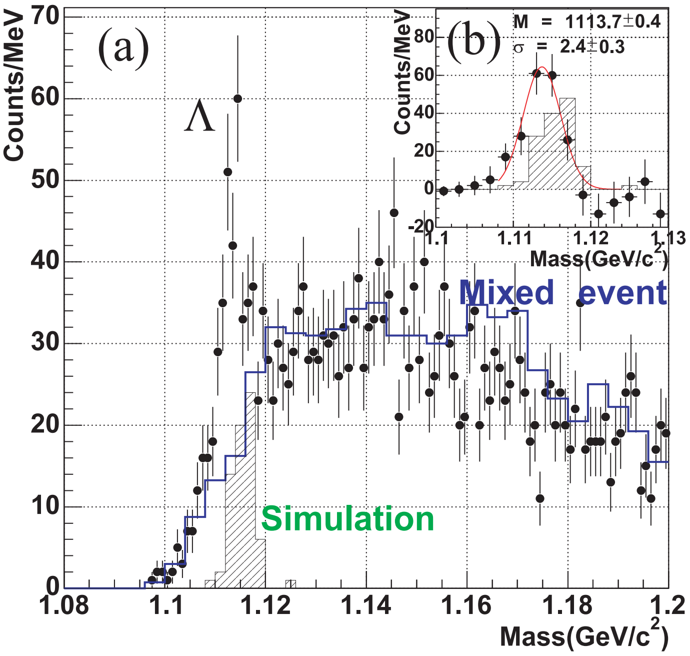

Figure 3.21: (a)Invariant mass spectrum of π^- and proton system. The peak around 1.115 GeV/c^2 is the $\Lambda(1115)$. The histogram with the blue solid line is the background estimated using the mixed event technique. The hatched histogram shows the expected peak shape obtained from the Monte Carlo simulation. (b) Peak structure after the subtraction of the estimated background. By fitting this histogram with a Gaussian function, the mass and width were obtained to be $M = 1113.7 \pm 0.4$ MeV/c^2 and $\sigma = 2.4 \pm 0.3$ MeV/c^2, respectively. The hatched histogram is the same one with the simulated histogram shown in (a).

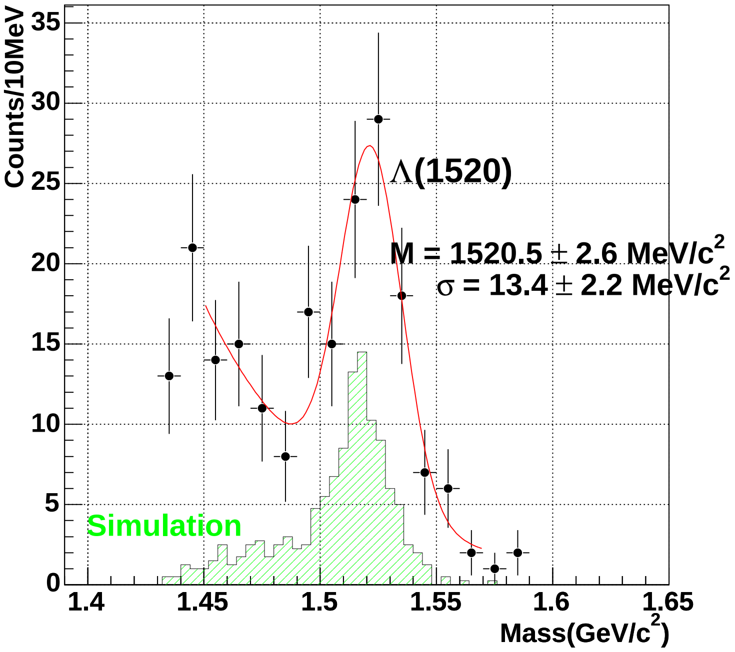

Figure 3.22: Invariant mass spectrum of K^- and proton system. The peak of $\Lambda(1520)$ is seen. The mass and width was obtained to be $M = 1520.5 \pm 2.6$ MeV$/c^2$ and $\sigma = 13.4 \pm 2.2$ MeV$/c^2$, respectively. The hatched histogram shows the expected peak shape obtained from the Monte Carlo simulation.

3.8.2 Missing mass spectrum of the $\pi^- p \to K^- p X$ reaction

In order to check the performance of the missing mass measurement in the (π^-, K^-) data, we reconstructed the K^0_S meson from the missing mass of $\pi^- p \to K^- p X$ reaction using the image data. By the analysis of the spectrometer, the momenta of the incident π^- and the outgoing K^- were measured. In addition, much more information was obtained by using the image data, because the SCIFI detector was the 4π tracking detector. In particular, the tagging of K^0_S meson decaying into π^+ and π^- mesons and the measurement of the scattering angle of the proton were the key points in this analysis. The analysis procedure is following. Figure 3.23 shows a supporting illustration of the analysis procedure.

1. Tag the K^0_S production events by selecting the "V" topology which indicated that a neutral particle, after some flight length, decayed into two charged particles.

2. Require that the number of the charged particles produced at the reaction point was two. The two tracks were corresponding to the K^- meson and the proton. When the π^- beam interacted with ^{12}C nucleus, the additional tracks of the fragmentation production from the nucleus were seen. These events were rejected because these events made the broad background due to the Fermi motion of proton in the nucleus.

3. Reconstruct the scattering angle, that is the direction vector, of the proton from the two sets of 2-dimensional image.

4. As the events where the particles in the final state were the K^-, K^0_S and proton, the following two reactions are considered,

$$\pi^- p \to K^- K_S^0 p \quad \text{(phase space)},$$
$$\pi^- p \to K^0 \Lambda(1520) \to K^- K_S^0 p \quad (\Lambda(1520) \text{ production}).$$

We assumed that K^- and proton were the decay products from $\Lambda(1520)$. Because the scattering angle of the proton were measured using the image data, the momentum could be calculated.

5. Calculate the momentum of the proton to make the invariant mass of the proton and the K^- be the mass of $\Lambda(1520)$. Although the $\Lambda(1520)$ has the natural width of 15.6±1.0 MeV/c^2, the central value of the mass was used. Therefore there was the uncertainty due to the width in the calculated momentum.
6. From these information, the missing mass of the $\pi^- p \to K^- pX$ reaction was calculated. For the phase space events, the calculated momenta of the protons were not correct, because we assumed that K^- and proton were the decay products from $\Lambda(1520)$. Therefore phase space events made the continuous background. On the other hand, the true $\Lambda(1520)$ production events should make the peak corresponding to the K^0 meson.

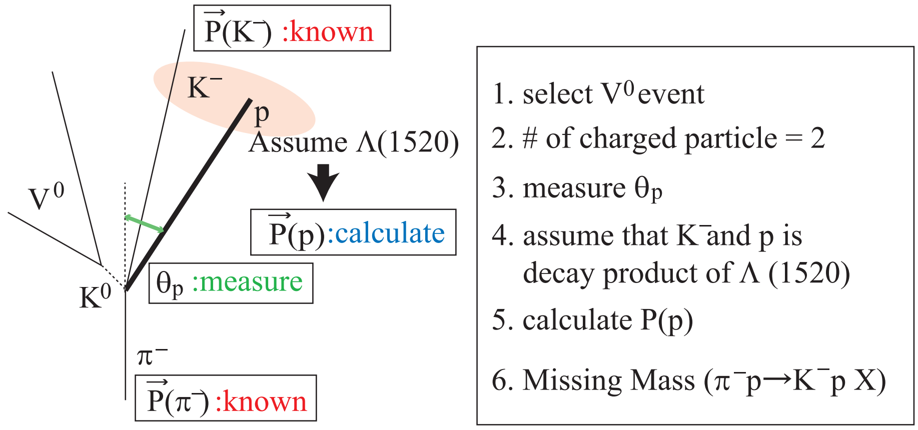

Figure 3.23: Supporting illustration of the derivation of the missing mass of the $\pi^- p \to K^- pX$ reaction.

Figure 3.24 shows the missing mass of the $\pi^- p \to K^- pX$. The peak corresponding to the K_S^0 meson can be recognized. The simulated spectra for the phase space events and $\Lambda(1520)$ production events are also shown by the hatched spectra. Because the momentum of proton was calculated using the central value of the mass of $\Lambda(1520)$, the shape of the reconstructed K_S^0 meson became a Lorentz function. The obtained missing mass spectrum can be understood as the sum of these contributions. The peak position was obtained to be $M = 498.1 \pm 5.2$ MeV/c^2 by fitting this spectrum with the Lorentz function. The obtained mass was consistent with the PDG value of 497.67 MeV/c^2.

As discussed above, the obtained peak position of the K_S^0 meson was consistent with the PDG value. The shape of the spectrum was consistent with the Monte Carlo simulation. Therefore we consider that the analysis for both incident and outgoing particles has been executed correctly. From these studies, we conclude that the missing mass resolution of 13.4 MeV/c^2 for the Θ^+ calculated by the Monte Carlo simulation is reliable.

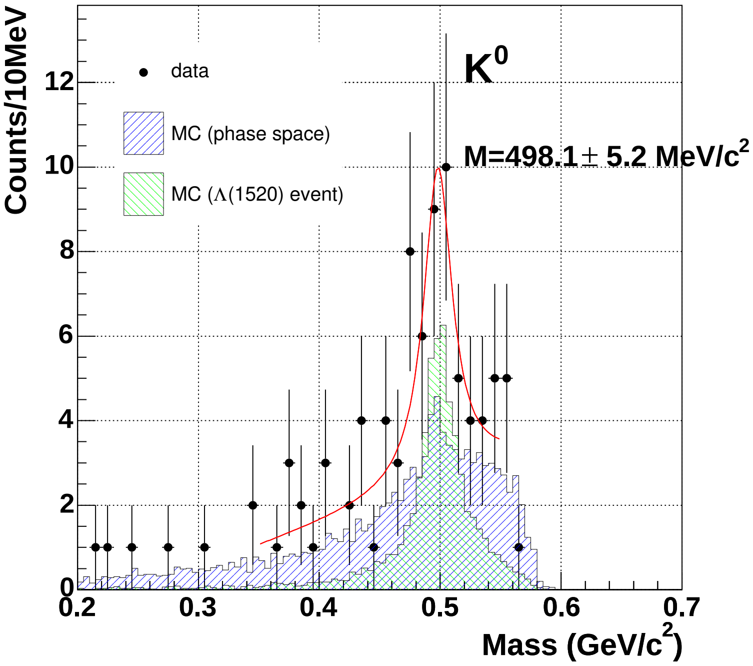

Figure 3.24: Missing mass spectrum of the $\pi^- p \rightarrow K^- p X$ reaction where the K^0 meson was tagged by selecting the "V" topology in the image data. The peak corresponding to the K^0 meson is recognized. The peak position was obtained to be 498.1 ± 5.2 MeV/c^2 by fitting with the Lorentz function. The blue and green hatched histograms show the Monte Carlo simulations for the phase space events and the $\Lambda(1520)$ events, respectively.

f_{beam}	beam normalization factor	83.6 ± 1.3%
ϵ_{K2}	tracking efficiency of K2 beamline	72.7 ± 2.0%
ϵ_{track}	tracking efficiency of scattered particle	84.6 ± 2.0%
$f_{\check{C}erenkov}$	Čerenkov overkilling factor	90.8 ± 0.8%
f_{decay}	decay factor	57.6 ± 0.1% / 55.0 ± 0.1%
$f_{K^{-}int}$	K^- interaction factor	89.8 ± 0.1% / 90.7 ± 0.1%
ϵ_{MT}	efficiency of mass trigger	95.7 ± 0.1%
ϵ_{DAQ}	DAQ live time	93.5 ± 0.2%
ϵ_{ana}	efficiency of analysis	49.6 ± 0.3%

Table 3.2: Summary of the various efficiencies for the calculation of the production cross section. The $f_{K^{-}int}$ and f_{decay} were obtained for 1.87 GeV/c and 1.92 GeV/c, respectively. The former value is for 1.92 GeV/c and the latter value is for 1.87 GeV/c.

3.9 Cross section

After the derivation of the missing mass spectrum of the $\pi^- p \rightarrow K^- X$ reaction, we discuss the production cross section of the Θ^+. In order to obtain the cross section, detection and analysis efficiencies have to be estimated. The cross section is calculated from the experimental yields as

$$\begin{aligned} \left(\frac{d\sigma}{d\Omega}\right) &= \frac{1}{N_{target}} \cdot \frac{1}{N_{beam} \cdot f_{beam} \cdot \epsilon_{K2}} \cdot \frac{1}{\epsilon_{DAQ}} \cdot \frac{N_{\Theta^+}}{\epsilon_{KURAMA} \cdot \epsilon_{ana} \cdot d\Omega}, \\ N_{target} &= \frac{2 \cdot (\rho x) \cdot N_{Avo}}{14} \ (polyethylene), \ \frac{(\rho x) \cdot N_{Avo}}{13} \ (SCIFI), \\ \epsilon_{KURAMA} &= \epsilon_{track} \cdot f_{decay} \cdot f_{K^{-}int} \cdot f_{\check{C}erenkov} \cdot \epsilon_{MT}. \end{aligned}$$

Here N_{Θ^+}, N_{beam} and N_{target} represent the number of Θ^+, beam particles and protons in the target. The solid angle covered by the forward spectrometer at laboratory frame is represented by $d\Omega$. Other ϵ's and f's represent various experimental efficiencies, and are summarized in Table 3.2. The efficiencies include μ^-, e^- contamination effect in the beam, track-finding efficiency of incident particles, track-finding efficiency of scattered particles, overkilling of the Čerenkov counters, the decay and interaction of the outgoing K^-, the DAQ live time, the efficiencies of the mass trigger and the analysis cut. Each efficiency was calculated with various calibration data and the Monte Carlo simulation. The acceptance was calculated with the Monte Carlo simulation. The coefficient ϵ_{ana} is the analysis cut efficiency and summarized in Table 3.1. In this section, we discuss how they were obtained.

3.9.1 Normalization of beam particles

The coefficient f_{beam} is the correction factor to obtain the number of π^-. In this experiment, we could not distinguish e^- and μ^- from π^-. We referred the past experiments where a gas Čerenkov counter was used to distinguish e^- and μ^- and estimated that this contamination was 12.4±1.3% [67, 73]. We also calculated the absorption rate of π^- in the target with the GEANT simulation and obtained to be 4%. Adding these two values, we estimated f_{beam} to be 83.6±1.3%.

3.9.2 Track-finding efficiency of beam particles

The coefficient ϵ_{K2} is the track-finding efficiency for beam particles. The efficiency was estimated as a ratio of the number of events accepted as a good trajectory to that of good beam particles defined from the time-of-flight between T1 and T2. The analysis of beam particles was composed of the momentum reconstruction using BDC1,2,3 and BPC1,2 and the track measurement of the incident beam using BPC3,4,5. The former was 76.3% due to the inefficiency of BDC3 as described in Section2.3. The latter was 94.7%. The total efficiency including these two factors was obtained to be 72.7±2.0%.

3.9.3 Track-finding efficiency of scattered particles

The efficiencies of track-finding routine used in the analysis program for scattered particles have to be estimated, because the routine has criteria to find tracks such as minimum number of hit chambers and can not find out some tracks due to the inefficiency of the drift chambers or multi hit events.

The tracking efficiency is defined by the following equations,

$$\begin{aligned}
\epsilon_{down-track(ZX)} &= 1-(\epsilon(min)+\epsilon(\chi^2 cut)+\epsilon(FTOFmissX)),\\
\epsilon_{down-track(YZ)} &= 1-(\epsilon(min)+\epsilon(\chi^2 cut)+\epsilon(FTOFmissY)+\epsilon(KINKcut1)),\\
\epsilon_{up-track(ZX)} &= 1-(\epsilon(min)+\epsilon(\chi^2 cut)+\epsilon(bendpoint)),\\
\epsilon_{up-track(YZ)} &= 1-(\epsilon(min)+\epsilon(\chi^2 cut)+\epsilon(KINKcut2)),\\
\epsilon_{track} &= \epsilon_{down-track(ZX)}\times\epsilon_{down-track(YZ)}\times\epsilon_{up-track(ZX)}\times\epsilon_{up-track(YZ)},
\end{aligned}$$

where $\epsilon_{down-track(ZX)}$, $\epsilon_{down-track(YZ)}$ denote the track-finding efficiencies at the exit of KURAMA in the horizontal and vertical planes, respectively, and $\epsilon_{up-track(ZX)}$, $\epsilon_{up-track(YZ)}$ denote the same efficiencies at the entrance of KURAMA. The other ϵ's of right-hand side represent inefficiencies due to the algorithm in the analysis program. The $\epsilon(min)$ represents the inefficiency due to the lack of the hit planes. In the analysis program, we required at least three hit planes to execute straight track search. The $\epsilon(\chi^2 cut)$ represents the inefficiency due to the χ^2 cut for local tracks, where the criterion of $\chi^2 < 100$ was required. The others represent the factors which come from the consistency check between up-track and down-track as described in Section 3.3.1. The $\epsilon(FTOFmissX)$ and $\epsilon(FTOFmissY)$ are the inefficiencies which come from the check between FTOF and down-track as shown in Figure 3.5 (left) and (right), respectively. The $\epsilon(KINKcut1)$ and $\epsilon(KINKcut2)$ are the inefficiencies due to the inconsistency between up-track and down-track in the vertical plane as shown in Figure 3.6 (left) and (right), respectively. Finally the $\epsilon(bendpoint)$ is the inefficiencies corresponding to the inconsistency between up-track and down-track in the horizontal plane as shown in Figure 3.7.

The coefficient ϵ_{track} was obtained by analyzing the data produced by the Monte Carlo simulation with the same analysis program. In this Monte Carlo simulation, the measured efficiencies of the chamber planes summarized in Table 2.4 were taken into account and the decay process was not included.

Before we discuss the track-finding efficiency in the (π^-, K^-) data, the validity of this estimation was checked using scattered proton events taken with (K^-, K^+) trigger data, because proton does not decay and this made the estimation more easy. The scattered protons could be selected by using hit combination of CH and FTOF and the time-of-flight without tracking as discussed in the section of the mass trigger. Figure 3.25 shows the scattered plot between hit segment of the CH and time-of-flight of FTOF of segment 4, where there were two loci corresponding to protons and π^+'s. In order to select proton events, we applied the TOF gate shown in the solid lines in Figure 3.25, which corresponded to the 1.5σ region in order to reject contamination of other particles. We estimated the track-finding efficiency by analyzing such pre-selected proton events and obtained the results listed in the column of "proton select" of Table 3.3. The efficiencies were compared with the results obtained by analyzing the Monte Carlo data which is also listed in the column of "simulation" of Table 3.3. The difference larger than 1.0% was found in χ^2 cut. The difference is considered to be caused by the wrong TDC information of the drift chambers most likely due to the multi hit events in the same cell or some noises in the real data. Figure 3.26 shows the XT curve of DC3. In this Figure there were some events located in the wrong relation and these events were rejected by the χ^2 cut. Because this effect was not taken into account in the simulation, we concluded that the difference in χ^2 cut came from this effect. The other factors were consistent within less than 1.0%.

Because we checked the validity of the simulation, we estimated the track-finding efficiency for the (π^-, K^-) event using the Monte Carlo simulation. However the factor of the χ^2 cut was estimated with the real data. The estimated track-finding efficiency is given in the column of "(π^-, K^-) simulation" and ϵ_{track} was obtained to be 84.6±2.0%. The error was estimated from the difference between pre-selected proton events and the Monte Carlo events.

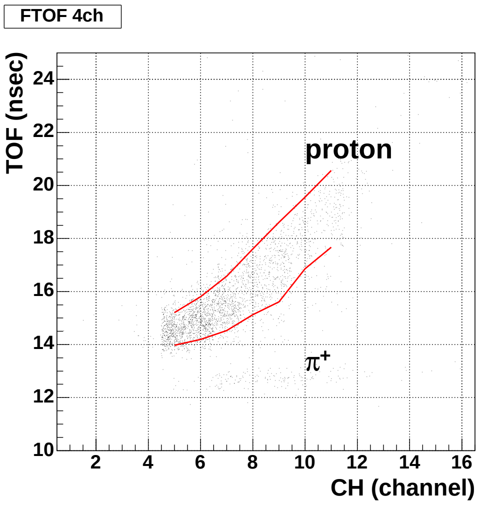

Figure 3.25: Scattered plot between hit segment of the CH and time-of-flight of the FTOF of segment 4 in the (K^-, K^+) data. There were two loci corresponding to protons and π^+'s. The solid lines are the selection region of time-of-flight of FTOF which is corresponding to 1.5σ region.

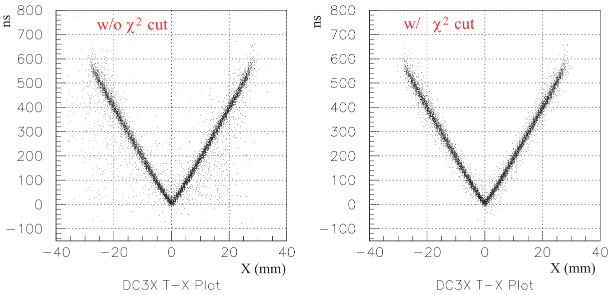

Figure 3.26: XT plots of DC3 before the χ^2 cut (left) and after the χ^2 cut (right). By applying the χ^2 cut the events with the bad XT relation were rejected.

3.9.4 Overkilling of Čerenkov counters

The coefficient $f_{\check{C}erenkov}$ represents the correction factor due to the overkilling rates of BVAC and FAC. Although the velocity of K^-'s produced in the (π^-, K^-) reaction is much smaller than the threshold values for each Čerenkov counter, some events were discriminated due to the δ-rays produced along the passage in the counters and the accidental veto under the high counting rate.

At first, we discuss the overkilling rates due to the δ-ray, $f_\delta(BVAC)$ and $f_\delta(FAC)$, for each counter. Figure 2.12 shows the efficiencies of each counter as the function of β. In this plot, the efficiency, that is overkilling rate for the K^-'s now, were measured using π^- beam of 230 MeV/c and obtained to be 6.9±1.0% for BVAC and 4.7±0.8% for FAC, respectively. While FAC had the acceptance for all outgoing particles detected in the spectrometer, BVAC had the acceptance for only particles with smaller scattering angles. The acceptance of BVAC for the K^-'s was measured from the (π^-, K^-) data and obtained to be 21.3%. The overkilling rate for BVAC was obtained by the following equation, $f_\delta(BVAC) = (6.9 \pm 1.0) \times 0.213 = 1.5 \pm 0.2\%$. The overkilling rate for FAC was obtained to be $f_\delta(FAC) = 4.7 \pm 0.8\%$.

Next we discuss the overkilling rates due to the accidental coincidence, $f_{acc}(BVAC)$ and $f_{acc}(FAC)$, under the beam intensity of 3.3×10^5 /spill. The single counting rates were 142±13 kHz and 250±22 kHz for BVAC and FAC, respectively. Considering that the gate widths for BVAC and FAC were 100 ns and 70 ns, respectively, the overkilling rates were obtained to be $f_{acc}(BVAC) = 1.42 \pm 0.13\%$ and $f_{acc}(FAC) = 1.75 \pm 0.15\%$. Taking into account the all effects, we calculated the $f_{\check{C}erenkov}$ by the following equation,

$$f_{\check{C}erenkov} = (1 - f_\delta(BVAC)) \cdot (1 - f_\delta(FAC)) \cdot (1 - f_{acc}(BVAC)) \cdot (1 - f_{acc}(FAC)). \quad (3.13)$$

The $f_{\check{C}erenkov}$ was obtained to be 90.8±0.8%.

3.9.5 Decay of the outgoing K^-

The coefficient f_{decay} represents the correction factor due to the decay ratio of the K^-'s before arriving at FTOF. The $\beta\gamma c\tau$ of the K^- with the momentum of 0.8 GeV/c is 6 m. A part of K^-'s decayed on the way of the spectrometer, of which typical flight length was 3.3 m. Using the $\beta\gamma c\tau$ and the flight length of 3.3 m, the rough estimation of the survival rate was 58%. In order to study this factor for the $\pi^- p \to K^- \Theta^+$ reaction in detail, we executed the Monte Carlo simulation for the beam momentum of 1.92 GeV/c and 1.87 GeV/c. In this simulation the Θ^+ was produced isotropically in the center of mass system. The survival rate for 1.92 GeV/c was obtained to be 57.6±0.1%. Similarly the survival rate for 1.87 GeV/c was 55.0±0.1%.

	(K^-, p)		(π^-, K^-)
	proton select	simulation	simulation
	down-track(ZX)		
$\epsilon(min)$	0.763	0.073	0.104
$\epsilon(\chi^2 cut)$	1.42	0.00	1.87
$\epsilon(FTOFmissX)$	0.535	0.293	0.241
	down-track(YZ)		
$\epsilon(min)$	0.225	0.00	0.028
$\epsilon(\chi^2 cut)$	1.53	0.00	1.49
$\epsilon(FTOFmissY)$	0.066	0.084	0.134
$\epsilon(KINKcut1)$	2.00	2.35	2.64
	up-track(ZX)		
$\epsilon(min)$	0.03	0.011	0.00
$\epsilon(\chi^2 cut)$	0.17	0.032	1.83
$\epsilon(bendpoint)$	1.51	1.43	1.49
	up-track(YZ)		
$\epsilon(min)$	5.41	3.39	3.40
$\epsilon(\chi^2 cut)$	1.09	1.05	2.11
$\epsilon(KINKcut2)$	0.670	1.05	0.860
	Tracking efficiency		
ϵ_{track}	85.4	90.5	84.6

Table 3.3: Summary of the estimations of the track-finding efficiencies of the (K^-, p) and the (π^-, K^-) data. For the (K^-, p) event, the results obtained from the pre-selected proton and Monte Carlo simulation are shown. There is a difference larger than 1% in the $\epsilon(\chi^2)$ between results obtained from the pre-selected data and simulation. This might be caused due to the wrong TDC information (see text for detail description). Estimated tracking efficiency in the $\pi^- p \to K^- \Theta^+$ reaction using Monte Carlo simulation is given in the column of "(π^-, K^-) simulation". As the $\epsilon(\chi^2)$, we adopted inefficiencies obtained from the real data.

	length (cm)	density (g/cm3)	thickness (g/cm2)	λ_I (g/cm2)
Target(CH_2)	5.0	1.0	5.0	57.0
VHX	0.2	1.07	0.214	58.3
VHY	0.2	1.07	0.214	58.3
BVAC	6.0	0.200	1.20	64
FAC	6.0	0.164	0.984	64
CH	0.2	1.07	0.214	58.3
YH	0.5	1.07	0.535	58.3

Table 3.4: Summary of the materials in the forward spectrometer. λ_I denotes the interaction length.

3.9.6 Interaction of the outgoing K^-

The coefficient f_{K^-int} represents the correction factor due to the interaction rate of K^- in the materials of the target and the forward spectrometer. The cross section of the K^-p reaction at the momentum around 0.8 GeV/c has relatively large value of about 40 mb, half of which is the elastic scattering. Along the path of the outgoing K^-, there were materials of which total thickness was 8.36 g/cm^2, as summarized in Table 3.4. Therefore some outgoing K^-'s interacted with these materials and disappeared. The interaction rate of K^- with these materials was roughly calculated to be about 13% considering the interaction length of each material. In order to estimate this interaction rate in detail, we also executed the Monte Carlo simulation based on the GEANT4. As the elastic and inelastic interaction, we used the packages included in the GEANT4. Figure 3.27 shows the interaction points or decay points of K^-'s obtained by the simulation. The blue points were the survival events where the outgoing K^- arrived at FTOF without the decay or interaction. The black points were the decay points of K^-'s. The red points indicated the inelastic reaction points. As expected, the inelastic reaction points were concentrated on the materials in the spectrometer. The green points showed the events where there were elastic scatterings with the materials and the K^-'s went off from the acceptance and stopped at the end-guard or the yoke of KURAMA. For the correction due to the interaction of K^-, we took into account the last two effects due to the inelastic and elastic interactions. The interaction rates were obtained to be 10.2±0.1% and 9.3±0.1% for the beam momenta of 1.92 GeV/c and 1.87 GeV/c, respectively. Therefore the coefficient f_{K^-int} were obtained to be 89.8±0.1% and 90.7±0.1% for 1.92 GeV/c and 1.87 GeV/c, respectively.

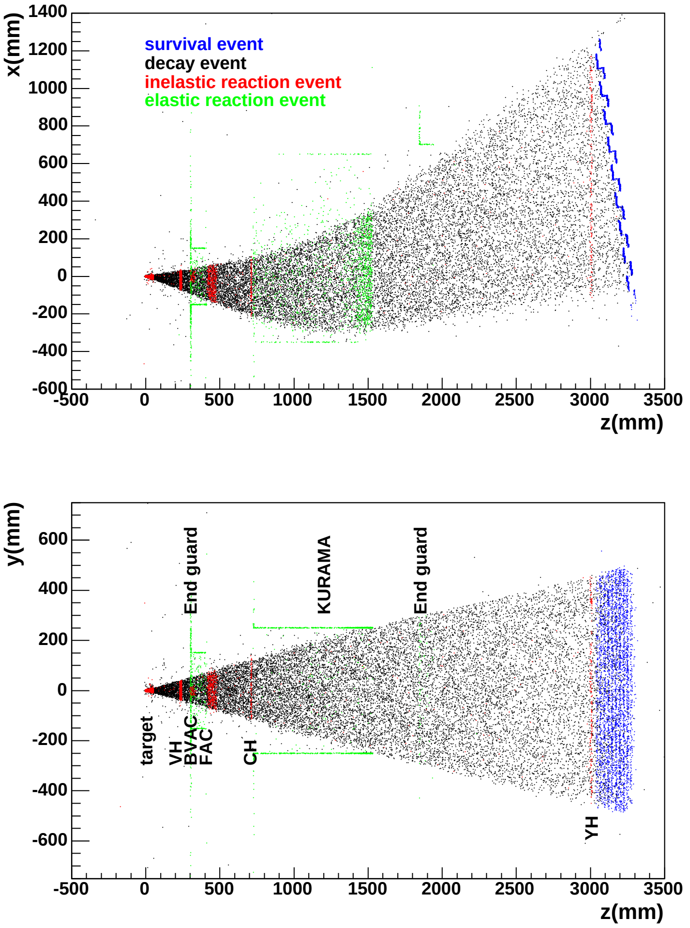

Figure 3.27: Interaction points or decay points of K^-'s obtained by the Monte Carlo simulation based on the GEANT4. The top figure shows the horizontal projection and the bottom one shows the vertical projection. The blue points represent the survival events which arrived at the FTOF without the decay or interaction. The black points are the decay points of K^-'s. The red points indicate the inelastic interaction points. The green points show the events where there were elastic scatterings with the materials and the K^-'s went off from the acceptance and stopped at the end-guard or the yoke of KURAMA.

3.9.7 Efficiency of mass trigger

The coefficient ϵ_{MT} is the efficiency of the second-level mass trigger. In addition to the ordinal data accepted by the mass trigger (data$_{MTon}$) we also took data rejected by the mass trigger (data$_{MToff}$) with the prescale factor of 30. Figures 3.28 (a), (b) show the mass spectra for data$_{MTon}$ and data$_{MToff}$, where K^-'s are also identified in data$_{MToff}$. The efficiency of the mass trigger, ϵ_{MT}, was estimated by the following equation,

$$\epsilon_{MT} = 1 - \frac{30 \times N_{off}}{N_{on} + 30 \times N_{off}}, \tag{3.14}$$

where N_{on} and N_{off} are the number of K^-'s in data$_{MTon}$ and data$_{MToff}$, respectively. Figure 3.28 (c) shows the efficiencies for each momentum region. For all momentum region, the ϵ_{MT} was obtained to be 95.7±0.5% where the error was statistical error. The system error due to the contributions of π^- was estimated to be less than 0.2%.

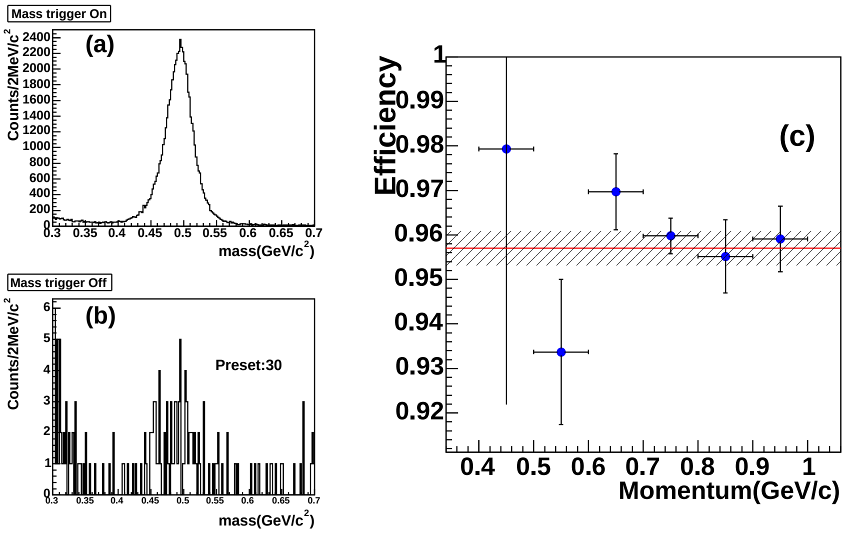

Figure 3.28: (a) Mass spectrum for data$_{MTon}$. (b) Mass spectrum for data$_{MToff}$. (c) Efficiency of the mass trigger. The solid circles represent the efficiencies for each momentum region. The red line is the efficiency obtained for all momentum region and the hatched region shows the error.

3.9.8 Data acquisition efficiency

The data acquisition efficiency (ϵ_{DAQ}), caused by the dead time of the data acquisition system, was obtained as a ratio of the number of the first-level trigger events accepted by the DAQ and that of the first-level trigger requests. The ϵ_{DAQ} was obtained to be 93.5±0.2%.

3.9.9 Acceptance

The effective solid angle of the forward spectrometer was calculated with the Monte Carlo simulation. In the event generator, the distribution of the beam profile defined as a function of (x_b, y_b, u_b, v_b) was produced from the experimental data, where x_b, y_b, u_b and v_b were the horizontal and vertical positions and their derivatives of a beam particle at the target. The outgoing K^-'s were generated uniformly from $\theta - \frac{1}{2}\Delta\theta$ to $\theta + \frac{1}{2}\Delta\theta$ in the polar angle, from 0 to 2π in the azimuthal angle and from $p - \frac{1}{2}\Delta p$ to $p + \frac{1}{2}\Delta p$ in the momentum. In the simulation, the Charge Trigger was also taken into account. The effective solid angle was calculated as a function of scattering angle θ and momentum p as follows,

$$d\Omega(\theta, p) = 2\pi \int_{\theta-\frac{1}{2}\Delta\theta}^{\theta+\frac{1}{2}\Delta\theta} d\cos\theta \times \frac{\text{number of accepted events}}{\text{number of generated events}}. \qquad (3.15)$$

The results are shown in Figure 3.29. Assuming that the Θ^+ was produced isotropically in the center of mass system, the expected momentum distribution has mean momentum of 0.825 GeV/c with momentum spread of 0.040 GeV/c (r.m.s) as shown in Figure 3.30. In order to calculate the differential cross section, we used 0.141±0.004 sr where 0.141 sr was corresponding to the acceptance for momentum of 0.825 GeV/c and the error of 0.004 sr attributed to the momentum spread of 0.040 GeV/c. Similarly, we used 0.133±0.005 sr for 1.87 GeV/c.

When we assume that the Θ^+ was produced isotropically in the center of mass system, 10.4% of the outgoing K^-'s were accepted for the beam momentum of 1.92 GeV/c. Similarly 11.0% of K^-'s were accepted for 1.87 GeV/c. These values were used to derive the total cross section assuming that the Θ^+ was produced in the S-wave.

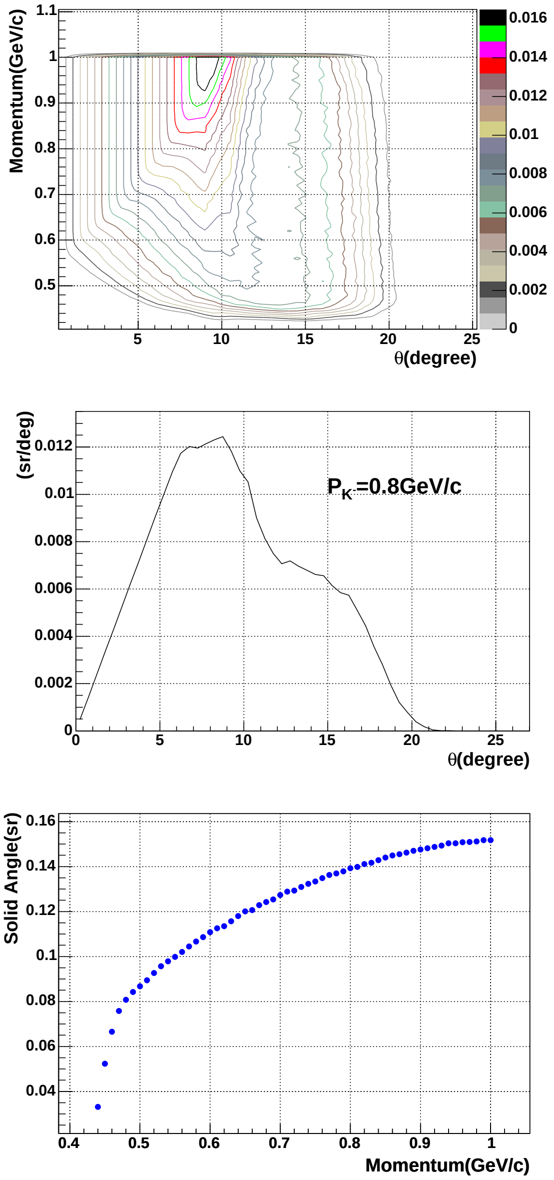

Figure 3.29: Solid angle of the forward spectrometer in the laboratory system. (Top) Contour plot of the solid angle as a function of the scattering angle and the momentum. (Middle) Solid angle at the momentum of 0.8 GeV/c. (Bottom) Solid angle as a function of the momentum. In this plot, the solid angle was integrated in all scattering angle. The solid angle for the momentum of 0.825 GeV/c which is the expected mean momentum of the Θ^+ production at beam momentum of 1.92 GeV/c is 0.141 sr. Similarly that for the momentum of 0.749 GeV/c is 0.133 sr.

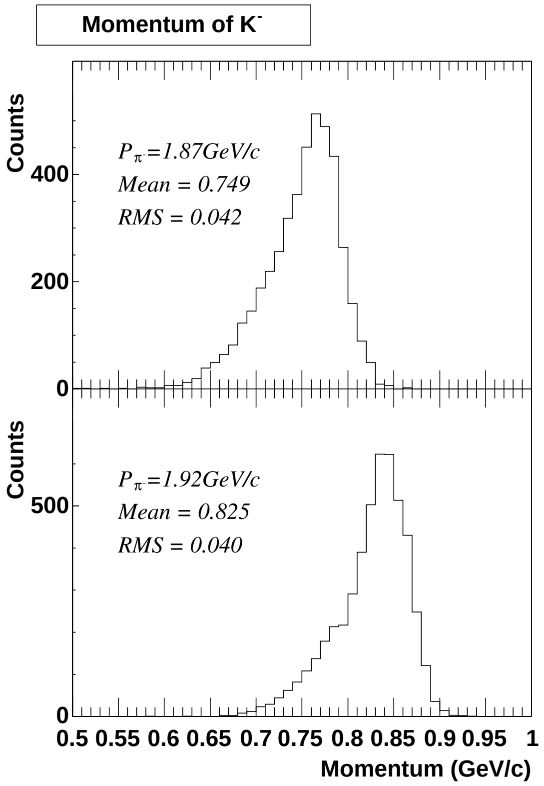

Figure 3.30: Simulated momentum distributions of the K^-'s in the $\pi^- p \rightarrow K^- \Theta^+$ reaction at the beam momenta of 1.87 GeV/c (top) and 1.92 GeV/c (bottom).

Chapter 4

Results

4.1 Missing mass spectra of the $\pi^- p \to K^- X$ reaction

The missing mass spectra for the $\pi^- p \to K^- X$ reaction are shown in Figure 4.1, 4.2 for the beam momenta of 1.87 GeV/c and 1.92 GeV/c. Considering the expected missing mass resolution of 13.4 MeV/c^2 (FWHM), i.e. σ=5.7 MeV/c^2, three spectra with different binnings of 2MeV/c^2, 3MeV/c^2 and 4MeV/c^2 per bin are presented to study the effects which result from the difference of the binning.

In order to display the contribution from carbon nuclei in the SCIFI and polyethylene targets, carbon target data are also shown as the hatched spectra, which are normalized by the number of beam particles and the number of carbon nuclei in each target. The statistics of the carbon target data is about ten times lower than that of the polyethylene target data. The net contribution from free protons is represented as the excess from the hatched histogram and is compatible with the expectation from the cross sections of the $\pi^- p \to K^- X$ reactions measured in the past experiment using a bubble chamber [56]. Because half of data at beam momentum of 1.87 GeV/c was taken with the SCIFI target, the contribution from free protons at 1.87 GeV/c is smaller than that at 1.92 GeV/c. Naively the low missing mass region is corresponding to high momentum of the scattered K^-. When a reaction with a free proton is considered, a momentum, which is so high as to correspond to the missing mass region less than about 1.45 GeV/c^2, is not allowed kinematically. Therefore this missing mass region is attributed to contributions from quasi-free reactions in carbon nuclei. In fact, this missing mass region is represented well by the carbon target data.

In the missing mass spectrum at 1.87 GeV/c, data taken with the SCIFI and the polyethylene targets are combined. Any peak with the width compatible with the experimental resolution has not been observed in this spectrum.

In the missing mass spectrum at 1.92 GeV/c, it seems that there is a bump around 1.53 GeV/c^2 which is consistent with the mass reported by several experiments. However there is a possibility that the structure is only a statistical fluctuation. In the following section, we discuss the bump in this missing mass spectrum.

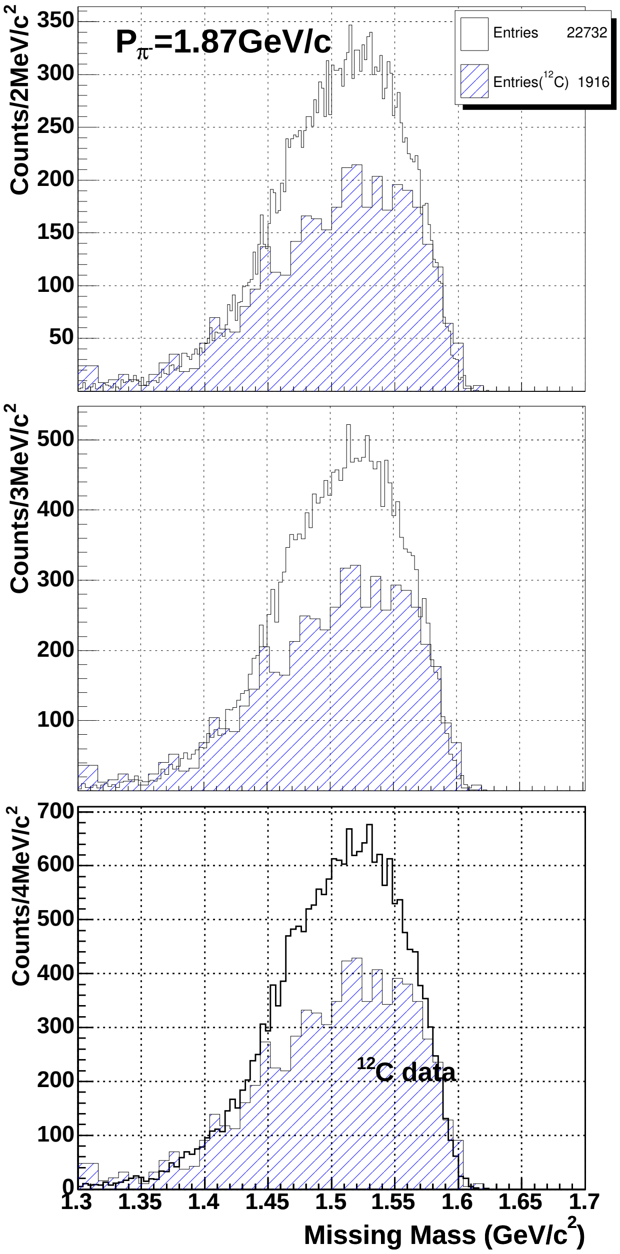

Figure 4.1: Missing mass spectra of the $\pi^- p \to K^- X$ reaction at the beam momentum of 1.87 GeV/c with the different binnings of 2MeV/c^2 (top), 3MeV/c^2 (middle), and 4MeV/c^2 (bottom) per bin. These histograms are the sum of data with the SCIFI target and the polyethylene target. The hatched histograms are the carbon target data which are normalized by the number of target and beam particles. The statistics of the carbon target data is about ten times lower than that of the polyethylene and SCIFI data. These hatched histograms show the contribution from carbon nuclei in the SCIFI and the polyethylene targets.

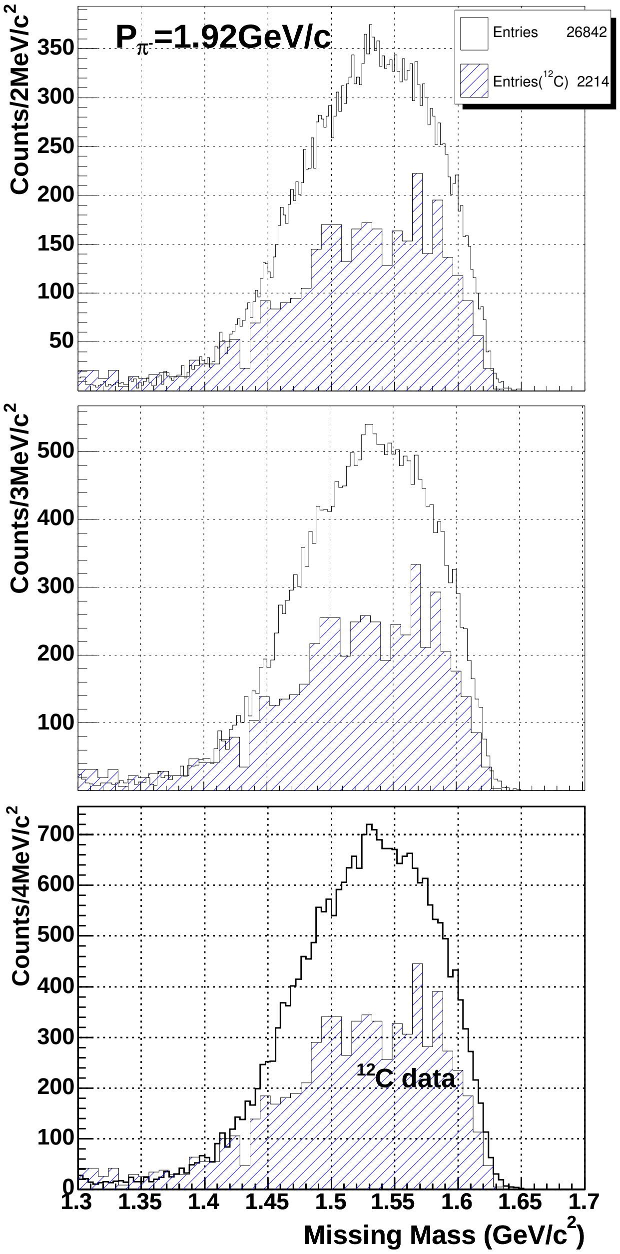

Figure 4.2: Missing mass spectra of the $\pi^- p \rightarrow K^- X$ reaction at the beam momentum of 1.92 GeV/c with the different binnings of 2MeV/c^2 (top), 3MeV/c^2 (middle), and 4MeV/c^2 (bottom) per bin. The hatched histograms are the carbon target data which are normalized by the number of target and beam particles. The statistics of the carbon target data is about ten times lower than that of the polyethylene data. These hatched histograms show the contribution from carbon nuclei in the polyethylene target.

4.2 Discussion about the missing mass spectrum at 1.92 GeV/c

In this section, we discuss whether it is possible to regard the bump in the missing mass spectrum at 1.92 GeV/c as the Θ^+ from the viewpoint of the peak position, the width and the statistical significance.

We fitted this histogram with the background of a cubic function and a Gaussian peak as shown in Figure 4.3 (a). In this fitting, at first, the initial parameters of the background were estimated by fitting with only a cubic function, where the bump region was excluded from the fitting. Then the histogram was fitted with the Gaussian peak and the background function simultaneously. Figure 4.3 (b) shows the residual plot from the background function obtained in the fitting. The peak position has been obtained to be 1530.6 $^{+2.2}_{-1.9}$(stat.)$^{+1.9}_{-1.3}$(syst.) MeV/c^2. The explanation of the systematic error will be described in Section 4.2.1. The obtained value is consistent with the masses reported by the several experiments. The width has been obtained to be Γ=$9.8^{+7.1}_{-3.4}$ MeV/c^2 (FWHM) which is consistent with the expected resolution of 13.4 MeV/c^2 within the error. The count of the peak has been obtained to be 139^{+86}_{-67}(stat.)±10(syst.) by calculating the area of the Gaussian function obtained by fitting the histogram. The uncertainty of count resulting from varying the fitting range and binning is considered as the systematic error. The systematic error of the peak count will be explained in Section 4.2.2.

Because the obtained width is consistent with the experimental resolution, we also fitted this spectrum with the fixed width of 13.4 MeV/c^2 as shown in Figure 4.4. The count of this bump has been obtained to be 183±71(stat.)±10(syst.). The statistical significance of this bump was considered by two expressions. The first expression is the naive estimator $N_s^{2\sigma}/\sqrt{N_s^{2\sigma}+N_b^{2\sigma}}(\cong N_s^{2\sigma}/\sqrt{N_b^{2\sigma}})$ where $N_s^{2\sigma}$ is the peak count within 2σ region from the center and $N_b^{2\sigma}$ is the background within the same region. The significance of 2.7σ is obtained by the first expression. The second estimate of significance is given by $N_s/\sqrt{\Delta N_s}$, where N_s is full area of the Gaussian peak obtained by the fitting of the histogram and ΔN_s is its fully correlated uncertainty. The significance of 2.5σ is obtained by the second expression.

Although we assumed that there was a bump around 1.53 GeV/c^2 in the discussion above, we also fitted the histogram with only the background of a cubic function assuming that there was no peak structure. The fitting result is shown by a dashed line in Figure 4.3 (a). The difference between backgrounds obtained from two fits, the Gaussian peak plus the background and only the background, was represented by the solid line in Figure 4.3 (b). The obtained reduced χ^2 was less than one and the assumption of the non-peak structure could not be excluded. However the reduced χ^2 was dependent on the fitting range and was almost determined by the residuals at the region other than the bump. Therefore we also checked the statistical significance of the bump from this background obtained with the assumption of the non-peak structure The significance is estimated to be 1.9σ using the first expression, $N_s^{2\sigma}/\sqrt{N_s^{2\sigma}+N_b^{2\sigma}}$.

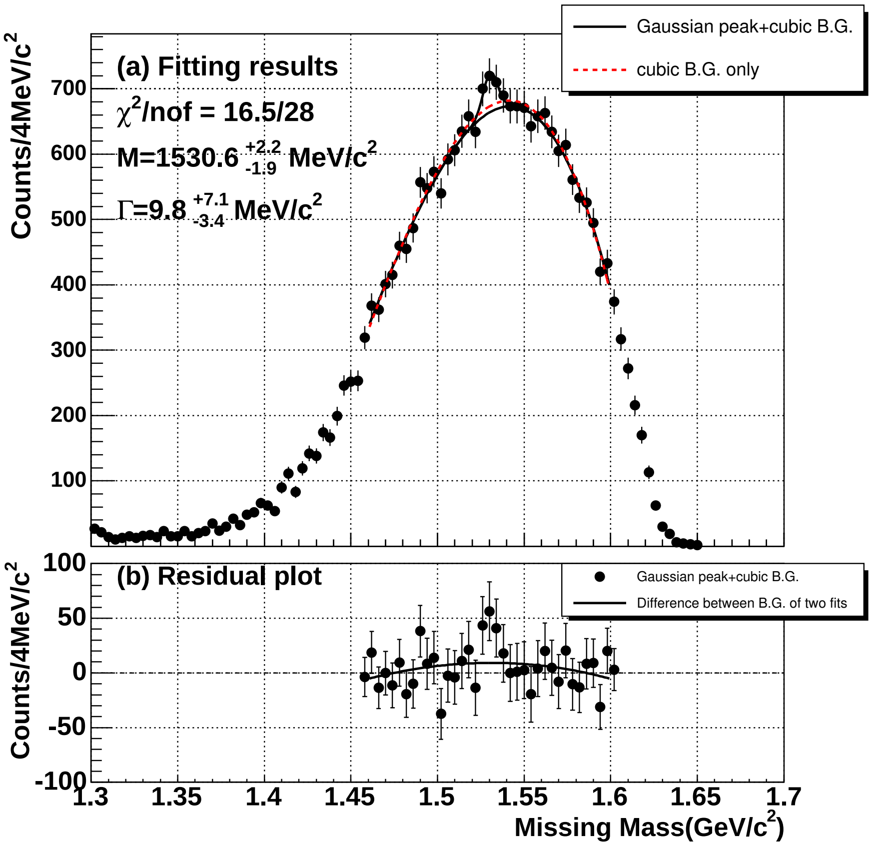

Figure 4.3: Fitting results of the missing mass spectrum of the $\pi^- p \rightarrow K^- X$ reaction at the beam momentum of 1.92 GeV/c. (a) We fitted this spectrum with third order polynomial background and a Gaussian peak (solid line). In this fitting, the width was a parameter and obtained to be $9.8^{+7.1}_{-3.4}$ MeV/c^2 (FWHM) which was consistent with the expected value of 13.4 MeV/c^2 within the error. The dashed line represents the fitting result with only third order polynomial background assuming that there is no peak structure. (b) Residual plot from the background function obtained from the fitting with third order polynomial background and a Gaussian peak. The difference between backgrounds obtained from two fits, the Gaussian peak plus the background and the background only, is represented by the solid line.

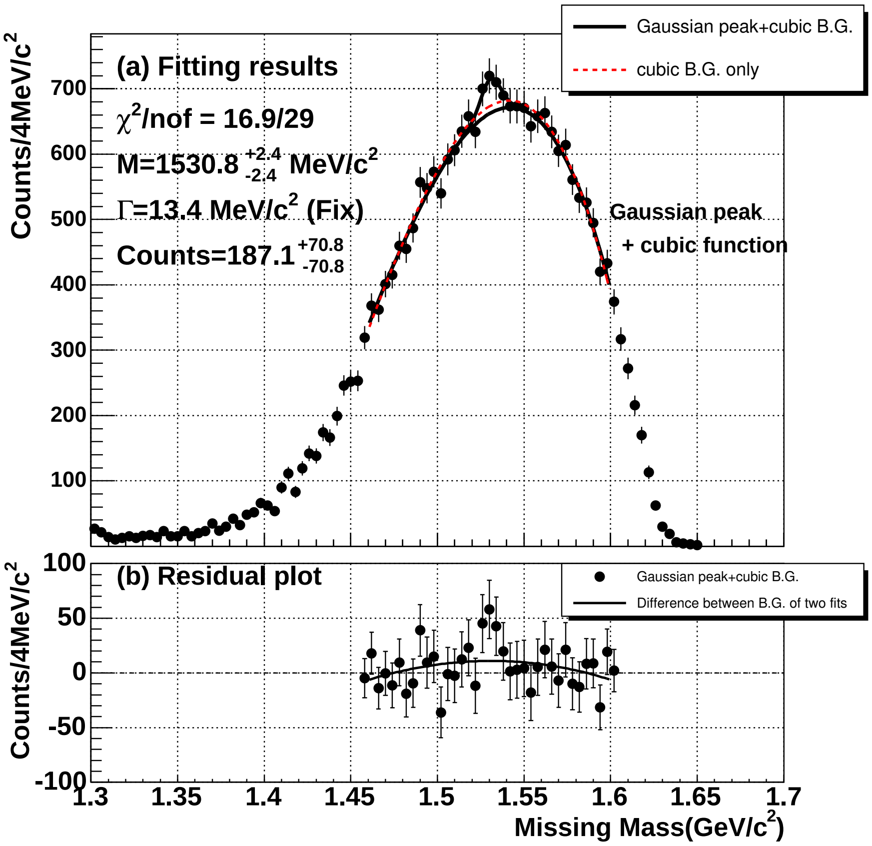

Figure 4.4: (a)Results of fitting the missing mass spectrum of the $\pi^- p \rightarrow K^- X$ reaction at the beam momentum of 1.92 GeV/c with the same function as Figure 4.3. However, in this fitting, the width was a fixed value of the expected resolution of 13.4 MeV/c^2. The solid line represents the fitting result. The dashed line is the same as that in Figure 4.3 and represents the fitting result with only third order polynomial background assuming that there is no peak structure. (b) Residual plot from the background function obtained from the fitting with third order polynomial background and a Gaussian peak. The difference between backgrounds obtained from two fits, the Gaussian peak plus the background and the background only, is represented by the solid line.

4.2.1 Systematic error of the peak position

Missing mass is calculated with the momenta of incident and outgoing particles and the scattering angle as described in Equation (3.12). We estimated the systematic error of the absolute value of the missing mass from the systematic error of these variables.

The momenta of beam particles were calibrated in order that the peak of the Σ^+ obtained in the (π^+, K^+) reaction became consistent with the PDG value. However the statistics of the Σ^+ was not enough. There is an uncertainty due to the statistical error of the determination of the peak position. This uncertainty is corresponding to the uncertainty of the Θ^+ mass of $\Delta M =^{+1.8}_{-0.9}$ MeV/c^2.

For the scattered particles, the important variables are the momentum and the scattering angle to determine the missing mass. We did not take into account the systematic error of the momentum, because the obtained central values of masses of K^- and π^- were consistent with the PDG value. The scattering angle was calculated using the straight track at the entrance of KURAMA, where there was the fringing field and the trajectories of outgoing particles were bent by the fringing field. Therefore the obtained scattering angle has the systematic error due to this effect. We assumed that the systematic error of the missing mass came from only the systematic error of the scattering angle. The systematic error of the scattering angle was estimated from the masses of $\Lambda(1115)$ and $\Lambda(1520)$ obtained from the invariant mass spectra of the π^- and proton system and the K^- and proton system, respectively. The observed mass of $\Lambda(1115)$ was 1113.7±0.4 MeV/c^2 (the PDC value is 1115.683±0.006 MeV/c^2). Assuming that the shift is attributed to the error of the scattering angle, the error of the scattering angle is $\Delta\theta = +0.5$ degree, which is corresponding to the error of the missing mass of $\Delta M = +0.6$ MeV/c^2. The observed mass of $\Lambda(1520)$ was 1520.5±2.6 MeV/c^2 (the PDC value is 1519.53±1.0 MeV/c^2). Similarly, the error of the scattering angle is $\Delta\theta = -0.5$ degree and the error of the missing mass is $\Delta M = -0.9$ MeV/c^2.

Considering the effects of the beam momentum and the scattering angle, we determined that the systematic error of the missing mass is $\Delta M =^{+1.9}_{-1.3}$ MeV/c^2.

4.2.2 Counts of peak

The count of the peak was calculated as the area of the Gaussian function obtained by fitting the missing mass histogram with the Gaussian peak and the polynomial background. The background shape obtained from the fitting is dependent on the fitting range. Therefore the count of the peak also varies with the fitting range. In addition, because the statistics of the histogram is not sufficient, the yield of the peak depends on the binning of the histogram. The uncertainty due to the difference of the fitting range and the binning is treated as the systematic error of the peak count. In order to study the systematic error, we investigated the yield of the peak for the histograms with different binnings of 2 MeV/c^2, 3 MeV/c^2 and 4 MeV/c^2 per bin. The dependence of the fitting range was checked by fitting with five different fitting ranges, where the fitting range was incremented by 10 MeV/c^2 for both sides from the closest fitting range between 1.49 GeV/c^2 and 1.57 GeV/c^2. The maximum value of the upper side of the fitting range was set to 1.6 GeV/c^2. Figures 4.5 and 4.6 show the dependences of the reduced χ^2 , the count of the peak and the statistical significance for the different binnings and fitting ranges. Figure 4.5 is the result for the fitting with the width as a parameter. Figure 4.6 is the result for the fitting with the fixed width. From the reduced χ^2, as shown in (a) of these figures, the fittings are considered to be reasonable for all fitting ranges. The result for the count of the peak is shown in (b) of these figures, where the error bars represent the statistical error. The final value and the systematic error of the yield were obtained as the mean value and the standard deviation of the counts, as shown by the red line and the hatched region in (b) of these figures, respectively. In case of the fit with the width as a parameter, the peak count is 138^{+86}_{-67}(stat.) ± 10(syst.). In case of the fit with the fixed width, similarly, the peak count is 183 ± 71(stat.) ± 10(syst.). The (c) of these figures show the dependences of the statistical significance where the statistical significance is considered by the two expression of $N_s^{2\sigma}/\sqrt{N_s^{2\sigma}+N_b^{2\sigma}}$ and $N_s/\sqrt{\Delta N_s}$ as described in page 86. When the standard deviation of the distribution is considered as the error of the significance, the significances for the fitting with the width as a parameter have been obtained to be 2.5±0.1 σ for the first expression and 2.0±0.2 σ for the second expression. For the fitting with the fixed width, similarly, the significances have been obtained to be 2.7±0.1 σ and 2.5±0.1 σ, respectively.

4.2.3 Summary

The obtained results are summarized by following,

$$\begin{aligned}\text{Mass} &: 1530.6^{+2.2}_{-1.9}(\text{stat.})^{+1.9}_{-1.3}(\text{syst.})\ \ \text{MeV}/c^2,\\ \text{Width} &: 9.8^{+7.1}_{-3.4}\ \text{MeV}/c^2.\end{aligned}$$

The obtained mass is consistent with ones reported by several experiments which claimed the evidence of the Θ^+. The width is consistent with the experimental resolution. This fact is also similar with other experiments. From the result of the fitting with the fixed width, the yield and the significance are

$$\begin{aligned}\text{Yield} &: 183 \pm 71(\text{stat.}) \pm 10(\text{syst.}),\\ \text{Significance} &: 2.5 \sim 2.7\ \sigma.\end{aligned}$$

The statistical significance is not sufficient to claim this bump as the evidence of the Θ^+. However it is quite important to estimate the upper limit of the production cross section of the Θ^+ via the $\pi^- p \rightarrow K^- \Theta^+$ reaction. Therefore we have obtained the upper limit of the production cross section. To derive the upper limit, the peak count obtained from the fitting with the fixed width is used at beam momentum of 1.92 GeV/c. We used a single tail approach assuming that the peak count fluctuates based on Gaussian statistics. Then the upper limit of the peak count is $N_s + 1.28 \times \sqrt{\Delta N_{stat.}^2 + \Delta N_{syst.}^2}$=274 at 90% confidence level, where N_s denotes the peak count obtained from the fitting and $\Delta N_{stat.}$, $\Delta N_{syst.}$ denote the statistical and systematic errors respectively, and we use this count for the following calculations.

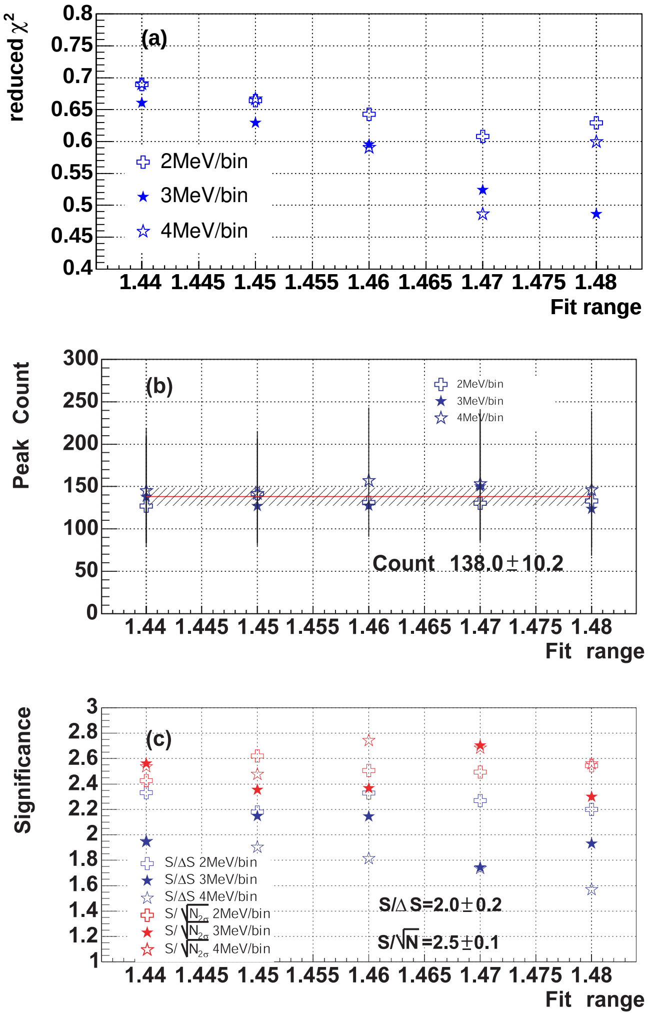

Figure 4.5: Study of the systematic error due to the difference of the fitting range and the binning for the fitting with the width as a parameter. In all plots, the open cross, solid star and open star represent the results for the histogram with binning of 2 MeV/c^2, 3 MeV/c^2 and 4 MeV/c^2, respectively. The x axis is the lower side of the fitting range. (a) The χ^2 distribution of the fitting with the Gaussian peak and polynomial background for each binning and fitting range. (b) Count of the peak distribution for each binning and fitting range. The error bars represent the statistical errors. The red line is the mean value of the count which is 138.0 and the hatched region represents the standard deviation of this distribution which is treated as the systematic error. (c) Dependence of the statistical significance. The red points represent the significances calculated by the first expression of $N_s^{2\sigma}/\sqrt{N_s^{2\sigma}+N_b^{2\sigma}}$. The blue points represent the significances calculated by the second expression of $N_s/\sqrt{\Delta N_s}$. The mean values and the standard deviations of these distributions are obtained to be 2.5±0.1σ and 2.0±0.2σ for the first and second expressions, respectively.

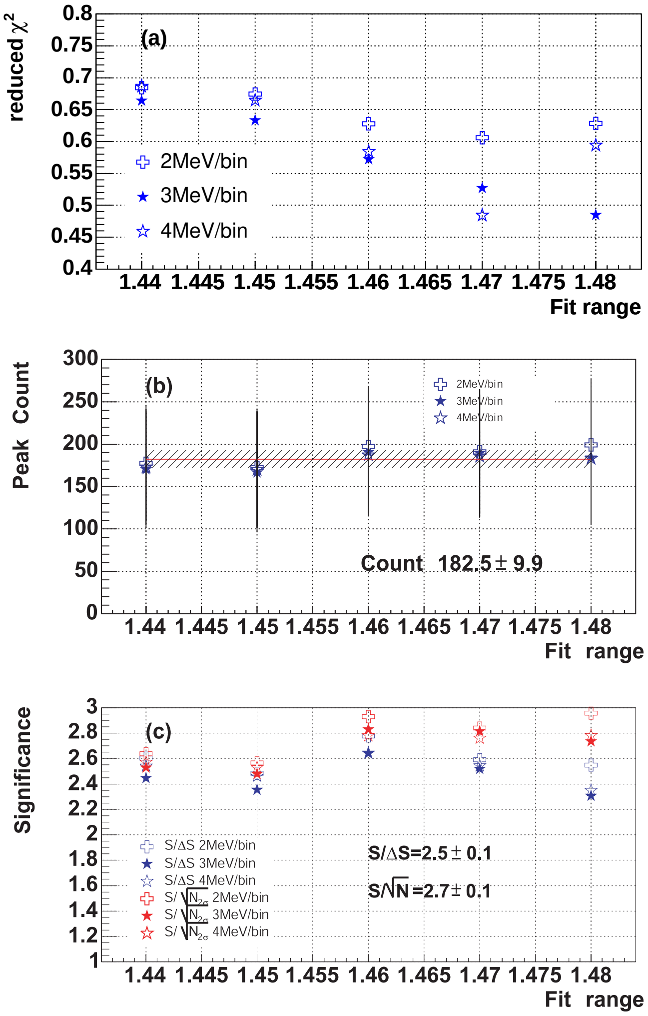

Figure 4.6: Study of the systematic error due to the difference of the fitting range and the binning for the fitting with the fixed width. In all plots, the open cross, solid star and open star represent the results for the histogram with binning of 2 MeV/c^2, 3 MeV/c^2 and 4 MeV/c^2, respectively. The x axis is the lower side of the fitting range. (a) The χ^2 distribution of the fitting with the Gaussian peak and polynomial background for each binning and fitting range. (b) Count of the peak distribution for each binning and fitting range. The error bars represent the statistical errors. The red line is the mean value of the count which is 182.5 and the hatched region represents the standard deviation of this distribution which is treated as the systematic error. (c) Dependence of the statistical significance. The red points represent the significances calculated by the first expression of $N_s^{2\sigma}/\sqrt{N_s^{2\sigma}+N_b^{2\sigma}}$. The blue points represent the significances calculated by the second expression of $N_s/\sqrt{\Delta N_s}$. The mean values and the standard deviations of these distributions are obtained to be $2.7\pm0.1\sigma$ and $2.5\pm0.2\sigma$ for the first and second expressions, respectively.

4.3 The upper limit of production cross section of the $\pi^- p \rightarrow K^- X$ reaction

In order to derive the upper limit of the cross section, we used the equation (3.13) as described in Section 3.9. The efficiencies listed in Table 3.2 were used. Scattering angles of outgoing particles at the laboratory system range from 0 degree to 20 degree and the mean value of the scattering angle is 8.2 degree. The differential cross section in the laboratory system is derived in this scattering angle range.

4.3.1 At beam momentum of 1.92GeV/c

For the derivation of the upper limit, the count of the peak obtained by the fitting with the fixed width was used. The numbers of beam particles and protons in the target are $N_{beam} = 7.40 \times 10^9$ and $N_{target} = 8.6 \times 10^{23}$, respectively.

The upper limit of the differential cross section via the $\pi^- p \rightarrow K^- \Theta^+$ reaction at the beam momentum of 1.92 GeV/c has been obtained to be

$$\frac{d\sigma}{d\Omega_{\mathrm{L}}} < 2.9 \ \mu\mathrm{b/sr} \ \ (90\% \ \ \mathrm{confidence} \ \ \mathrm{level})$$

at 90% confidence level. Assuming that K^- is produced isotropically in the center of mass system, 10.4% of K^- is accepted by the spectrometer. Therefore, if the K^- is produced in the S-wave, the upper limit of the total cross section has been obtained to be

$$\sigma < 3.9 \ \mu\mathrm{b} \ \ (90\% \ \ \mathrm{confidence} \ \ \mathrm{level})$$

at 90% confidence level.

4.3.2 At beam momentum of 1.87GeV/c

We obtained the upper limit of the cross section from the 1.87 GeV/c data as well as 1.92 GeV/c data. Because we used two different targets, we derived the upper limit for each target.

In the missing mass spectrum at 1.87 GeV/c, we could not find any obvious peak structure. We estimated that the signal from the Θ^+ (N_{Θ^+}) is less than $1.28\times\sqrt{N_{2\sigma}}$ at 90 % confidence level, where $N_{2\sigma}$ represents the count in the missing mass spectrum corresponding to $\pm 2\sigma$ region from the peak position (1530.6 MeV/c^2) obtained from 1.92 GeV/c data. We calculated that N_{Θ^+} were 62 and 52 for the SCIFI target and the polyethylene target, respectively.

SCIFI target

The numbers of beam particles and protons in the target are $N_{beam} = 2.88 \times 10^9$ and $N_{target} = 9.53 \times 10^{23}$, respectively. From the SCIFI target data, the upper limit of the differential cross section via $\pi^- p \rightarrow K^- \Theta^+$ reaction at the beam momentum of 1.87 GeV/c has been obtained to be

$$\frac{d\sigma}{d\Omega_{\mathrm{L}}} < 1.7 \ \mu\mathrm{b/sr} \ \ (90\% \ \ \mathrm{confidence} \ \ \mathrm{level})$$

at 90% confidence level. Assuming that the Θ^+ is produced isotropically in the center of mass system, the upper limit of the total cross section has been obtained to be

$$\sigma < 2.1 \ \mu\mathrm{b} \ \ (90\% \ \ \mathrm{confidence} \ \ \mathrm{level})$$

at 90% confidence level.

Polyethylene target

The numbers of beam particles and protons in the target are $N_{beam} = 2.97 \times 10^9$ and $N_{target} = 8.56 \times 10^{23}$, respectively. From the polyethylene target data, the upper limit of the differential cross section at the beam momentum of 1.87 GeV/c has been obtained to be

$$\frac{d\sigma}{d\Omega_{\rm L}} < 1.6\ \mu\text{b/sr} \quad (90\% \quad \text{confidence} \quad \text{level})$$

at 90% confidence level. The upper limit of the total cross section has been obtained to be

$$\sigma < 1.8\ \mu\text{b} \quad (90\% \quad \text{confidence} \quad \text{level})$$

at 90% confidence level.

4.3.3 Summary

The obtained upper limits of cross sections and differential cross sections are summarized in Figure 4.7 as a function of beam momentum. At the beam momentum of 1.87 GeV/c, the results from the two targets are consistent each other.

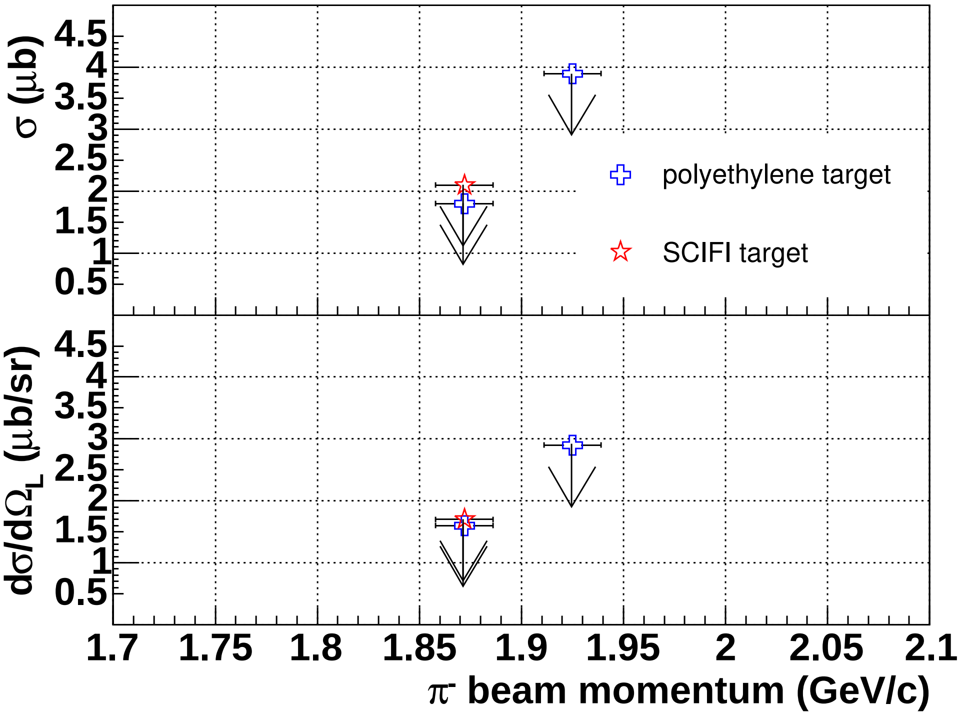

Figure 4.7: Upper limits of the total and differential cross sections of the $\pi^- p \to K^- \Theta^+$ reaction. For the derivation of the total cross section, we assume that the Θ^+ is produced isotropically in the center of mass system. The differential cross section is derived in the scattering angle from 0 to 20 degree at the laboratory frame.

In the above discussion, we have derived the upper limit for the mass region of the obtained peak position (1530.6 MeV/c^2). However, the mass of the Θ^+ has not been determined demonstrably, because there are some differences between the masses reported by several collaborations which claim the evidence of the Θ^+. The significance for the peak observed in the present experiment is insufficient as the evidence of the Θ^+. Therefore we have derived the 90 % confidence level upper limits of the total and differential cross sections as a function of the mass of the Θ^+. Because the momentum of the outgoing K^- is related to the mass of the Θ^+, the decay factor (f_{decay}), the K^- interaction factor (f_{K-int}) and the acceptance ($d\Omega$) were obtained for each mass of the Θ^+. Figures 4.8 and 4.9 show the obtained upper limits for the beam momenta of 1.87 GeV/c and 1.92 GeV/c.

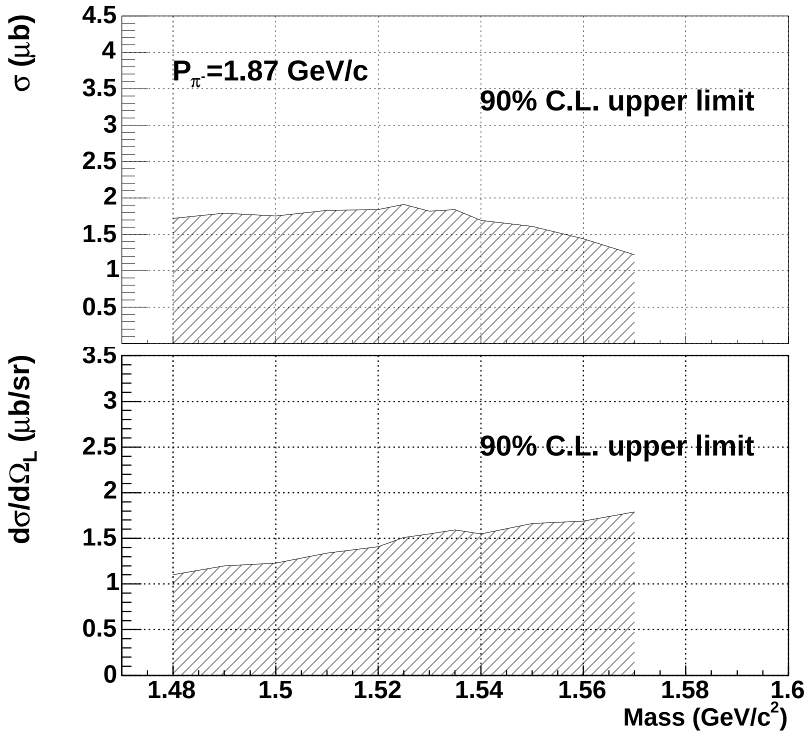

Figure 4.8: Upper limits of the total and differential cross sections of the $\pi^- p \to K^- \Theta^+$ reaction as a function of the mass of the Θ^+ for the beam momentum of 1.87 GeV/c. This is the result obtained from the polyethylene target data.

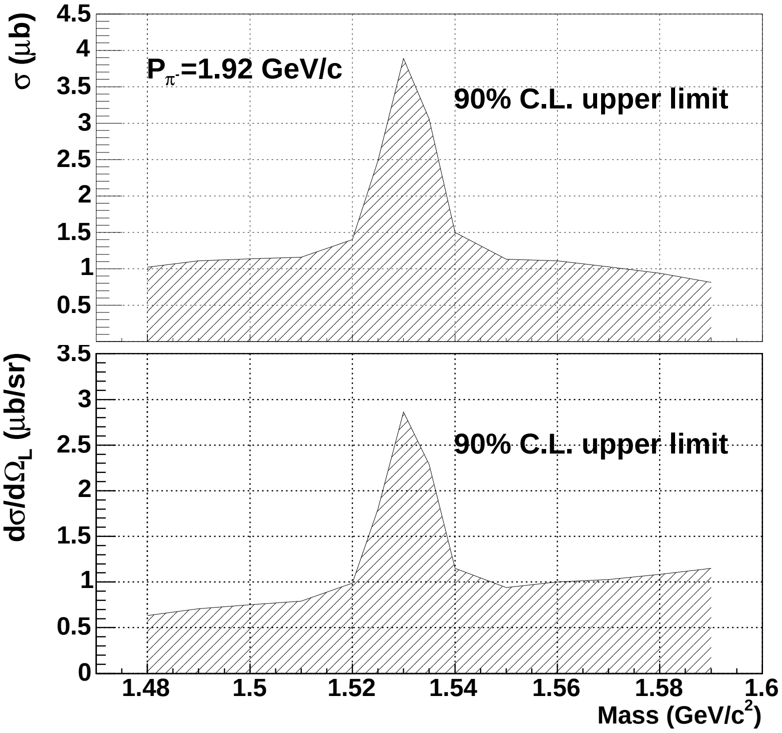

Figure 4.9: Upper limits of the total and differential cross sections of the $\pi^- p \rightarrow K^- \Theta^+$ reaction as a function of the mass of the Θ^+ for the beam momentum of 1.92 GeV/c.

Chapter 5

Discussion

5.1 Comparison with theoretical calculations

Once the existence of the Θ^+ is established, its production mechanism will become quite important issue. Here we compare our experimental results with theoretical calculations.

The theoretical calculations of the production cross section via $\pi^- p \to K^- \Theta^+$ reaction have been done by W. Liu and C. M. Ko [57] and Y. Oh et al. [58]. They calculated the production cross section taking into account the Feynman diagrams shown in Figure 1.12, where nucleon resonance or K^{0*} was exchanged. Unknown parameters such as the coupling constant $g_{K^* N\Theta}$ and the cut off parameter Λ of the form factor were used in their calculations. In their calculation, they used the same form factor, which is a function of $\sqrt{s}$ only,

$$F(s) = \frac{\Lambda^2}{\Lambda^2 + \mathbf{q}_i^2}, \tag{5.1}$$

where Λ is the cut off parameter and $\mathbf{q}_i$ is the three-momentum of the initial state particles in the center of mass frame. They used the cut off parameter of $\Lambda = 0.5$ GeV basing on fitting the measured cross section for the reaction $\pi N \to K\Lambda$ using similar hadronic Lagrangians [63].

In Reference [57], Liu and Ko calculated the cross section taking into account only the s-channel diagram. They used $g_{KN\Theta} = 4.4$, which corresponds to 20 MeV/c^2 width of the Θ^+. They predict that the cross section is about 50 μb. In their formalism, the cross section is controlled by the $g_{KN\Theta}$, because they took into account the only s-channel diagram. The cross section is proportional to the width, since both the cross section and the width are proportional to $g^2_{KN\Theta}$. If parameters other than $g_{KN\Theta}$ are correct, the present experimental results mean that the width of the Θ^+ is less than 1.6 MeV/c^2.

Y. Oh *et al.* calculated the cross section taking into account the s-channel diagram and t-channel diagram where the K^* is exchanged. They used $g_{KN\Theta}$=2.2, which corresponds to 5 MeV/c^2 width of the Θ^+, and the same cutoff value used by C. M. Ko et al.. Because there is no information about $g_{K^* N\Theta}$, they used several values from -2.2 to 2.2 as $g_{K^* N\Theta}$. They point out that the behavior of the cross section of the $\pi^- p \to K^- \Theta^+$ reaction is quite dependent on the magnitude of $g_{K^* N\Theta}$ as shown in Figure 5.1. The calculated cross section ranges from about 2 μb to 190 μb. Therefore this reaction is suitable to give a guide to estimate the magnitude of $g_{K^* N\Theta}$. Present results are quite smaller than most of the theoretical calculations as shown in Figure 5.1. If the parameters other than $g_{K^* N\Theta}$ are correct, the calculations other than using $g_{K^* N\Theta} = 2.2$ are excluded by the present results.

Currently, although we do not know the correct values of $g_{KN\Theta}$, $g_{K^* N\Theta}$ and which kind of form factor is realistic, the present results give a strong constraint to these unknown parameters.

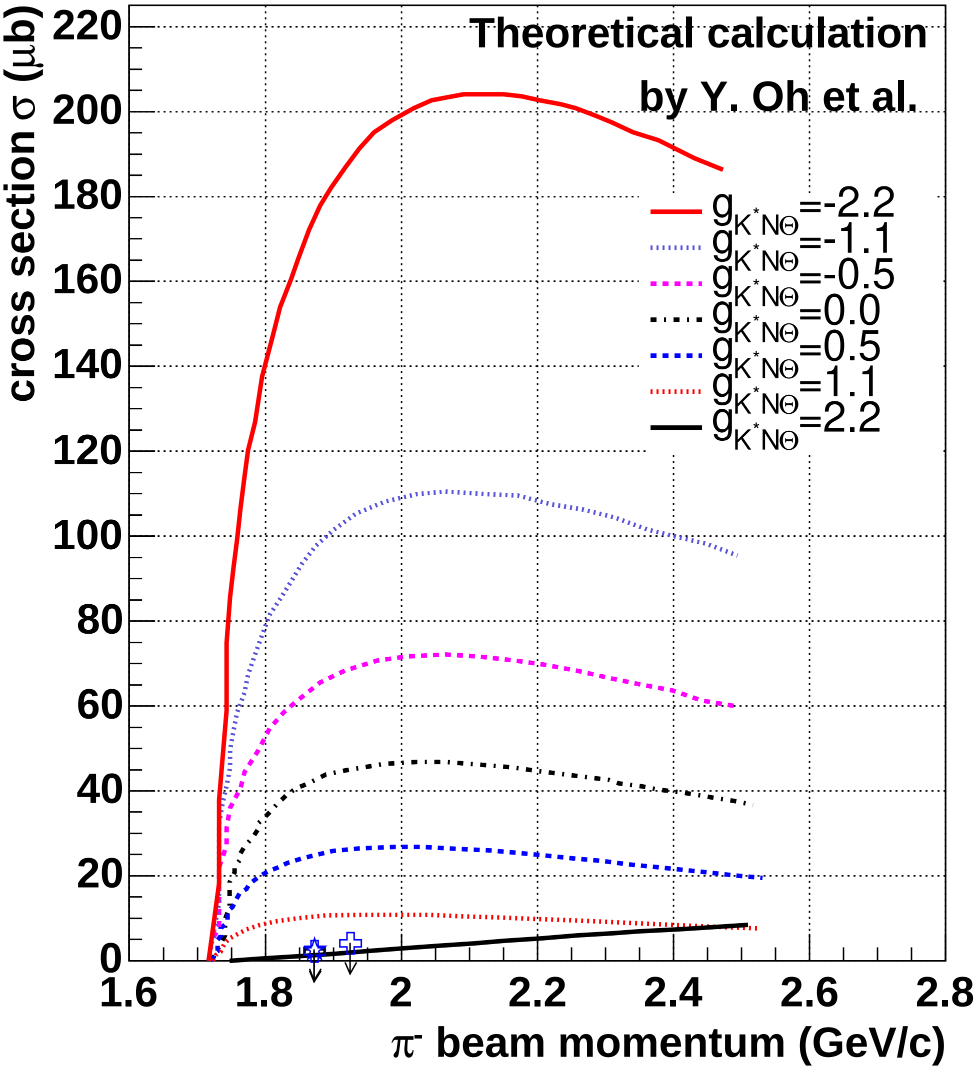

Figure 5.1: Comparison with the experimental 90% C.L. upper limits of the production cross section of $\pi^- p \to K^- \Theta^+$ reaction and theoretical calculations by Y. Oh *et al.* [58]. They calculated the total cross section for $J^P = 1/2^+$ using $g_{KN\Theta}$=2.2 and several values as $g_{K^*N\Theta}$ from -2.2 to 2.2.

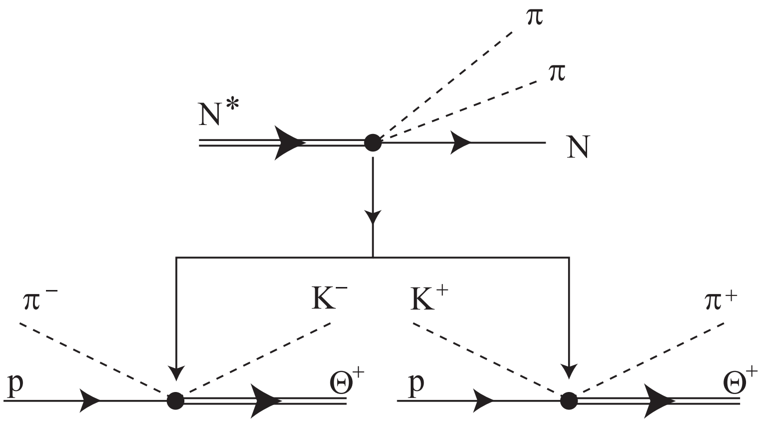

Figure 5.2: Feynman diagram for the three-body decay of the N^* resonance and Feynman diagrams with two-meson coupling for the π^- and K^+ induced reactions for the Θ^+ production. In the calculation by T. Hyodo and A. Hosaka [74], the coupling constants of $\Theta K\pi N$ are estimated from that of $N^*\pi\pi N$ calculated from the decay width of $N^* \to N\pi\pi$.

5.2 Relation between the cross sections via π^- and K^+ induced reactions

A theoretical study of production mechanism via hadronic reactions has been done by T. Hyodo and A. Hosaka [74]. Figure 5.3 shows the obtained upper limit of the cross section for each π^- beam momentum together with their theoretical calculations. They took particular note of the importance of two meson coupling and calculated the total cross sections of the reaction $\pi^-p \to K^-\Theta^+$ and $K^+p \to \pi^+\Theta^+$ in case of $J^P = 1/2^+$ and $3/2^-$ taking into account Feynman diagrams shown in Figure 5.2. They obtained the scalar and vector coupling constants of $\Theta K\pi N$, g^s and g^v, using the flavor SU(3) symmetry from the decay width of $N^*(1710) \to \pi\pi N$. Without the two meson coupling, all the amplitudes for the Θ^+ production are proportional to the $g_{KN\Theta}$ coupling, which is fixed by the small decay width of the Θ^+ as was done in the calculation by W. Liu and C.M. Ko. However, even with the extremely narrow width of the Θ^+, sizable cross section can be obtained with the two meson coupling determined from the decay width of $N^*(1710)$. The obtained coupling constants have uncertainty due to the experimental uncertainties of the branching ratio. They restricted the coupling constants to be consistent with our present results for the dotted, dot-dashed and dashed lines in Figure 4.7. Moreover the relative phase between scalar and vector coupling constants could not be determined by the information of decay width of $N^*(1710)$. This relative phase is quite important because it affects the interference term of two amplitudes. If g_s and g_v have the same phase, the two amplitudes interfere constructively for $\pi^-p \to K^-\Theta^+$ channel, while in $K^+p \to \pi^+\Theta^+$ case it shows the destructive interference. On the other hand, if g_s and g_v do not have the same phase, the constructive and destructive interference appears in opposite way. Considering the small cross section obtained in the present experiment, they selected the latter case. Therefore the behavior near the threshold in this calculation is different from that by Y. Oh *et al.* due to the destructive interference between scalar and vector amplitudes.

The ratio of cross sections of π^- and K^+ induced reactions can be calculated more reliably than the absolute value of the cross section, because there is uncertainty due to selection of a form factor in the derivation of the absolute value. By using the coupling constant which explains the present data, they find that the ratio is very different for

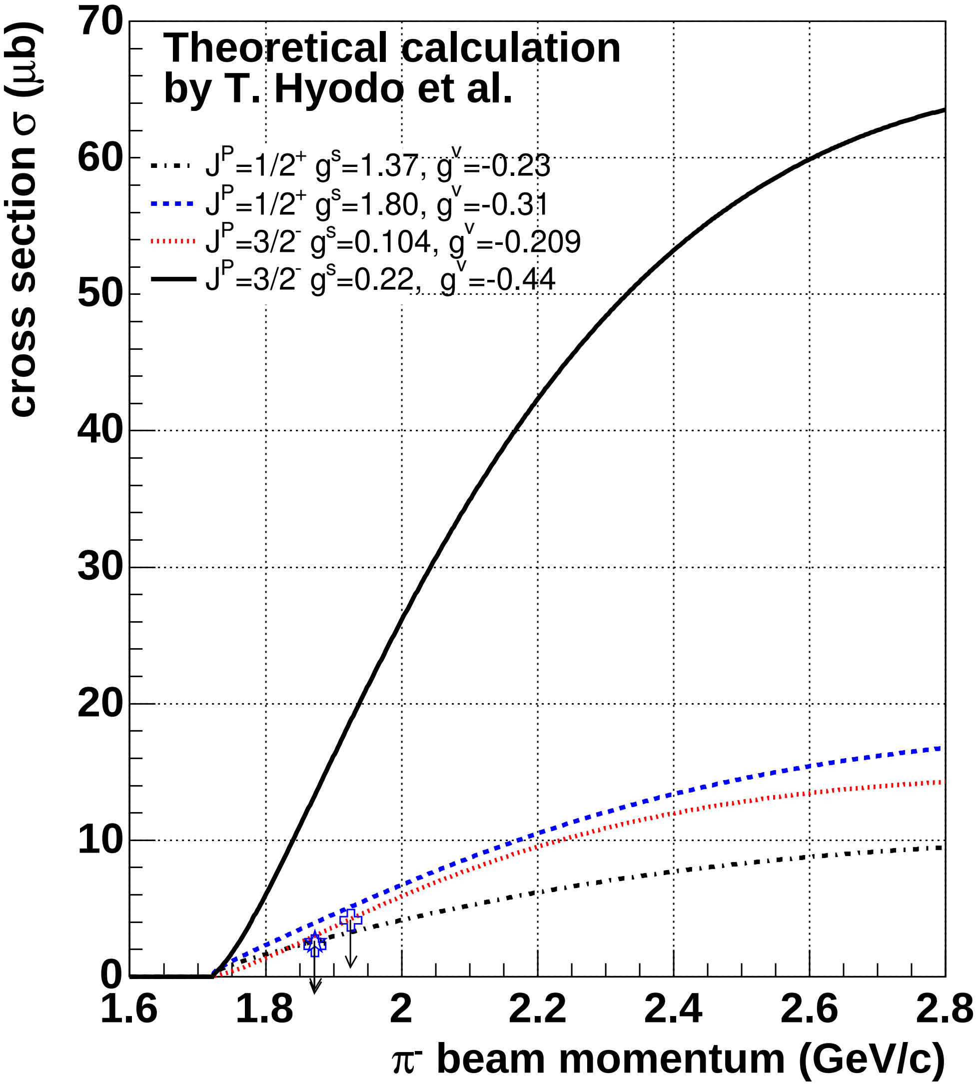

Figure 5.3: The upper limits of the production cross section of $\pi^- p \to K^- \Theta^+$ reaction at beam momenta of 1.87 and 1.92GeV/c. The theoretical calculations by T. Hyodo and A. Hosaka [74] are also shown together. They calculated the total cross section for $J^P = 1/2^+$ and $3/2^-$ using scalar and vector meson coupling constants, g^s and g^v, respectively. The dot-dashed and dashed lines are calculations for $J^P = 1/2^+$ with $(g^s, g^v) = (1.37, -0.23)$ and $(1.80, -0.31)$ respectively. The dotted and solid lines are calculations for $J^P = 3/2^-$ with $(g^s, g^v) = (0.104, -0.209)$ and $(0.22, -0.44)$ respectively.

two J^P assignments. In the case of $J^P = 1/2^+$ the ratio of the cross section, $\sigma(K^+ p \to \pi^+ \Theta^+)/\sigma(\pi^- p \to K^- \Theta^+)$, is $\sim$ 50, while in the case of $J^P = 3/2^-$ it is $\sim$ 3.3. An experiment to search for the Θ^+ via $K^+ p \to \pi^+ \Theta^+$ has been performed at the K6 beam line with high statistics and good missing mass resolution using the SKS spectrometer at KEK (KEK-PS E559) (see Appendix B for the detailed description). One of the most important purposes is the determination of the width utilizing the spectrometer system with the excellent missing mass resolution of 2.4 MeV/c^2 (FWHM), if we observe the Θ^+. In this experiment, about 25,000 events for the $K^+p \rightarrow \pi^+X$ reaction have been collected. The expected sensitivity is less than 10 μb. This experiment together with the present results will provide deeper understanding on the existence of the Θ^+.

Chapter 6

Conclusion

Since the report on the evidence of the exotic baryon Θ^+, many studies from both theoretical and experimental aspects have been conducted. The Θ^+ is predicted by Diakonov *et al.* using chiral soliton model and is considered to be manifestly exotic baryon which has unusual quark contents of $uudd\bar{s}$. The observation at SPring-8/LEPS was immediately confirmed by several experiments. Recently, however, null results have been reported from several high-energy experiments where investigators searched for the Θ^+ using higher statistics. In such a situation, the confirmation of the existence (or non-existence) of the Θ^+ is urgent and crucially important. Therefore high statistics experiments at low energy region with hadronic reaction become crucial.

The present experiment has been carried out to search for the Θ^+ via $\pi^- p \to K^- X$ reaction at the K2 beam line of the KEK Proton Synchrotron (KEK-PS E522). We used π^- beams of 1.87 and 1.92 GeV/c. A SCIFI target was exposed to 2.9×10^9 π^-'s with momentum of 1.87 GeV/c. For the search for the Θ^+, a polyethylene target was mainly used to enhance the contribution from free protons and was exposed to 3.0×10^9 π^-'s of 1.87 GeV/c and 7.4×10^9 π^-'s of 1.92 GeV/c. The analysis was done carefully paying attention to the resolution of the spectrometer, since the Θ^+ is expected to be narrow. The missing mass resolution for the Θ^+ is estimated to be 13.4 MeV/c^2 (FWHM) from the Monte Carlo simulation. The cut positions to select good (π^-, K^-) events were also determined by clear criteria. In the missing mass of the $\pi^- p \to K^- X$ reaction at 1.87 GeV/c, any structure corresponding to the Θ^+ has not been observed. In the missing mass at 1.92 GeV/c, a bump with a width consistent with the experimental resolution has been found at the mass of $M = 1530.6^{+2.2}_{-1.9}(\text{stat.})^{+1.9}_{-1.3}(\text{syst.})$ MeV/c^2. However the statistical significance of the bump is only 2.5$\sim$2.7σ which is not sufficient to claim the evidence of the Θ^+. Therefore we have derived the upper limit of the production cross section via $\pi^- p \to K^- \Theta^+$ reaction. The upper limit of the differential cross sections for the scattering angle from 0 degree to 20 degree at the laboratory frame have been obtained to be 1.6 μb/sr and 2.9 μb/sr at the 90 % confidence level at the beam momenta of 1.87 and 1.92 GeV/c, respectively. The upper limits of the total cross sections have been obtained to be 1.8 μb and 3.9 μb at 1.87 and 1.92 GeV/c, respectively, assuming that the Θ^+ is produced isotropically in the center of mass system.

The obtained upper limits are quite smaller than the theoretical calculations and give a strong constraint to the unknown parameters such as the coupling constant $g_{K^* N \Theta}$ used in the calculations. Using the present results, the cross section of the $K^+ p \to \pi^+ \Theta^+$ reaction has been studied by T. Hyodo and A. Hosaka. They find that the ratio of the cross sections of π^- and K^+ induced reactions are quite different for two J^P assignments of the Θ^+. In the case of $J^P = 1/2^+$, $\sigma(K^+ p \to \pi^+ \Theta^+)/\sigma(\pi^- p \to K^- \Theta^+)$ is $\sim$50, while in the case of $J^P = 3/2^-$ it is $\sim$3.3. An experiment to search for the Θ^+ via $K^+ p \to \pi^+ X$

reaction has been performed at KEK. This experiment together with the present results will provide deeper understanding on the existence of the Θ^+.

Acknowledgments

During my research at graduate school, fortunately I have been given chances to join many experiments; LEPS, KEK-PS E325, E509, E518, E521, E522, E559, E566. These were quite invaluable opportunity not only to learn various experiences for experiments but also to be acquainted with many people. I have spent a long time with them and been supported by them with their collaboration, advice and encouragement. I deeply appreciate kindness and warm advice of all who have helped me until completion of this thesis work.

First of all, I would like to express my sincere gratitude to Prof. Ken'ichi Imai, who has been my supervisor. He guided me to an exciting world of the experimental hadronic and nuclear physics. He gave me so many chances to join experiments which are my irreplaceable asset. He always encouraged me with his warm advice and vivid sense for physics when I had a trouble in the experiment and data analysis. I have also learned from him about attitudes to the physical research as a physicist.

I have spent my graduate school days as a member of the "Experimental Nuclear and Hadronic Physics (NH)" group in Kyoto University. I would like to acknowledge Prof. Naohito Saito for his advice and encouragement. I am very impressed by his leadership not only to physics discussion but also to the management of our laboratory. It is my great pleasure to complete my thesis work before his movement to the KEK. I would like to express my thanks to Prof. Haruhiko Funahashi for his guidance from early days when I was the fourth grade of the undergraduate school. I wish to acknowledge the help and encouragement by Prof. Harutaka Sakaguchi, Prof. Masanobu Nakamura, Prof. Masaru Yosoi and Dr. Tetsuya Murakami and all members of NH group. The NH group has been a hospitable place for me.

I have joined two experiment to search for the Θ^+, KEK-PS E522 and E559, during my doctoral course. I would address my thanks to all the members of KEK-PS E522 and E559 collaboration. I could not complete this thesis work without their great effort. I would like to express great thanks to Prof. Jung-Keun Ahn and Mr. Choong-Jae Yoon. The E522 experiment was impossible without their great effort of design and preparation of the experiment. I am grateful to Mr. Yoon for his contribution for setting up and management of the experiment. I am also grateful to Prof. Ahn for useful discussion on the analysis. I wish to thank to Dr. Hitoshi Takahashi for his kindness during my long stay at KEK. I learned from him many things about experimental and analysis technique. He also brought me to the restaurant out side of KEK at every week end, which released my stress and anxiety caused by the long preparation and long beamtime. I would like to express my thanks to Prof. Kazuma Nakazawa for his continuous collaboration for both experiments. He came to the experimental area as much as possible and encouraged me during the long beam time. I would like to express my thanks to Dr. Kazuhiro Yamamoto for his contribution at the early stage of the experiment. The starting up of the experiment was going well thanks to his experiences on the (K^-, K^+) reaction. I wish to thank Mr. Tomokatsu Hayakawa for his great contributions for the set up and analysis of the experiment.

I would express my gratitude to Prof. Shin'ya Sawada and Prof. Toshiyuki Takahashi for supports for the designing and managing the E559 experiment. Prof. Sawada always relaxed and encouraged me and other graduate students. Prof. Takahashi is one of the specialist of the experiment at SKS and I learned many things from his experience on the experiment from both aspects of the hard ware and soft ware. I wish to thank to Mr. Masahi Hayata, Mr. Seishi Dairaku and Mr. Daisuke Nakajima for their great efforts to the design and operation of the range counter, large acceptance chamber and liquid hydrogen target, respectively. I would express my gratitude to Prof. Tomofumi Nagae, who is the leader of the SKS group, for his helps and suggestions based on his experiences of the experiment at SKS. I am grateful to Dr. Shigeru Ishimoto and Dr. Shoji Suzuki. They made great efforts to construct the liquid hydrogen target system and operate it quite stably. I would wish to thank to Dr. Tomofumi Maruta and Mr. Hiroyuki Fujioka for their sizable contributions during not only the experimental shift time but also the preparation and analysis periods. I would wish to thank to Dr. Michiko Sekimoto for experimental supports at the test experiment and the E559 experiment. I would like to thank to Dr. Shuhei Ajimura, who is the specialist of the trigger system of SKS, for help to make the (K^+, π^+) trigger.

I cordially thank the beam channel group for their support to provide beam with the excellent condition during both experiments. Especially I thank Prof. Masaharu Ieiri for his effort for the maintenance of the electrostatic separator. I am also thankful to Prof. Hiroyuki Noumi, Dr. Yoshinori Sato and Dr. Akihisa Toyoda for their great efforts to provide K^+ beams with good condition. They re-tuned the beam condition whenever I asked them.

I would like to express my gratitude to Prof. Hirokazu Tamura, who is the leader of Hyperball group. He gave me a chance to join E509 experiment and write the results as my master thesis. After the E509 experiments, he gave me many opportunities to join his experiments and he and his students also helped my experiments. I am sincerely grateful to Dr. Kiyoshi Tanida, who was also supervisor when I was a master student. I am very impressed by his vivid sense for physics and his kindness for collaborators. I would like to thank to Dr. Mifuyu Ukai for her encouragements. I would like to thank to Dr. Yusuke Miura for his great support at many experiments I joined.

I would like to express my gratitude to Prof. Takashi Nakano and Prof. Kenneth H. Hicks, who triggered experimental search for Θ^+ at many collaborations. Discussion with them gave me many motivations for my analysis and was quite useful for me. I would like to express my thanks to Prof. Atsushi Hosaka and Dr. Tetsuo Hyodo for their theoretical calculation.

I would address my thanks to all the members of KEK-PS E522 and E559 collaboration, Dr. Hiroki Sato. Mr. Yoshinori Fukao, Ms Hiromi Okada, Mr. Kazuya Aoki, Mr. Kaoru Taketani, Mr. Kohei Shoji, Mr. Tetsuya Hibi, Mr Haruyuki Nishikawa, Mr. S.J. Kim, Mr. B.H. Choi, Mr. Tomohiro Kameyama, Dr. Takaomi Watanabe, Dr. Megumi Naruki, Dr. Hisako Fujimura, Mr. Yoshichika Seki, Mr. Satoru Kamigaito, Mr. Katsuyuki Senzaka, Mr. R. Zavislak, Prof. Tomokazu Fukuda, Ms. Sari Kinoshita, Dr. Takeshi Koike, Mr. Yue Ma, Mr. Koutaro Shirotori, Prof. Jacques Arvieux and Mr. Tomonori Takahashi.

During my master course, I joined experiments at SPring-8/LEPS. I would address my thanks to all members of LEPS collaboration. Especially I would like to thanks Dr. Takatsugu Ishikawa, Mr. Manabu Miyabe and Mr. Masayuki Niiyama. They taught me quite many things about experimental technique through the experiment at LEPS and construction of TPC, analysis procedure from very elementary points, when I was in first grade of my master course.

I would like to thank members of NH group in the same grade, Mr. Yoshinori Fukao, Mr. Terunao Nakura, Ms. Hiromi Okada, Mr. Shinsuke Ota, Mr. Satoru Terashima, Mr. Manabu Togawa for their friendships and encouragements. Talk and discussion with them make my graduate school days fruitful and enjoyable.

Finally, I would address my heartfelt thanks to my parents, Mr. Norio Miwa and Ms. Chizuko Miwa and my brother, Dr. Yohei Miwa. They have supported me not only financially but also mentally with their warm encouragement. I could not finish this thesis work without their continuous support, patience and encouragement.

Appendix A

Scintillating Fiber Target System

A.1 Scintillating Fiber Block

The SCIFI block consisted of 300 μm $\times$ 300 μm square plastic scintillating fibers (KURARAY SCSF-78). The core of the fiber was 288 μm $\times$ 300 μm and its material was polystyrene ($(CH)_n$). The refractive index of the core was 1.59 and the density was 1.03 g/cm^3. The cladding was made of polymethylmethacrelate (PMMA, $C_5H_8O_2$) with refractive index of 1.49 and density of 1.19 g/cm^3. The wave length of transmitted light was peaked at 450 nm. All fibers were coated with white paint as an extra mural absorber (EMA). The attenuation length of SCSF-78 (300 μm square) was 114 cm. The attenuation length was defined as the longer decay constant obtained with the two components exponential fitting. The length of the fibers which used for the SCIFI target was about 30 cm, and the effective volume of the target corresponded to from 0 cm to 10 cm.

A.2 Image-intensifier tubes and CCD camera

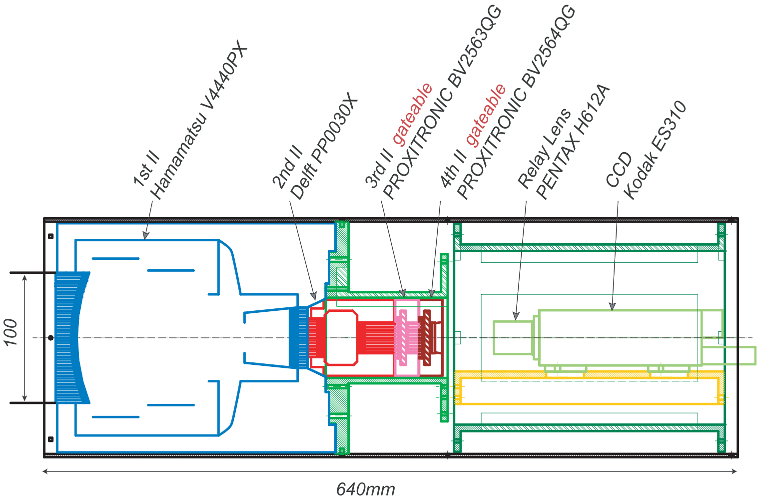

Figure A.1: Schematic drawing of the structure of IIT chain for SCIFI target system.

The first and second stages were electrostatic-type image intensifier tubes. The first stage (HAMAMATTSU V4440PX) had a large input window (100 m ϕ) which was made of glass fibers. The quantum efficiency of photo-cathode was 19 %. The applied anode voltage of the first IIT was 20 kV. The phosphor of the first IIT was PS-5 whose decay time was measured to be 1.3 μs. The diameter of the fiber-optic output window was 25 mm ϕ, i.e. the image was demagnified by a factor of four with the electrostatic lens system.

The second IIT (DEP PP0030X) was used in order to obtain sufficient number of photons before a micro-channel plate (MCP) in the next stage. The diameters of both input and output fiber-optic windows were 25 mm ϕ. The phosphor of 300 ns decay time (P46) was used for second IIT.

The third and fourth stages were MCP type image intensifiers (PROXITRONIC BV2563 QG). The diameters of the input and output windows were 25 mm ϕ. These IITs were gatable. The first-level trigger opened these gates for 2 μs to cover the decay time of the first phosphor of 1.3 μs. The decay time of the phosphor (P20) for the these IITs were 20 μs, whereas the decision time of the second-level trigger was about 14 μs.

The image amplified by four IITs was digitalized by CCD camera (Kodac MEGAPLUS Camera ES310). The CCD camera consisted of 648 × 484 pixels where the size of each pixel was 9 μm × 9 μm. The readout of the charge on the CCD was started by the external trigger. The digital data were compressed from 8 bit to 4 bit using the real time image processing module (Imaging Techmology Coop. MVC 150/40).

A.3 Correction of distorted image

Images are distorted mainly due to the pin-hole distortion caused by the electro-static lenses of IITs. The distortion can be expressed as,

$$\begin{pmatrix} X' \\ Y' \end{pmatrix} = (a_0 + a_1 r + a_2 r^3 + a_3 r^5 + \cdots) \begin{pmatrix} X \\ Y \end{pmatrix},$$

where (X, Y) and (X', Y') represent original coordinates and distorted ones, respectively, and r is$\sqrt{X^2 + Y^2}$. The coefficients a_i are correction parameters. Since SCIFI target were installed very close to the spectrometer, their images were also distorted by the magnetic field (about 0.01 or 0.02 T), although we minimized the distortion by covering each IIT chain with a double magnetic shield made of iron and μ-metal. Therefore, the pin-hole distortions as well as the effect due to the remaining magnetic field were corrected with following expression,

$$\left\{ \begin{array}{l} X' = b_0 + b_1 X + b_2 Y + b_3 X^2 + b_4 XY + b_5 Y^2 + b_6 X^3 + b_7 X^2 Y + b_8 XY^2 + b_9 Y^3 \\ Y' = c_0 + c_1 X + c_2 Y + c_3 X^2 + c_4 XY + c_5 Y^2 + c_6 X^3 + c_7 X^2 Y + c_8 XY^2 + c_9 Y^3 \end{array} \right.$$

The correction parameters, b_i and c_i, were determined using the images of a plate with a grid-pattern LED. Figure A.2 (a) shows the grid image viewed by left-sided IIT and Figure A.2 (b) shows that after the correction using above equation. After this correction image reconstruction was performed.

(a) Before correction

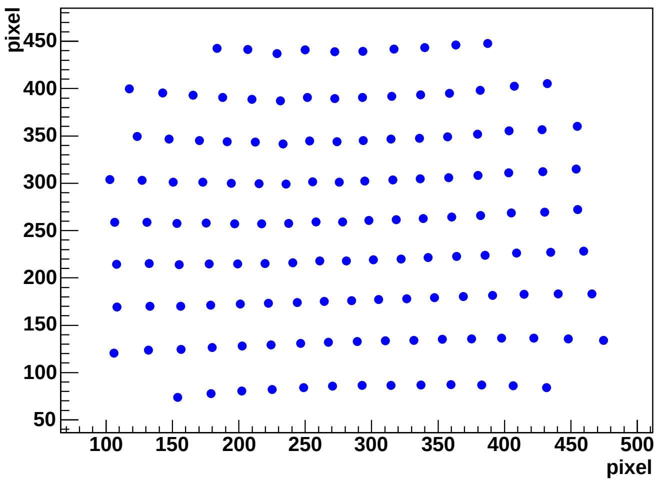

(b) After correction

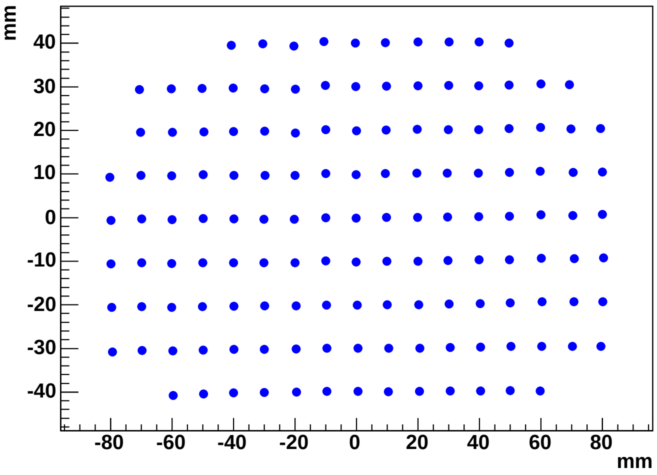

Figure A.2: The grid image viewed by the left-sided IIT (a) before and (b) after the correction.

Appendix B

KEK-PS E559 experiment

– Search for the Θ^+ baryon via $K^+p \to \pi^+X$ reaction –

After the E522 experiment, we proposed an experiment to search for the Θ^+ via $K^+p \to \pi^+X$ reaction to give a conclusive information on the existence of the Θ^+. Although theoretical prediction expected large production cross section in this reaction (more than several ten μb), the experiment was designed to have sensitivity until small production cross section (about 10 μb) because the cross section is also expected to be small considering the small cross section via $\pi^-p \to K^-\Theta^+$ reaction.

We have performed the E559 experiment to search for the Θ^+ via the K^+ induced reaction at the K6 beam line with high statistics and good missing mass resolution using SKS spectrometer at KEK 12 GeV Proton Synchrotron (KEK-PS E559). The experimental periods were about one month from June 2005 and two weeks from December 2005. We used K^+ beams of 1.2 GeV/c and total 6.1×10^9 kaons were irradiated. By using K^+ beams including $\bar{s}$ quark, the strangeness of the reconstructed system by the missing mass of the $K^+p \to \pi^+X$ reaction was a priori known to be positive. Naively the production cross section via $K^+p \to \pi^+\Theta^+$ reaction is expected to be larger than that via $\pi^-p \to K^-\Theta^+$ reaction, because K^+ beams already include $\bar{s}$ quark. Therefore the high statistics search is expected to be possible. One of the most important purpose is the determination of the width of the Θ^+ by utilizing spectrometer system, SKS and K6 beam line, with the excellent missing mass resolution of 2.4 MeV/c^2 (FWHM). Therefore this experiment will give the information to understand the narrow width and give the insight about non-perturbative QCD, if we observe the Θ^+. Figure B.1 shows the experimental setup of the E559 experiment. As a target, a new liquid hydrogen target system was constructed for both this experiment and future experiments at J-PARC [75]. The thickness of the liquid hydrogen target was 12.5 cm. The momentum of each beam particle was analyzed using the K6 beam line spectrometer of which resolution is expected to be $\Delta p/p$=0.047% (FWHM). Scattered particles were detected using SKS spectrometer.

The background of the measurement is divided into two parts. One is the physical background such as Δ and K^* production. Another background is the 3 body decay of K^+ such as $K^+ \to \pi^+\pi^+\pi^-$ or $K^+ \to \pi^+\pi^0\pi^0$. The latter background was quite severe and the rejection of these decay backgrounds was essential for the Θ^+ search. In decay events, one or three charged particles were emitted to a forward angle, whereas in a hadronic reaction such as Δ production or Θ^+ production, two charged particles were emitted with a large scattering angle. Therefore we installed a large acceptance chamber just downstream of the target to detect the charged particles [76]. We selected two charged particle events to reject decay events in offline analysis. To improve S/N ratio by detecting K^+ from the decay of Θ^+, we also installed a range counter system at the downstream of this chamber [77].

Let us now describe the present analysis status of the (K^+, π^+) data. The momentum analyses of incident and outgoing particles are done well, since the Σ^+ is clearly reconstructed with almost expected resolution using the $\pi^+ p \to K^+ X$ reaction taken for the calibration as shown in Figure B.2. The vertex distribution after the rejection of decay events is shown in Figure B.3 together with the distribution of the empty target data (blue-hatched histogram). The 12.5 cm liquid hydrogen image is clearly observed. We took approximately 15,000 and 10,000 events of $K^+ p \to \pi^+ X$ reaction in the first and second run, respectively. However, there are still background events which is shown in the hatched histogram. These events might be the contaminations of the K^+ decay events and reaction events at the timing counter upstream of the target (BH2). We will compare the vertex distribution attributed to these background events with a simulation in future studies.

The analysis of the $K^+ p \to \pi^+ X$ reaction is still preliminary and the analysis of the missing mass is in progress.

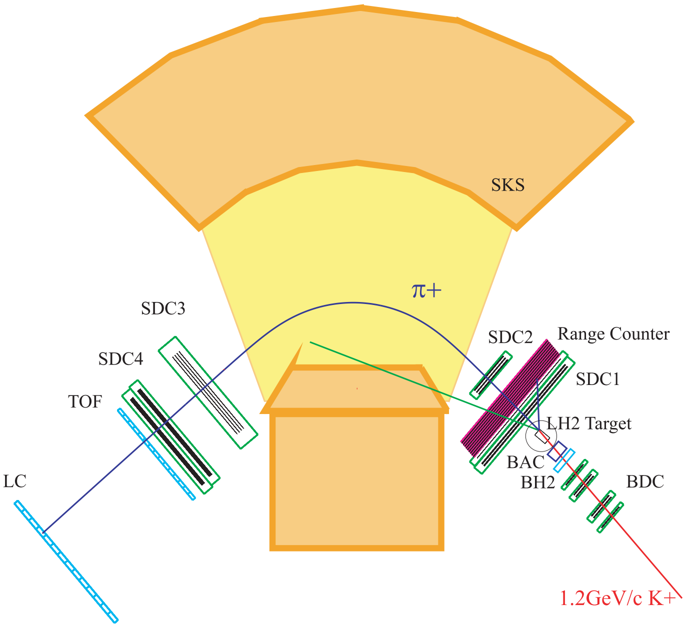

Figure B.1: Experimental setup of the KEK-PS E559. As a target, a liquid hydrogen target was used. The shape of the container was a cylinder, of which length was 12.5 cm and diameter was 6.8 cm. Beam line spectrometer consisted of 4 drift chambers (BDC1,2,3,4) and trigger counters (BH1,2 and BAC) located upstream and downstream of QQDQQ magnet system. The SKS spectrometer consisted of 4 drift chambers (SDC1,2,3,4) and trigger counters (TOF, LC). The magnetic field of the SKS was set to 1.6 T which was corresponding to the central momentum of 0.55 GeV/c. In order to suppress the background due to the decay of K^+ beams and improve S/N ratio by detecting K^+, a large acceptance chamber and a range counter system were installed after the target to detect the charged particles.

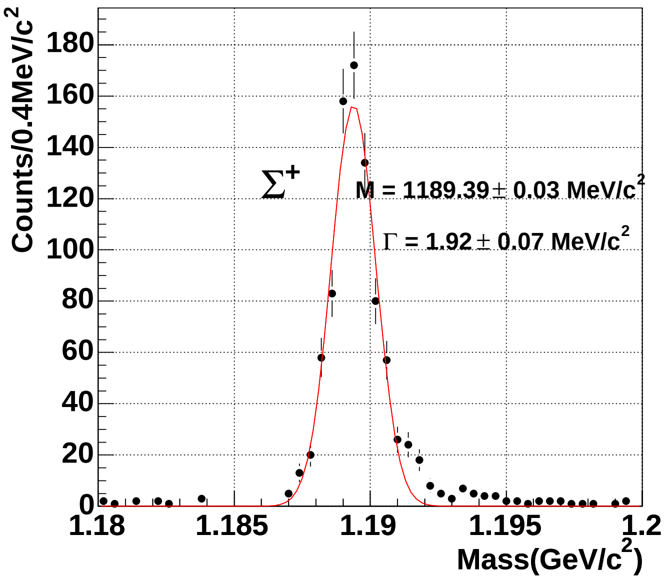

Figure B.2: Missing mass spectrum of the $\pi^+ p \rightarrow K^+ X$ reaction. The peak corresponding to Σ^+ was clearly observed with the expected experimental resolution of 1.92±0.07 MeV/c^2.

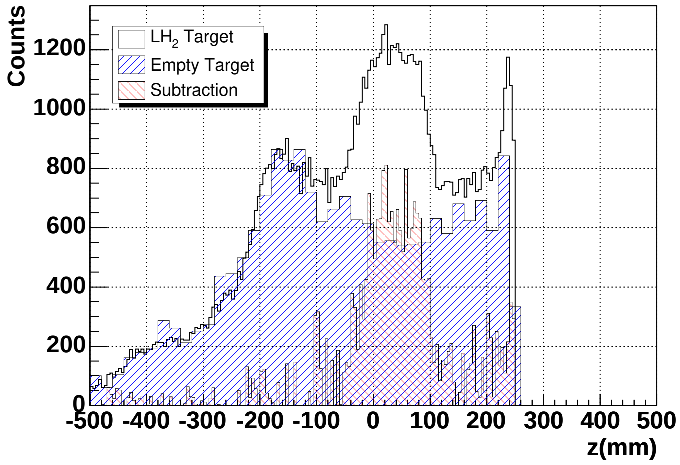

Figure B.3: Vertex distribution of $K^+ p \rightarrow \pi^+ X$ reaction obtained from first run. The blue hatched histogram represents the background event estimated from the empty target data. The red hatched histogram shows the net contribution of $K^+ p$ interaction events.

Bibliography

[1] R.L. Jaffe, Proc. Topical Conference on Baryon Resonances, Oxford, July 1976, SLAC-PUB-1774.

[2] K.Hashimoto, Phys. Rev. C **29**, 1377 (1984).

[3] R.A. Arndt and L.D. Poper, Phys. Rev. D **31**, 2230 (1985).

[4] Particle Data Group, Phys. Lett. B **170**, 289 (1986).

[5] Particle Data Group, Rev. Mod. Phys. **48**, SI88 (1976).

[6] R.L. Kelly, in Proceedings of the Meeting on Exotic Resonances (Hiroshima, 1978), ed. I. Endo *et al.*

[7] G.C. Oades, in Low and Intermediate Energy Kaon-Nucleon Physics (1981), ed. E. Ferrari and G. Violini.

[8] T. Nakano *et al.*, Phys. Rev. Lett. **91**, 012002 (2003).

[9] D. Diakonov, V. Petrov, M. Polyakov, Z. Phys. A **359**, 305 (1997).

[10] K. H. Hicks; Prog. Part. Nucl. Phys. **55**, 647 (2005).

[11] K. Goeke, H.-C. Kim, M. Praszalowicz and G.-S. Yang, Prog. Nucl. Part. Phys. **55**, 350 (2005).

[12] R. Jaffe, F. Wilczek, Phys. Rev. Lett. **91**, 232003 (2003).

[13] M. Karliner and H.J. Lipkin, Phys. Lett. B **575**, 249 (2003).

[14] T. Kishimoto and T. Sato, hep-ex/0312003.

[15] S. Sasaki, Phys. Rev. Lett. **93**, 152001 (2004).

[16] F. Csikor, Z. Fodor, S.D Katz, T.G. Kovacs, JHEP 0311 (2003) 070.

[17] N. Mathur *et al.*, Phys. Rev D **70**, 074508 (2004).

[18] T.W. Chiu and T.H. Hsieh, Phys. Rev D **72**, 034505 (2005).

[19] N. Ishii *et al.*, Phys. Rev D **71**, 034001 (2005).

[20] J. Sugiyama, T. Doi and M. Oka, Phys. Lett. B **581**, 167 (2004).

[21] T. Bowen *et al.*, Phys. Rev D **2**, 2599 (1970).

[22] T. Bowen *et al.*, Phys. Rev D **7**, 22 (1973).

[23] R.G. Glasser *et al.*, Phys. Rev D **15**, 1200 (1977).

[24] S. Nussinov, hep-ph/0307357.

[25] J.S. Hyslop *et al.*, Phys. Rev D **46**, 961 (1992).

[26] R.A. Arndt, I.I. Strakovsky and R.L. Workman, Phys. Rev C **68**, 042201(R) (2003).

[27] R.N. Cahn and G.H. Trilling, Phys. Rev D **69**, 011501(R) (2004).

[28] W.R. Gibbs, Phys. Rev C **70**, 045208 (2004).

[29] DIANA Collaboration, V. V. Barmin *et al.*, Phys. Atom. Nucl. **66**, 1715 (2003).

[30] CLAS Collabaration, S. Stepanyan *et al.*, Phys. Rev. Lett **91**, 252001 (2003).

[31] SAPHIR Collabaration, J. Barth *et al.*, Phys. Lett. B **572**, 127 (2003).

[32] A. E. Asratayn, A. G. Dolgolenko and M. A. Kubantsev, Phys. Atom. Nucl. **67**, 682 (2004).

[33] CLAS Collabaration, V. Kubarovsky *et al.*, Phys. Rev. Lett **92**, 032001 (2004).

[34] HERMES Collabaration, A. Airapetian *et al.*, Phys. Lett. B **585**, 213 (2004).

[35] ZEUS Collabaration, S. Chekanov *et al.*, Phys. Lett. B **591**, 7 (2004).

[36] COSY-TOF Collabaration, M. Abdel-Bary *et al.*, Phys. Lett. B **595**, 127 (2004).

[37] SVD Collabaration, A. Aleev *et al.*, arXiv:hep-ex/0401024.

[38] P.Zh. Aslanyan *et al.*, arXiv:hep-ex/0403044.

[39] NA49 Colaboration, C. Alt *et al.*, Phys. Lev. Lett **92**, 042003 (2004)

[40] H1 Colaboration, A. Aktas *et al.*, Phys. Lett. B **588**, 17 (2004)

[41] BES Collabaration, J. Z. Bai *et al.*, Phys. Rev. D **70**, 012004 (2004).

[42] BABAR Collabaration, SLAC-PUB-10598, hep-ex/0408064.

[43] BABAR Collabaration, B. Aubert *et al.*, hep-ex/0502004.

[44] Belle Collabaration, K. Abe *et al.*, hep-ex/0409010.

[45] ALEPH Collabaration, S. Schael *et al.*, Phys. Lett. B **599**, 1 (2004).

[46] HERA-B Collabaration, I. Abt *et al.*, Phys. Rev. Lett **92**, 212003 (2004).

[47] SPHINX Collabaration, Yu. M. Antipov *et al.*, Eur. Phys. J. **A21**, 455 (2004).

[48] Hyper-CP Collabaration, M.J. Longo *et al.*, Phys. Rev. D**70**, 111101(R) (2004).

[49] CDF Collabaration, D. O. Litvintsev *et al.*, Nucl. Phys. B (Proc. Suppl.) **142**, 374 (2005).

[50] FOCUS Collabaration, K. Stenson *et al.*, Int. J. Mod. Phys. A **20** 3745 (2005).

[51] Belle Collabaration, Phys. Lett. B **632**, 173 (2006).

[52] PHENIX Collabaration, C. Pinkerton *et al.*, J. Phys. G **30**:S1201 (2004).

[53] CLAS Collabaration, M. Battaglieri et al., Phys. Rev. Lett **96** 042001 (2006).

[54] CLAS Collabaration, B. McKinnon et al., hep-ex/0603028.

[55] A.I. Titov, A. Hosaka, S. Date, Y. Ohahi, Phys. Rev. C **70** 042202 (2004).

[56] O. I. Dahl et al., Phys. Rev. **163** 1377 (1967).

[57] W. Liu and C. M. Ko , Phys. Rev. C **68** 045203 (2003).

[58] Y. Oh, H. Kim, and S. H. Lee , Phys. Rev. D **69** 014009 (2004).

[59] Y. Oh, H. Kim, and S. H. Lee , Phys. Rev. D **69** 074016 (2004).

[60] T. Hyodo, A. Hosaka, and E. Oset, Phys. Lett. B **579** 290 (2004).

[61] C.H. Li and C.M. Ko, Nucl. Phys A **712** 110 (2002).

[62] R.L. Workman and H.W. Fearing, Phys. Rev D **37** 3117 (1988).

[63] W. Liu, C.M. Ko and S.H. Lee, Nucl. Phys A **728** 457 (2003).

[64] J.K. Ahn et al., Phys. Lett. B **444** (1998) 267.

[65] C.J. Yoon et al., Proc. of the YITP workshop “Multi-quark Hadrons; for, five and more ?”, http://www.slac.stanford.edu/econf/C0402171/files/manuscripts/Yoon.pdf .

[66] J.K. Ahn et al., Nucl. Instr. and Meth. A **457** 137 (2001).

[67] A. Yamamoto, KEK report 81-13, (1981).

[68] K. Amako et al., Nucl. Instr. and Meth. **197** 325 (1982).

[69] S. Agostinelli et al., Nucl. Instrum. Methods. A 506 (2003) 250.

[70] K.L. Brown et al., CERN 76-13, (1976), SLAC-91, (1974).

[71] J. Myrheim and L. Bugge, Nucl. Instrum. Methods. **160** 43 (1979).

[72] S. Agostinelli et al., Nucl. Instrum. Methods. A **506** 250 (2003).

[73] Y. Kondo, Ph.D. thesis, Kyoto University (2000), (unpublished).

[74] T. Hyodo, and A. Hosaka, Phys. Rev. C **72** 055202 (2005).

[75] D. Nakajima, Master’s thesis, University of Tokyo (2005) (unpublished).

[76] S. Dairaku, Master’s thesis, Kyoto University (2005) (unpublished).

[77] M. Hayata, Master’s thesis, Kyoto University (2004) (unpublished).